NASA/CR—1998-208511

A Numerical Simulator for Three-Dimensional Flows Through Vibrating Blade Rows

H. Andrew Chuang and Joseph M. Verdon
United Technologies Research Center, East Hartford, Connecticut

Prepared under Contract NAS3–26618

National Aeronautics and
Space Administration

Lewis Research Center

August 1998

Available from

NASA Center for Aerospace Information
7121 Standard Drive
Hanover, MD 21076
Price Code: A05

National Technical Information Service
5287 Port Royal Road
Springfield, VA 22100
Price Code: A05

A Numerical Simulator for Three-Dimensional Flows through Vibrating Blade Rows

Contents

Summary **1**

1 Introduction **3**

2 Unsteady Flow through a Vibrating Blade Row **5**

3 Fluid Dynamic Equations **7**
3.1 Governing Equations 7
3.2 High Reynolds Number Approximations 9
3.3 Solution Strategy 10

4 Near-Field, Finite-Volume Analysis **12**
4.1 Finite-Volume Equations 12
4.2 Evaluation of Flux Terms 13
4.3 Solution Procedure 16

5 Far-Field Eigenanalyses **18**
5.1 Unsteady Perturbations in the Far Field 18
5.2 Classification of Unsteady Disturbances 21
5.3 Near-Field/Far-Field Matching Procedure 22

6 Numerical Results **24**
6.1 3D 10th Standard Configuration 25
6.2 NASA Rotor 67 32
6.3 Discussion 36

7 Concluding Remarks **38**

References **40**

Figures 1 through 28 **44**

List of Figures

Figure 1. Rotating axial compressor blade row operating within an annular duct.

Figure 2. 3D Tenth Standard Configuration undergoing an exaggerated torsional motion ($\alpha_{hub} = 0$ deg, $\alpha_{tip} = 45$ deg). The rotor consists of 24 airfoils. The nodal diameter of the blade motion is 6, which results in an interblade phase angle of 90 deg. The outer casing has been eliminated from the figure for clarity.

Figure 3. TURBO computational grid at midspan for the 3D 10th Standard Cascade.

Figure 4. Relative steady isentropic surface mach number distributions for the 3D 10th Standard Cascade ($M_{-\infty}^{\text{abs}} = 0.4015$, $|\Omega| = 0.2145$).

Figure 5. Relative frame steady flow properties far upstream and far downstream of the 3D 10th Standard Cascade ($M_{-\infty}^{\text{abs}} = 0.4015, |\Omega| = 0.2145$).

Figure 6. Local work per cycle distributions at all spanwise stations and global works per cycle for the 3D 10th Standard Cascade undergoing pure torsional vibrations about midchord and pure bending vibrations at $\omega = 1$ and $\sigma = \mp 90$ deg ($N_D = \mp 6$).

Figure 7. Averaged local work per cycle distributions at midspan, as predicted using the 3D TURBO and the 2D LINFLO analyses, for the 3D 10th Standard Cascade undergoing torsional blade vibrations about midchord at $\omega = 1$.

Figure 8. Averaged local work per cycle distributions at midspan, as predicted using the 3D TURBO analysis with one-dimensional, local, far-field conditions and the 2D LINFLO analysis, for the 3D 10th Standard Cascade undergoing bending vibrations at $\omega = 1$.

Figure 9. Averaged local work per cycle distributions, at midspan, as predicted using the 3D TURBO and the 2D LINFLO analyses, for the 3D 10th Standard Cascade undergoing bending vibrations at $\omega = 1$.

Figure 10. Work per cycle versus interblade phase angle for the 3D 10th Standard Cascade undergoing pure torsional vibrations about midchord (top) and pure bending vibrations (bottom) at $\omega = 1$.

Figure 11. Axial eigenvalues, $\chi = \beta + i\kappa_\xi$, at inlet for three circumferential ($m = -1, 0, 1$) and three radial ($\mu = 0, 1, 2$) modes of steady ($n = 0$), first-harmonic ($n = 1$) and second-harmonic ($n = 2$) acoustic disturbance in an unsteady flow at $\omega = 1.0$ and $N_D = 6$, through the 3D 10th Standard Cascade.

Figure 12. Axial eigenvalues, $\chi = \beta + i\kappa_\xi$, at exit for three circumferential ($m = -1, 0, 1$) and three radial ($\mu = 0, 1, 2$) modes of steady ($n = 0$), first-harmonic ($n = 1$) and second-harmonic ($n = 2$) acoustic disturbance in an unsteady flow at $\omega = 1.0$ and $N_D = 6$, through the 3D 10th Standard Cascade.

Figure 13. First harmonic, radial, pressure modes, $p^R_{m\mu}(r)$, $m = -1, 0, 1$, $\mu = 0, 1, 2$, at inlet and exit due to an acoustic excitation or response, at $N_D = 6$, far upstream and for an acoustic response, at $N_D = 6$, far downstream of the 3D 10th Standard Cascade: (——) in-phase component; (- - -) out-of-phase component of $p^R_{m\mu}(r)$.

Figure 14. Time histories of mass flow and total pressure ratio for the 3D 10th Standard Cascade undergoing a pure bending vibration at $\omega = 1.0$ and $N_D = -6$.

Figure 15. First-harmonic unsteady pressure distributions at midspan acting on four blades of the 3D 10th Standard Cascade undergoing a pure bending vibration at $\omega = 1.0$ and $N_D = -6$.

Figure 16. Local work per cycle distributions on four blades of the 3D 10th Standard Cascade undergoing a pure bending vibration at $\omega = 1.0$ and $N_D = -6$.

Figure 17. Local work per cycle distributions at midspan for the 3D 10th Standard Cascade undergoing a pure bending vibration at $\omega = 1.0$ and $N_D = -6$.

Figure 18. TURBO computational grid for the NASA Rotor 67 and leading edge detail at blade tip.

Figure 19. Comparison of measured and computed fan total pressure characteristics for the NASA Rotor 67 fan.

Figure 20. Experimental and numerical relative Mach number contours near peak efficiency.

Figure 21. Experimental and numerical relative Mach number contours near stall.

Figure 22. Steady static pressure distributions for the Rotor 67 fan (a) near the peak efficiency point, and (b) near stall.

Figure 23. Relative frame steady flow properties (a) far upstream and (b) far downstream of the NASA Rotor 67 fan ($M^{\text{abs}}_{-\infty} \approx 0.526$, $|\Omega| = 2.524$).

Figure 24. Axial eigenvalues, $\chi = \beta + i\kappa_\xi$, at inlet for the time-mean ($n = 0$), and the first ($n = 1$) and second ($n = 2$) temporal harmonics, and three circumferential ($m = -1, 0, 1$) and five radial ($\mu = 0, 1, 2, 3, 4$) modes of acoustic disturbance in the far field of Rotor 67, for an unsteady flow at $\omega = 0.54$ and $N_D = 0$, and a meanflow condition near peak efficiency.

Figure 25. Axial eigenvalues, $\chi = \beta + i\kappa_\xi$, at exit for the time-mean ($n = 0$), and the first ($n = 1$) and second ($n = 2$) temporal harmonics, and three circumferential ($m = -1, 0, 1$) and five radial ($\mu = 0, 1, 2, 3, 4$) modes of acoustic disturbance in the far field of Rotor 67, for an unsteady flow at $\omega = 0.54$ and $N_D = 0$, and a meanflow condition near peak efficiency.

Figure 26. First harmonic, radial pressure modes, $p^R_{m\mu}(r)$, $m = -1, 0, 1$, $\mu = 0, 1, 2$, for an acoustic excitation or response, at $N_D = 0$, far upstream and for an acoustic response, at $N_D = 0$, far downstream of the Rotor 67 fan: (——) in-phase component; (- - -) out-of-phase component of $p^R_{m\mu}(r)$.

Figure 27. Local work per cycle distributions and global works per cycle for the Rotor 67 fan undergoing pure torsional vibrations about midchord at $\omega = 0.54$ and $\sigma = 0$ and 180 deg ($N_D = 0$ and 11).

Figure 28. Local work per cycle distributions and global works per cycle for the Rotor 67 fan undergoing pure bending vibrations at $\omega = 0.54$ and $\sigma = 0$ and 180 deg ($N_D = 0$ and 11).

A Numerical Simulator for Three-Dimensional Unsteady Flows through Vibrating Blade Rows

Summary

The three-dimensional, multi-stage, unsteady, turbomachinery analysis, TURBO, has been extended to predict the aeroelastic and aeroacoustic response behaviors of a single blade row operating within a cylindrical annular duct. In particular, a blade vibration capability has been incorporated so that the TURBO analysis can be applied over a solution domain that deforms with a vibratory blade motion. Also, unsteady far-field conditions have been implemented to render the computational boundaries at inlet and exit transparent to outgoing unsteady disturbances. The modified TURBO analysis is applied herein to predict unsteady subsonic and transonic flows. The intent is to partially validate this nonlinear analysis for blade flutter applications via numerical results for benchmark unsteady flows, and to demonstrate the analysis for a realistic fan rotor. For these purposes, we have considered unsteady subsonic flows through a 3D version of the 10th Standard Cascade, and unsteady transonic flows through the first stage rotor of the NASA Lewis, Rotor 67, two-stage fan.

1. Introduction

The development of analyses to predict unsteady flows through turbomachinery blade rows has been motivated primarily by the need to predict the aeroelastic (flutter and forced vibration) and aeroacoustic (sound generation and propagation) characteristics of the blading. Accurate and efficient aerodynamic analyses are needed to determine the unsteady loads that act on the blades and the unsteady pressure responses that persist upstream and downstream of the blade row, for various sources of unsteady excitation. The latter include structural (blade) motions and aerodynamic disturbances at inlet and exit that carry energy towards the blade row.

The computational resources required to simulate nonlinear unsteady flows continue to prohibit the use of such simulations in detailed aeroelastic or aeroacoustic design studies. Thus, for the most part, the unsteady aerodynamic analyses that are being used in turbomachinery aeroelastic and aeroacoustic design prediction systems are based on linearized inviscid flow theory [Ver93], which has evolved to the point that three-dimensional, linearized, Euler analyses are being developed [HL93, HCL94, Sre96, MV97]. Linear analyses meet the needs of turbomachinery designs for efficient unsteady aerodynamic response predictions. However, of necessity, such analyses ignore potentially important physical features of unsteady flows, including the effects of moderate to large amplitude unsteady excitation and the effects of viscous-layer displacement and separation.

Time-accurate, nonlinear, Euler and Reynolds-averaged Navier-Stokes analyses, are therefore needed to understand and predict the relative importance of nonlinear and viscous effects on the unsteady flows associated with blade vibration and blade-row noise generation. Since the mid 1980's, a number of such analyses have been developed for turbomachinery configurations. These have been applied to predict flows through single blade rows in which the unsteadiness is caused by prescribed blade vibrations [HR89, Sid91, HD93, GV94, PGW96, GC96, AV96, BSK97] or by prescribed aerodynamic disturbances at the inflow or outflow boundaries [Gil88, DV94, CCA94], and flows through aerodynamically coupled arrays in which the unsteadiness is caused by the relative motions of adjacent blade rows [Rai87, Rai89, JW89, JW90, JHW92, CW93].

These recent and important advances in the numerical simulation of unsteady flows demonstrate the power and potential usefulness of nonlinear unsteady aerodynamic codes. Most of the related activity to date has been focused on developing numerical strategies for solving the Euler and Navier-Stokes equations and on implementing these strategies into useful codes. Although there is still a need for improvements in algorithm speed and accuracy and, more importantly, in the treatment of flow boundary conditions, a major focus of continuing work must be placed on validating the capabilities of modern Euler/Navier–Stokes solution schemes for accurately predicting turbomachinery flow phenomena. Once validated, Euler and Navier-Stokes analyses for turbomachinery unsteady flows can provide engineers with useful insights into the impact of nonlinear and viscous effects on blade vibration and discrete-tone noise generation. These analyses would also provide a test-bed for evaluating and improving the linearized models that are being developed for use in aeroelastic and aeroacoustic design prediction systems.

Under the present effort, we have modified and applied the nonlinear unsteady analysis, TURBO, to predict unsteady flows through single vibrating blade rows. TURBO is a multi-stage turbomachinery code that has been constructed, as part of a long range research effort [Jan89, JW89, JW90, JHW92, CW93, CCA94] conducted at Mississippi State University (MSU), to simulate the complex unsteady flow phenomena occurring in turbomachines. The Euler, the thin-layer Reynolds-averaged Navier-Stokes equations or the full Reynolds-averaged Navier-Stokes equations are solved using an implicit, cell-centered finite volume scheme, in which inviscid or convective flux Jacobians are evaluated using flux vector splitting and inviscid residual fluxes are evaluated using Roe's [Roe81] flux difference splitting to form a higher-order TVD scheme. Viscous or diffusive fluxes can be treated either explicitly [CW93] or implicitly [CCA94]. Newton subiterations are used as part of the time-stepping procedure to converge the unsteady solution at each time step. At each subiteration level, the discrete equations are approximately factored and solved using a modified two-pass matrix solver [Whi90], based on the Gauss-Seidel iteration procedure.

In the present study, we have extended and applied TURBO to predict unsteady flows through single vibrating blade rows operating within cylindrical annular ducts. In particular, we have implemented a blade vibration capability into TURBO so that unsteady solutions can be determined over a domain that deforms with a vibratory blade rotation. In addition, we have incorporated far-field conditions into TURBO to render computational inlet and exit boundaries transparent to outgoing disturbances and to allow incoming aerodynamic disturbances to be prescribed as approximate solutions to the governing equations.

The goals of the present effort have been to extend, demonstrate and validate the TURBO analysis for blade flutter applications. In the present version of TURBO, the implicit, wave-split, finite-volume analysis, developed at MSU, is applied to predict the unsteady flow in the near field, and coupled at the computational inflow and outflow boundaries, to far-field eigenanalyses for the unsteady perturbations of fully-developed, axisymmetric, mean flows. The resulting analysis is described in this report and applied to predict unsteady flows through a three-dimensional version of the 10th Standard Cascade [FV93] and the NASA Rotor 67 fan. We have considered inviscid unsteady subsonic and transonic flows excited by prescribed blade vibrations and, for validation purposes, we have compared the TURBO results for 10th Standard Cascade with those based on the two-dimensional, potential-based linearization, LINFLO [Ver93], and those based on the three-dimensional, linearized Euler analysis, LINFLUX [MV97]. The predictions indicate that the current version of the 3D TURBO analysis can provide useful and accurate unsteady aerodynamic response information, provided that meshes of sufficient density and clustering are employed.

2. Unsteady Flow through a Vibrating Blade Row

We consider the flow, at high Reynolds number (Re) and with negligible body forces, of a perfect gas with constant specific heats through a rotating and vibrating blade row that operates within a stationary annular duct (see Figure 1). The duct is of infinite axial extent and has hub and duct radii, $r = r_H$ and $r = r_D$, respectively, and the blade row consists of N_B blades which rotate about the duct axis at constant angular velocity $\mathbf{\Omega} = \Omega \mathbf{e}_\xi$. We assume that the flows far upstream and far downstream from the blade row are at most small perturbations of fully-developed, axisymmetric, steady background flows, and that in the absence of a vibratory motion, the blades are identical in shape, equally spaced around the rotor, and identical in orientation relative to the axisymmetric inlet flow.

We will examine this unsteady flow in both stationary and rotating frames of reference, in terms of cylindrical ($\xi,\ r,\ \theta,\ t$) and Cartesian $(x_1, x_2, x_3, t) = (\xi,\ r\cos\theta,\ r\sin\theta, t)$ coordinates. Here ξ and r measure distance along and radially outward from the duct axis, respectively, and θ measures angular distance in the direction opposite to the direction of rotation, which is counterclockwise relative to an observer looking in the axial flow direction. When necessary, we will use the superscripts abs or rel to indicate that a physical quantity is measured relative to stationary or the rotating frame; e.g., $\theta^{\text{abs}} = \theta^{\text{rel}} + \Omega t$.

We intend to numerically resolve the unsteady flow, in terms of curvilinear spatial coordinates, on a computational grid that rotates with the blade row and deforms with the vibratory blade motion. The vector $\mathcal{R}(\bar{\mathbf{x}}, t)$ describes the displacement of a moving field (grid) point, $\mathbf{x}$, relative to its reference or mean position, $\bar{\mathbf{x}}$, in the rotating frame. The displacement field, $\mathcal{R}$, is prescribed so that the solution domain deforms with the vibratory motions of the blades and is rigid far from the blade row.

For aeroelastic and aeroacoustic applications, we are usually interested in a restricted class of unsteady flows; those in which the unsteady fluctuations can be regarded as disturbances to a background flow that is steady in a blade-fixed, rotating reference frame. Moreover, the steady background flows far upstream (say $\xi \le \xi_-$) and far downstream ($\xi \ \ge \ \xi_+$) from the blade row can be assumed to consist of at most a small steady perturbation from a fully-developed, axisymmetric, steady flow. The time-dependent or unsteady fluctuations in these flows arise from temporally and circumferentially periodic unsteady excitations, i.e., prescribed vibratory blade motions and prescribed aerodynamic disturbances at inlet and exit that carry energy towards the blade row.

For example, if the blades vibrate at reduced frequency, ω, as seen by an observer in the rotating frame, and at constant interblade phase angle, σ, we can write

$$\mathcal{R}_{\mathrm{B}_n}(\bar{r}, \bar{\theta} + 2\pi n/N_B, \bar{\xi}, t) = \mathbf{T}_n Re\{\mathbf{R}_{\mathrm{B}}(\bar{r}, \bar{\theta}, \bar{\xi}) \exp[i(\omega t + n\sigma)]\},\ \bar{\mathbf{x}} \text{ on } B\ . \qquad (2.1)$$

Here, $\mathcal{R}_{\mathrm{B}_n}$ is the displacement of a point on the nth moving blade surface from its mean position in the rotating frame; $\mathbf{T}_n$ is a rotation matrix, which rotates vectors through n passages; $n = 0, 1, 2, \ldots, N_B - 1$ is a blade index; $Re\{\ \}$ denotes the real part of $\{\ \}$; $\mathbf{R}_{\mathrm{B}}$ is the complex amplitude of the reference ($n = 0$) blade displacement; and B refers to the mean position of the reference blade. The interblade phase angle, σ, is determined by the nodal diameter pattern of the vibratory blade motion, i.e., $\sigma = 2\pi N_{\mathrm{D}}/N_B$, where $|N_{\mathrm{D}}|$, the number of nodal diameters, is the integer count of the number of times a disturbance pattern repeats around the wheel. The sign of N_{D} is determined by the direction of rotation of the disturbance pattern. If the vibratory disturbance pattern moves in the direction of blade rotation, i.e., the negative θ-direction, then $N_{\mathrm{D}} > 0$. We should note that for an excitation of the form (2.1) the unsteady flow will be periodic over N_P blade passages, where $N_P = N_B/|N_D|$, $N_D \neq 0$.

The unsteady disturbances in the far upstream and far downstream regions are, in part, prescribed as a fluid dynamic excitation and, in part, depend upon the interaction between the fluid and the blading. Typically, an unsteady aerodynamic excitation is represented by a linear combination of fundamental disturbances that are harmonic in time at relative reduced frequency ω, and in the circumferential direction at angular wave number $\bar{m} = N_D + mN_B$, where m is an interger. The frequency of such an excitation in the stationary or absolute frame is $\omega^{\mathrm{abs}} = \omega - \bar{m}\Omega$, where the term $-\bar{m}\Omega$ accounts for the Doppler shift. In the present study, we will restrict our consideration to unsteady flows driven by prescribed blade motions; therefore, all external aerodynamic excitations are set equal to zero.

3. Fluid Dynamic Equations

In the present discussion, all physical variables are dimensionless. Lengths are scaled with respect to the reference length L^*; time with respect to the ratio L^*/V^* where V^* is the reference flow speed; velocity with respect to V^*; density with respect to a reference density ρ^*; stress, and therefore, pressure, with respect to $\rho^*(V^*)^2$; and specific internal energy with respect to $(V^*)^2$. The superscript $*$ refers to a dimensional reference value of a flow variable. The scalings for the remaining variables can be determined from the equations given below, which have the same general forms as their dimensional counterparts. The reference length, L^*, is typically taken to be the blade chord at the reference radial location r^*_{ref}; the reference fluid density and flow speed, to be the temporally- and circumferentially-averaged inlet density and relative flow speed at $r^* = r^*_{\text{ref}}$, respectively.

3.1 Governing Equations

The field equations that govern the unsteady flow are determined from the conservation laws for mass, momentum and energy, the thermodynamic relations for a perfect gas, and the constitutive relations for a Newtonian fluid. After ensemble averaging these equations and applying an algebraic turbulence model, we arrive at the following form of the Reynolds-averaged Navier-Stokes equations

$$\left.\frac{\partial \tilde{\mathbf{U}}}{\partial t}\right|_{\mathbf{x}} + \frac{\partial}{\partial x_j}(\tilde{\mathbf{F}}_j + \tilde{\mathbf{G}}_j) = \tilde{\mathbf{S}} \ , \tag{3.1}$$

in which a summation over repeated indices is implied.

The state, $\tilde{\mathbf{U}}$, flux, $\tilde{\mathbf{F}}_j$ and $\tilde{\mathbf{G}}_j$, $j = 1, 2, 3$, and source term, $\tilde{\mathbf{S}}$, vectors in equation (3.1), are given by

$$\tilde{\mathbf{U}} = \begin{bmatrix} \tilde{\bar{\rho}} \\ \tilde{\bar{\rho}}\tilde{\mathbf{V}}_{x_1} \\ \tilde{\bar{\rho}}\tilde{\mathbf{V}}_{x_2} \\ \tilde{\bar{\rho}}\tilde{\mathbf{V}}_{x_3} \\ \tilde{\bar{\rho}}\tilde{E}_T \end{bmatrix} , \quad \tilde{\mathbf{F}}_j = \begin{bmatrix} \tilde{\bar{\rho}}\tilde{\mathbf{V}}_{x_j} \\ \tilde{\bar{\rho}}\tilde{\mathbf{V}}_{x_1}\tilde{\mathbf{V}}_{x_j} + \tilde{P}\delta_{1j} \\ \tilde{\bar{\rho}}\tilde{\mathbf{V}}_{x_2}\tilde{\mathbf{V}}_{x_j} + \tilde{P}\delta_{2j} \\ \tilde{\bar{\rho}}\tilde{\mathbf{V}}_{x_3}\tilde{\mathbf{V}}_{x_j} + \tilde{P}\delta_{3j} \\ \tilde{\bar{\rho}}(\tilde{E}_T + \tilde{P}/\tilde{\bar{\rho}})\tilde{\mathbf{V}}_{x_j} \end{bmatrix} , \quad \tilde{\mathbf{G}}_j = \begin{bmatrix} 0 \\ -\tilde{\Pi}_{x_1x_j} \\ -\tilde{\Pi}_{x_2x_j} \\ -\tilde{\Pi}_{x_3x_j} \\ -\tilde{\Pi}_{x_jx_i}\tilde{\mathbf{V}}_{x_i} + \tilde{Q}_{x_j} \end{bmatrix}$$

and

$$\tilde{\mathbf{S}} = \Omega \begin{bmatrix} 0 \\ 0 \\ \tilde{\bar{\rho}}(2\tilde{V}_{x_3} + \Omega x_2) \\ -\tilde{\bar{\rho}}(2\tilde{V}_{x_2} - \Omega x_3) \\ \tilde{\bar{\rho}}\Omega(x_2\tilde{V}_{x_2} + x_3\tilde{V}_{x_3}) \end{bmatrix} , \tag{3.2}$$

where $\tilde{\bar{\rho}}$, $\tilde{\mathbf{V}}$, $\tilde{E}_T = \tilde{E} + \tilde{V}^2/2$ and $\tilde{P} = (\gamma - 1)\tilde{\bar{\rho}}(\tilde{E}_T - \tilde{V}^2/2)$ are the fluid density, relative velocity, relative specific total internal energy, and pressure, respectively, and γ is the fluid specific heat ratio of the fluid. The components of the viscous stress tensor, $\tilde{\mathbf{\Pi}}$, and, assuming Fourier's law for the conduction of heat, those of the heat flux vector, $\tilde{\mathbf{Q}}$, are given by

$$\tilde{\Pi}_{x_ix_j} = \tilde{\bar{\mu}}_{\text{eff}} Re^{-1} \left[\frac{\partial \tilde{V}_{x_i}}{\partial x_j} + \frac{\partial \tilde{V}_{x_j}}{\partial x_i} - 2\frac{\partial \tilde{V}_k}{\partial x_k}\delta_{ij} \right] \tag{3.3}$$

and

$$\tilde{Q}_{x_i} = -\tilde{\bar{\kappa}}_{\text{eff}} Pr^{-1} Re^{-1} \frac{\partial \tilde{T}}{\partial x_i} \ . \tag{3.4}$$

Here $\tilde{T} = \gamma(\tilde{E}_T - \tilde{V}^2/2)$ is the fluid temperature, and Re and Pr are the Reynolds number and Prandtl number, respectively, of the flow. The inviscid flux, $\tilde{\mathbf{F}}_j$, and source term vectors in equation (3.1) can also be written as explicit functions of the state variables; i.e.,

$$\mathbf{F}_j(\tilde{\mathbf{U}}) = \begin{bmatrix} \tilde{U}_{j+1} \\ \tilde{U}_{j+1}\tilde{U}_2/\tilde{U}_1 + \tilde{P}\delta_{1j} \\ \tilde{U}_{j+1}\tilde{U}_3/\tilde{U}_1 + \tilde{P}\delta_{2j} \\ \tilde{U}_{j+1}\tilde{U}_4/\tilde{U}_1 + \tilde{P}\delta_{3j} \\ \tilde{U}_{j+1}(\tilde{U}_5 + \tilde{P})/\tilde{U}_1 \end{bmatrix} \ , \ \tilde{\mathbf{S}}(\tilde{\mathbf{U}}, \mathbf{x}) = \begin{bmatrix} 0 \\ 0 \\ \Omega^2\tilde{U}_1 x_2 + 2\Omega\tilde{U}_4 \\ \Omega^2\tilde{U}_1 x_3 - 2\Omega\tilde{U}_3 \\ \Omega^2(\tilde{U}_3 x_2 + \tilde{U}_4 x_3) \end{bmatrix} \tag{3.5}$$

where $\tilde{P} = (\gamma - 1)[\tilde{U}_5 - \tilde{U}_1^{-1}(\tilde{U}_2^2 + \tilde{U}_3^2 + \tilde{U}_4^2)/2]$.

The matrix equation (3.1) describes the unsteady flow at a moving field point, $\mathbf{x}$, as seen by an observer fixed in a reference frame that rotates at constant velocity, $\boldsymbol{\Omega}$. If we set $\boldsymbol{\Omega} = 0$, we recover an equation that describes the flow in a stationary frame of reference. Equation (3.1) describes the behavior of the ensemble- or Reynolds-averaged values of the time-dependent flow variables. The effects of random turbulent fluctuations have been accommodated by using the effective viscosity, $\tilde{\bar{\mu}}_{\text{eff}} = \tilde{\bar{\mu}} + \tilde{\bar{\epsilon}}$, and the effective thermal conductivity, $\tilde{\bar{\kappa}}_{\text{eff}} = \tilde{\bar{\mu}} + (Pr/Pr_T)\tilde{\bar{\epsilon}}$, where Pr_T is the turbulent Prandtl number, in the definitions of the viscous stress tensor and the heat flux vector, respectively. The molecular viscosity, $\tilde{\bar{\mu}}$, and thermal conductivity, $\tilde{\bar{\kappa}} = \tilde{\bar{\mu}}$, are related to the temperature using Sutherland's Law, the eddy viscosity, $\tilde{\bar{\epsilon}}$, is determined using the Baldwin Lomax [BL78] algebraic turbulence model, and we set $Pr = 0.72$ and $Pr_T = 0.9$.

Transformation to Curvilinear Coordinates

It is convenient to solve the foregoing field equations in terms of body-fitted curvilinear spatial coordinates $(\alpha_1, \alpha_2, \alpha_3)$ and the time $\tau = t$, where the positive directions of α_1, α_2 and α_3 coordinate curves generally point in the streamwise, the spanwise (hub-to-tip) and the pitchwise directions. After introducing the transformation $(\mathbf{x}, t) \rightarrow [\boldsymbol{\alpha}(\mathbf{x}, t), \tau]$ into equation (3.1), we find that

$$\left.\frac{\partial \hat{\tilde{\mathbf{U}}}}{\partial \tau}\right|_{\boldsymbol{\alpha}} + \frac{\partial}{\partial \alpha_j}(\hat{\tilde{\mathbf{F}}}_j + \hat{\tilde{\mathbf{G}}}_j) = \hat{\tilde{\mathbf{S}}} \ , \tag{3.6}$$

where

$$\hat{\tilde{\mathbf{U}}} = J^{-1}\tilde{\mathbf{U}} \ , \quad \hat{\tilde{\mathbf{F}}}_j = J^{-1}\left(\frac{\partial \alpha_j}{\partial t}\tilde{\mathbf{U}} + \frac{\partial \alpha_j}{\partial x_k}\mathbf{F}_k\right) \ , \ \hat{\tilde{\mathbf{G}}}_j = J^{-1}\left(\frac{\partial \alpha_j}{\partial x_k}\tilde{\mathbf{G}}_k\right) \ , \ \hat{\tilde{\mathbf{S}}} = J^{-1}\tilde{\mathbf{S}} \tag{3.7}$$

and J is the Jacobian of the transformation $(\mathbf{x}, t) \rightarrow (\boldsymbol{\alpha}, \tau)$. The Cartesian components of $\tilde{\boldsymbol{\Pi}}$ and $\tilde{\mathbf{Q}}$ are determined from the relations

$$\tilde{\Pi}_{x_i x_j} = \tilde{\bar{\mu}}_{\text{eff}} Re^{-1}\left[\frac{\partial \alpha_k}{\partial x_j}\frac{\partial \tilde{\mathbf{V}}_{x_i}}{\partial \alpha_k} + \frac{\partial \alpha_k}{\partial x_i}\frac{\partial \tilde{\mathbf{V}}_{x_j}}{\partial \alpha_k} - 2\frac{\partial \alpha_m}{\partial x_k}\frac{\partial \tilde{\mathbf{V}}_{x_k}}{\partial \alpha_m}\delta_{ij}/3\right] \tag{3.8}$$

and

$$\tilde{Q}_{x_i} = -\bar{\tilde{\kappa}}_{\text{eff}} Pr^{-1} Re^{-1} \frac{\partial \alpha_j}{\partial x_i} \frac{\partial \tilde{T}}{\partial \alpha_j} \, . \tag{3.9}$$

Boundary Conditions

For turbomachinery applications the field equations (3.1) or (3.6) must be supplemented by boundary conditions at the blade surfaces and at the duct walls, periodicity conditions over N_P blade passages; e.g., $\tilde{\mathbf{V}}(r,\ \theta + 2\pi N_P/N_B,\ \xi) = \mathbf{T}_{N_P}\tilde{\mathbf{V}}(r, \theta, \xi)$, and far-field conditions at the computational inflow ($\xi = \xi_-$) and outflow ($\xi = \xi_+$) boundaries. Since transient unsteady aerodynamic behavior is usually not of interest, a precise knowledge of the initial state of the fluid is not required. No-slip conditions, i.e.,

$$\tilde{\mathbf{V}}^{\text{abs}} = \boldsymbol{\Omega} \times \mathbf{r} + \dot{\boldsymbol{\mathcal{R}}}_{\mathcal{B}_n} \text{ for } x \in \mathcal{B}_n \quad \text{and} \quad \tilde{\mathbf{V}}^{\text{abs}} = 0 \text{ for } r = r_H, r_D \, , \tag{3.10}$$

where $\tilde{\mathbf{V}}^{\text{abs}} = \tilde{\mathbf{V}}^{\text{rel}} + \boldsymbol{\Omega} \times \mathbf{r}$, apply at the blade moving surfaces, $\mathcal{B}_n$, and at the stationary duct walls, respectively. In addition, either the heat flux $\tilde{\mathbf{Q}} \cdot \mathbf{n}_{\mathcal{B}_n}$ or the temperature T must be prescribed at such surfaces. Temporally- and circumferentially-averaged values of the total temperature, the total pressure and the flow angle are specified as functions of radius at the computational inflow boundary, i.e., at $\bar{\xi} = \bar{\xi}_-$, and the temporally- and circumferentially-averaged pressure is specified at the outflow boundary, $\xi = \xi_+$, consistent with radial equilibrium. In general, the unsteady fluctuations at inlet and exit that carry energy towards the blade row must also be specified; those that carry energy away from the blade row must be determined as part of the nonlinear unsteady solution.

3.2 High Reynolds Number Approximations

Thin-Layer Equations

For most flows of practical interest, the Reynolds number (Re) is sufficiently high so that the viscous effects are concentrated within thin layers that lie along the blade surfaces and the duct walls (boundary layers), and extend downstream from the blade trailing edges (wakes). Such flows can be described by approximate field equations, known as the thin-layer, Reynolds-averaged, Navier-Stokes equations, leading to a substantial reduction in the computational resources needed to determine viscous unsteady solutions. The thin-layer equations are derived from (3.6) by assuming that streamwise gradients of the viscous flux terms, i.e., $\partial\hat{\tilde{\mathbf{G}}}_1/\partial\alpha_1$, are small, and hence, can be neglected. In addition, in the α_2 and α_3 directions, normal second derivatives of the velocity components and the temperature are retained, but mixed second derivatives are regarded as negligible.

The field equations resulting from the foregoing approximations have the form

$$\left.\frac{\partial \hat{\tilde{\mathbf{U}}}}{\partial \tau}\right|_{\boldsymbol{\alpha}} + \frac{\partial}{\partial \alpha_j}\hat{\tilde{\mathbf{F}}}_j + \frac{\partial}{\partial \alpha_2}\hat{\tilde{\mathbf{G}}}_2^{TL} + \frac{\partial}{\partial \alpha_3}\hat{\tilde{\mathbf{G}}}_3^{TL} = \tilde{\mathbf{S}} \, , \tag{3.11}$$

where the column vectors $\hat{\tilde{\mathbf{G}}}_2^{TL}$ and $\hat{\tilde{\mathbf{G}}}_3^{TL}$ are the thin-layer approximations to the viscous flux vectors $\hat{\tilde{\mathbf{G}}}_2$ and $\hat{\tilde{\mathbf{G}}}_3$, respectively. The boundary conditions to be used in conjunction with equation (3.11) are the same as those discussed above for the full viscous equations.

Inviscid Flow (Re $\to \infty$)

The field equations that govern the fluid motion in the inviscid limit ($Re \to \infty$), i.e., the Euler equations,

$$\left.\frac{\partial \hat{\tilde{\mathbf{U}}}}{\partial \tau}\right|_{\boldsymbol{\alpha}} + \frac{\partial}{\partial \alpha_j} \hat{\tilde{\mathbf{F}}}_j = \hat{\tilde{\mathbf{S}}} \; , \tag{3.12}$$

are obtained from equation (3.6) by setting $\hat{\tilde{\mathbf{G}}}_j = 0, \; j = 1,2,3$ or from equation (3.11) by setting $\hat{\tilde{\mathbf{G}}}_j^{\mathrm{TL}} = 0, \; j = 2,3$. In principle, the inviscid field equations must be supplemented by jump conditions that apply at vortex-sheet wakes, $\mathcal{W}_m$, and at shocks, $\mathcal{S}h_m$. However, the usual practice is to solve the inviscid field equations over the entire fluid domain, thereby capturing discontinuous wake and shock phenomena. The inviscid flow is then determined as a solution of the Euler equations subject to flow tangency conditions, i.e.,

$$(\tilde{\mathbf{V}}^{\mathrm{abs}} - \boldsymbol{\Omega} \times \mathbf{r} - \dot{\boldsymbol{\mathcal{R}}}_{\mathcal{B}_m}) \cdot \mathbf{n} = 0 \text{ for } \mathbf{x} \in \mathcal{B}_n \quad \text{and} \quad \tilde{\mathbf{V}}^{\mathrm{abs}} \cdot \mathbf{n} = 0 \text{ for } r = r_H, r_B \tag{3.13}$$

at the blade surfaces and the duct walls, respectively. The periodic and far-field conditions, used in the inviscid approximation, are the same as those indicated previously for Navier-Stokes simulations.

3.3 Solution Strategy

We require numerical solutions to the foregoing nonlinear unsteady boundary-value problems over N_P blade passages, where $N_P = N_B/|N_D|$ if $|N_D| \neq 0$ and $N_P = 1$ if $N_D = 0$, to predict the unsteady aerodynamic responses of a blade row to harmonic and circumferentially periodic, unsteady excitations. In the present study, we will seek such solutions for inviscid unsteady flows by matching a wave-split, finite-volume analysis for the unsteady flow in the near field, i.e., in the region $\xi_- \leq \xi \leq \xi_+$, to approximate solutions for the unsteady perturbations of fully-developed, axisymmetric, mean flows in the regions far upstream ($\xi < \xi_-$) and far downstream ($\xi > \xi_+$) of the blade row. Thus, we will solve the nonlinear unsteady equation (3.12) in the near field, a linearized form of this equation in the far-field, and match the near- and far-field solutions at the computational inflow and outflow boundaries.

The displacement field $\boldsymbol{\mathcal{R}}$ is assumed to vary harmonically with time, i.e., $\boldsymbol{\mathcal{R}}(\bar{\mathbf{x}}, t) = Re\{\mathbf{R}(\bar{\mathbf{x}}) \exp(i\omega t)\}$. The complex-amplitude of this field, $\mathbf{R}(\bar{\mathbf{x}})$, must be prescribed over the entire solution domain. In the present study, $\mathbf{R}$ is defined so that the solution domain deforms with the blade motion (i.e., $\mathbf{R} = \mathbf{R}_{\mathrm{B}_n}$ for $\bar{\mathbf{x}} \in \mathrm{B}_n$), slides along the hub and duct walls ($\mathbf{R} \cdot \mathbf{n} = \mathbf{0}$ for $\bar{r} = r_H, r_D$), and remains rigid far from the blade row ($\mathbf{R} \equiv \mathbf{0}$ for $\bar{\xi} \lessgtr \bar{\xi}_\mp$). In addition, $\mathbf{R}(\bar{\mathbf{x}})$ is prescribed along one blade-to-blade periodic boundary, such that it is continuous at the blade leading and trailing edges and decays exponentially away from the blade row. At the other periodic boundary, $\mathbf{R}$ is set so as to satisfy the periodicity condition

$$\mathbf{R}(\bar{r}, \bar{\theta} + 2\pi N_P/N_B, \; \bar{\xi}) = \mathbf{T}_{N_P} \mathbf{R}(\bar{r}, \bar{\theta}, \bar{\xi}) \; . \tag{3.14}$$

In the near field, $\mathbf{R}(\bar{\mathbf{x}})$ is first determined along the hub and duct walls as solutions of Laplace's equation, $\boldsymbol{\nabla}_{\bar{\mathbf{x}}}^2 \mathbf{R} = \mathbf{0}$, in two dimensions. It is then determined in the interior of the computational domain as a solution of Laplace's equation in three dimensions, subject to Dirichlet boundary conditions given above. For the unsteady excitations being considered herein, it is sufficient to solve for the foregoing linear boundary value problems over a single extended blade-passage region, since $\mathbf{R}(\bar{\mathbf{x}})$ can be specified in the remaining passages using the phase-lagged periodicity condition

$$\mathbf{R}(\bar{r},\ \bar{\theta}+2\pi n/N_B,\ \xi)=\mathbf{T}_n R(\bar{r},\ \bar{\theta},\ \bar{\xi})\exp(in\sigma)\ . \tag{3.15}$$

Also, note, that for unsteady flows in which no blades vibrations occur, one would simply set $\mathbf{R}\equiv\mathbf{0}$.

The near-field, finite-volume analysis, which, at present, is performed in the stationary frame in terms of absolute flow variables, is described in §4 of this report. The far-field eigenanalyses, which are performed in the rotating frame in terms of relative flow variables are described in §5. These have been coupled and implemented into the TURBO code, which is demonstrated via the numerical results for inviscid unsteady flows, presented in §6. Although our numerical results pertain only to inviscid flows, we have included viscous equations in this and the following sections to provide a framework for future work.

4. Near-Field, Finite-Volume Analysis

A flux split, finite-volume analysis for nonlinear, inviscid, unsteady flows has been developed [Jan89, JW89, JW90, JHW92], and implemented into the turbomachinery unsteady flow code, TURBO. This analysis was later extended for the prediction of viscous flows [CW93, CCA94]. TURBO is an implicit, multi-block, cell-centered, finite-volume code, that can be used to predict three-dimensional, nonlinear, inviscid and viscous, steady and unsteady flows through and around blade rows. The fluid dynamic equations are solved in a stationary reference frame over a solution domain that rotates with the blade row and deforms with the vibratory blade motions. A brief description of the TURBO analysis is given below. Additional information can be found in the references cited above.

The computational mesh used in TURBO is a sheared H-mesh. This structured mesh defines a curvilinear coordinate system, in which the coordinate curves lie along the boundaries of the physical domain, such that there is a one-to-one correspondence between the points, $\mathbf{x}$, in the physical domain and the points, $\boldsymbol{\alpha}$, in the computational domain. A time-dependent coordinate transformation, $(\mathbf{x}, t) \rightarrow (\boldsymbol{\alpha}, \tau)$, where $\mathbf{x} = \bar{\mathbf{x}} + \boldsymbol{\mathcal{R}}(\bar{\mathbf{x}}, t)$, from the rotating physical domain, in which the grid deforms with the blade motion, to a computational domain, in which the grid is stationary, uniform, and orthogonal, is applied to simplify the implementation of numerical differencing and flow boundary conditions. The α_1, α_2 and α_3 computational coordinates, or the I, J, K computational mesh indices, refer to the axial, spanwise and pitchwise directions, respectively. Cell faces are surfaces of constant computational coordinate, so that each cell is bounded by the six surfaces: $\alpha_1 = I - 1/2$ and $I + 1/2$, and $\alpha_2 = J - 1/2$ and $J + 1/2$, and $\alpha_3 = K - 1/2$ and $K + 1/2$.

4.1 Finite-Volume Equations

For a finite-volume discretization of the governing field equations, the time-dependent geometrical properties of the mesh cells in physical space are required. These include the cell volume, $\vartheta = J^{-1}$, the volume swept out per unit time by the constant α_j face as the cell interface moves, $\dot{\vartheta}_j = J^{-1}\partial\alpha_j/\partial t$, and the area of the constant α_j cell face projected in the x_k direction, $A_{jk} = J^{-1}\partial\alpha_j/\partial x_k$. These geometric properties of a cell are determined from the instantaneous locations of the cell vertices in physical space.

The finite-volume spatial discretization [Jan89, CW93] of equation (3.5), expressed in the stationary frame ($\boldsymbol{\Omega} = \mathbf{0}$), can be written as

$$\partial\hat{\tilde{\mathbf{U}}}/\partial\tau = -\delta_j\hat{\tilde{\mathbf{F}}}_j - \delta_j\hat{\tilde{\mathbf{G}}}_j = -\hat{\tilde{\mathbf{R}}} \tag{4.1}$$

where $\hat{\tilde{\mathbf{U}}} = \vartheta\tilde{\mathbf{U}}$, $\hat{\tilde{\mathbf{F}}}_j = -\dot{\vartheta}_j\tilde{\mathbf{U}} + A_{jk}\tilde{\mathbf{F}}_k$ and $\hat{\tilde{\mathbf{G}}}_j = A_{jk}\tilde{\mathbf{G}}_j$ Here, $\tilde{\mathbf{U}}$ represents an average of the physical state vector over a cell volume; $\hat{\tilde{\mathbf{F}}}_j$ is the inviscid or convective flux and $\hat{\tilde{\mathbf{G}}}_j$ is the viscous or diffusive flux, across a constant α_j cell face; and $\hat{\tilde{\mathbf{R}}}$ is the residual. The flux vectors $\hat{\tilde{\mathbf{F}}}$ and $\hat{\tilde{\mathbf{G}}}$ depend on the physical state varibles and the cell surface properties, and the residual $\hat{\tilde{\mathbf{R}}}$ is a nonlinear function of the physical state vector, $\tilde{\mathbf{U}}$. The operator δ_j in equation (4.1) denotes the difference in the α_j-direction across adjacent cell interfaces, and the repeated j index implies summation over all computational coordinate directions, so that the terms $\delta_j\hat{\hat{\mathbf{F}}}_j$ and $\delta_j\hat{\hat{\mathbf{G}}}_j$ are the net inviscid and viscous fluxes, respectively, through a cell.

The time-derivative in (4.1) is approximated using a second-order, implicit, three-level, backward, difference approximation. After applying this scheme and separating the time dependence of the state vector and the cell volume, we find that

$$\hat{\vartheta}\Delta\tilde{\mathbf{U}}^n + \hat{\hat{\mathbf{R}}}^{n+1} = \mathcal{G}^{n+1} = \vartheta^{n-1}\Delta\tilde{\mathbf{U}}^{n-1}/2\Delta\tau - \tilde{\mathbf{U}}^n(3\vartheta^{n+1} - 4\vartheta^n + \vartheta^{n-1})/2\Delta\tau \ , \qquad (4.2)$$

where $\hat{\vartheta} = 3\vartheta^{n+1}/2\Delta\tau$, $\Delta\tilde{\mathbf{U}}^n = \tilde{\mathbf{U}}^{n+1} - \tilde{\mathbf{U}}^n$, the vector $\mathcal{G}^{n+1}$ is determined by the terms on the right-hand side of (4.2), and the superscript n refers to the nth time level. The nonlinear equation (4.2) is solved at each time step using a Newton iteration procedure in which the viscous flux terms are treated explicitly, i.e., we set

$$\hat{\vartheta}\Delta\tilde{\mathbf{U}}^p + \delta_j\left(\partial\hat{\hat{\mathbf{F}}}_j/\partial\tilde{\mathbf{U}}\Big|_{\tilde{\mathbf{U}}^{p-1}}\Delta\tilde{\mathbf{U}}^p\right) = \hat{\vartheta}(\tilde{\mathbf{U}}^{p-1} - \tilde{\mathbf{U}}^n) - \hat{\hat{\mathbf{R}}}^{p-1} + \mathcal{G}^{n+1} \ . \qquad (4.3)$$

where $p = 1, 2, \ldots$, is the Newton iteration index, $\tilde{\mathbf{U}}^0 = \tilde{\mathbf{U}}^n$, $\Delta\tilde{\mathbf{U}}^p = \tilde{\mathbf{U}}^p - \tilde{\mathbf{U}}^{p-1}$, and $\tilde{\mathbf{U}}^p$ is the Newton update to the state vector. Once the Newton iteration converges $\Delta\tilde{\mathbf{U}}^p \equiv 0$, and $\tilde{\mathbf{U}}^p \equiv \tilde{\mathbf{U}}^{n+1}$.

4.2 Evaluation of Flux Terms

To simplify the description of the spatial discretizations that are used to evaluate the flux terms that appear in (4.3), we consider a "one-dimensional inviscid flow" in which, for example, $\hat{\hat{\mathbf{F}}}_j = \hat{\hat{\mathbf{F}}}$ is the inviscid flux vector in the $\alpha_j = \alpha$ computational coordinate direction. The subscript J will refer to the cell volume bounded by the cell surfaces at $\alpha = J + 1/2$ and $\alpha = J - 1/2$. Extensions of the equations that follow to multi-dimensional flows are straightforward conceptually, but involve the use of tedious additional nomenclature.

A cell-centered finite-volume discretization requires that flux information at say the $J+1$ cell interface be computed in terms of the values of the state variables, $\tilde{\mathbf{U}}_J$ and $\tilde{\mathbf{U}}_{J+1}$, in the neighboring cell volumes and the geometric properties of the grid, i.e., $\dot{\vartheta}_{J+1/2}$ and $A_{J+1/2}$, at the cell interface. In the TURBO analysis, a flux splitting technique is applied to evaluate the interfacial inviscid fluxes. It is based on a similarity transformation and an eigenvalue decomposition, of the flux Jacobian matrix, $\partial\hat{\hat{\mathbf{F}}}/\partial\tilde{\mathbf{U}}$, into matrices that account for right (+) and left (−) traveling disturbances.

Thus, the matrix $\partial\hat{\hat{\mathbf{F}}}/\partial\tilde{\mathbf{U}}|_{\tilde{\mathbf{U}}_J, G_{J+1/2}}$, where the subscripts indicate that the flux Jacobian matrix is evaluated in terms of the state vector in Jth cell and the surface metrics, indicated by $G_{J+1/2}$, at the $(J + 1/2)$th cell interface, is split according to

$$\frac{\partial\hat{\hat{\mathbf{F}}}}{\partial\tilde{\mathbf{U}}}\bigg|_{\tilde{\mathbf{U}}_J, G_{J+1/2}} = \frac{\partial\hat{\hat{\mathbf{F}}}}{\partial\tilde{\mathbf{U}}}\bigg|^{+}_{\tilde{\mathbf{U}}_J, G_{J+1/2}} + \frac{\partial\hat{\hat{\mathbf{F}}}}{\partial\tilde{\mathbf{U}}}\bigg|^{-}_{\tilde{\mathbf{U}}_J, G_{J+1/2}} = \hat{\hat{\mathbf{T}}}(\hat{\hat{\mathbf{\Lambda}}}^{+} + \hat{\hat{\mathbf{\Lambda}}}^{-})\hat{\hat{\mathbf{T}}}^{-1}\bigg|_{\tilde{\mathbf{U}}_J, G_{J+1/2}} \ , \qquad (4.4)$$

where the matrices $\hat{\hat{\mathbf{T}}}$ and $\hat{\hat{\mathbf{T}}}^{-1}$ contain the right and left eigenvectors, respectively, of $\partial\hat{\hat{\mathbf{F}}}/\partial\hat{\mathbf{U}}$, and $\hat{\hat{\mathbf{\Lambda}}}^{+}$ and $\hat{\hat{\mathbf{\Lambda}}}^{-}$ are diagonal matrices containing the positive (+) and negative (−) eigenvalues. The eigenvalues of the flux Jacobian matrix are used to determine which characteristic modes are taken into account, thus controlling the direction of spatial differencing.

Two different approximations are applied to evaluate interfacial, inviscid, flux information. One is based on flux vector splitting [SW81], and is used to evaluate the left-hand side flux terms in (4.3). This approximation is only first-order accurate, but allows for a convenient approximate factorization of equation (4.3), which facilitates the time-marching solution. The other is based on flux difference splitting [Roe81], and is used to evaluate the right-hand side inviscid flux terms. In TURBO, Roe's first-order accurate, flux-difference splitting approximation is modified, by adding corrective fluxes, to achieve higher order spatial accuracy.

Left-Hand-Side Flux Terms

The flux-vector splitting approximation to the Newton update to the inviscid flux vector at the $J+1/2$ cell interface is

$$\left(\left.\frac{\partial\hat{\tilde{\mathbf{F}}}}{\partial\tilde{\mathbf{U}}}\right|_{\tilde{\mathbf{U}}^{p-1}}\Delta\tilde{\mathbf{U}}^{p}\right)_{J+1/2} = \left.\frac{\partial\hat{\tilde{\mathbf{F}}}}{\partial\tilde{\mathbf{U}}}\right|^{+}_{\tilde{\mathbf{U}}^{p-1}_{J},G^{n+1}_{J+1/2}}\Delta\tilde{\mathbf{U}}^{p}_{J} + \left.\frac{\partial\hat{\tilde{\mathbf{F}}}}{\partial\tilde{\mathbf{U}}}\right|^{-}_{\tilde{\mathbf{U}}^{p-1}_{J+1},G^{n+1}_{J+1/2}}\Delta\tilde{\mathbf{U}}^{p}_{J+1}\ , \tag{4.5}$$

where the subscripts on the right-hand-side, flux Jacobian matrices indicate that these matrices are evaluated in terms of the state vector, $\tilde{\mathbf{U}}^{p-1}$, in the indicated cell volume, J or $J+1$, and the swept volume and surface area at the $n+1$ time level and the $J+1/2$ cell interface. The approximation (4.5) results in first order spatial accuracy, but it is only used to construct an approximate factorization of the Newton iteration equation (4.3). Therefore, any errors that are introduced, do not appear in the converged final solution.

The terms in (4.5) are spatially differenced in the α-direction to determine the Newton update to the net inviscid flux through the Jth cell volume; i.e,

$$\begin{aligned}\delta\left(\left.\frac{\partial\hat{\tilde{\mathbf{F}}}}{\partial\tilde{\mathbf{U}}}\right|_{\tilde{\mathbf{U}}^{p-1}}\Delta\tilde{\mathbf{U}}^{p}\right)\Bigg|_{J} &= \left.\frac{\partial\hat{\tilde{\mathbf{F}}}}{\partial\tilde{\mathbf{U}}}\right|^{+}_{\tilde{\mathbf{U}}^{p-1}_{J},G^{n+1}_{J+1/2}}\Delta\tilde{\mathbf{U}}^{p}_{J} + \left.\frac{\partial\hat{\tilde{\mathbf{F}}}}{\partial\tilde{\mathbf{U}}}\right|^{-}_{\tilde{\mathbf{U}}^{p-1}_{J+1},G^{n+1}_{J+1/2}}\Delta\tilde{\mathbf{U}}^{p}_{J+1} \\ &- \left.\frac{\partial\hat{\tilde{\mathbf{F}}}}{\partial\tilde{\mathbf{U}}}\right|^{+}_{\tilde{\mathbf{U}}^{p-1}_{J-1},G^{n+1}_{J-1/2}}\Delta\tilde{\mathbf{U}}^{p}_{J-1} - \left.\frac{\partial\hat{\tilde{\mathbf{F}}}}{\partial\tilde{\mathbf{U}}}\right|^{-}_{\tilde{\mathbf{U}}^{p-1}_{J},G^{n+1}_{J-1/2}}\Delta\tilde{\mathbf{U}}^{p}_{J}\ ,\end{aligned} \tag{4.6}$$

to determine the net flux through the Jth cell volume.

Right-Hand Side Inviscid Flux Terms

The inviscid flux vectors that appear in the residual on the right-hand side of (4.3) are evaluated using flux difference splitting [Roe81]. In TURBO, the flux, $\hat{\tilde{\mathbf{F}}}_{J+1/2}$, at the $J+1/2$ cell interface is evaluated in terms of the flux in the cell to the left (J) of the interface and the flux due to waves approaching the interface from the right. Thus, we set

$$\hat{\tilde{\mathbf{F}}}_{J+1/2} = \hat{\tilde{\mathbf{F}}}(\tilde{\mathbf{U}}_{J},G_{J+1/2}) + \left.\frac{\partial\hat{\tilde{\mathbf{F}}}}{\partial\tilde{\mathbf{U}}}\right|^{-}_{\tilde{\mathbf{U}}^{\mathrm{Roe}}_{J+1/2},G_{J+1/2}}(\tilde{\mathbf{U}}_{J+1}-\tilde{\mathbf{U}}_{J})\ , \tag{4.7}$$

where $\hat{\bar{\mathbf{F}}}(\tilde{\mathbf{U}}_J, G_{J+1/2})$ is a flux based on the state vector in the Jth cell and the cell metrics, $\dot{\vartheta}$ and A, at the $J+1/2$ cell interface, and the flux Jacobian matrix $\partial\hat{\bar{\mathbf{F}}}/\partial\tilde{\mathbf{U}}|_{\tilde{\mathbf{U}}^{\mathrm{Roe}}_{J+1/2,G_J+1/2}}$ is evaluated in terms of the intermediate state vector, $\tilde{\mathbf{U}}^{\mathrm{Roe}}_{J+1/2}$, and the cell metrics at the $J+1/2$ interface. The intermediate state vector, $\tilde{\mathbf{U}}^{\mathrm{Roe}}_{J+1/2}$, is defined using the relations:

$$\tilde{\bar{\rho}}^{\mathrm{Roe}}_{J+1/2} = \sqrt{\tilde{\bar{\rho}}_J \tilde{\bar{\rho}}_{J+1}}\ , \quad \tilde{\mathbf{V}}^{\mathrm{Roe}}_{J+1/2} = \frac{\sqrt{\tilde{\bar{\rho}}_J}\,\tilde{\mathbf{V}}_J + \sqrt{\tilde{\bar{\rho}}_{J+1}}\,\tilde{\mathbf{V}}_{J+1}}{\sqrt{\tilde{\bar{\rho}}_J} + \sqrt{\tilde{\bar{\rho}}_{J+1}}}\ ,$$

and

$$\tilde{E}^{\mathrm{Roe}}_{T,J+1/2} = \frac{\sqrt{\tilde{\bar{\rho}}_J}\,\tilde{E}_{T,J} + \sqrt{\tilde{\bar{\rho}}_{J+1}}\,\tilde{E}_{T,J+1}}{\sqrt{\tilde{\bar{\rho}}_J} + \sqrt{\tilde{\bar{\rho}}_{J+1}}}\ . \tag{4.8}$$

The discrete approximation (4.7) is first-order accurate, since the interfacial fluxes are based only upon information from adjacent cells. Higher order spatial accuracy can be achieved by adding corrective fluxes to the right-hand side of (4.7), which bring in information from additional neighboring cells. The corrective perturbation flux at the $J+1/2$ interface is comprised of right traveling waves at the upstream interface, $J-1/2$, of the Jth cell and left traveling waves at the downstream interface, $J+3/2$, of the $(J+1)$th cell. These waves are approximated using the Roe-averaged, flux Jacobian matrix at the $J+1/2$ interface. Thus, the enhanced approximation to the perturbation flux is obtained by adding terms of the form

$$\frac{1}{2}\,\frac{\partial\hat{\bar{\mathbf{F}}}}{\partial\tilde{\mathbf{U}}}\bigg|^{+}_{\tilde{\mathbf{U}}^{\mathrm{Roe}}_{J+1/2},\bar{A}_{J+1/2}} (\tilde{\mathbf{U}}_J - \tilde{\mathbf{U}}_{J-1}) \quad \text{and} \quad -\frac{1}{2}\,\frac{\partial\hat{\bar{\mathbf{F}}}}{\partial\tilde{\mathbf{U}}}\bigg|^{-}_{\tilde{\mathbf{U}}^{\mathrm{Roe}}_{J+1/2},\bar{A}_{J+1/2}} (\tilde{\mathbf{U}}_{J+2} - \tilde{\mathbf{U}}_{J+1})$$

to the right-hand side of (4.7), which should result in second order spatial accuracy. Flux limiters [VL74] are used in conjunction with the corrective fluxes to control dispersive errors, such as those that occur at shocks and at stagnation points. The limiters are activated by changes in sign in the jumps in the characteristic variables at adjacent interfaces.

Once the interfacial fluxes have been computed, they are spatially differenced, i.e.,

$$\delta\hat{\bar{\mathbf{F}}}\Big|_J = \hat{\bar{\mathbf{F}}}_{J+1/2} - \hat{\bar{\mathbf{F}}}_{J-1/2}\ , \tag{4.9}$$

to compute the net inviscid flux through the Jth control volume. A second-order discrete approximation is used to evaluate the interfacial fluxes in (4.9). Note that in computing the residual at the $p-1$ Newton iteration level, the flux vectors in (4.9) are evaluated in terms of the state variables at the $p-1$ iteration level and the grid properties at the $n+1$ time level.

Right-Hand Side Viscous Flux Terms

At each step of the Newton iteration procedure, the viscous flux vector, $\hat{\bar{\mathbf{G}}}$, is evaluated at the cell interfaces in terms of the values of the flow variables, at the $p-1$ iteration level, in the cell volumes to the left and right of the interface and the area of the cell interface at the $n+1$ time level. The individual terms that make up this vector are considered separately. Derivatives of the fluid properties at cell interfaces are evaluated in terms of the property values in the cell volumes to the left and right of the interface, using central difference approximations; the velocities at cell interfaces, by averaging their values in the adjacent cell volumes. Once the viscous fluxes at the cell interfaces have been computed, they are spatially differenced according to

$$\delta\bar{\bar{\tilde{\mathbf{G}}}}\Big|_J = \bar{\bar{\tilde{\mathbf{G}}}}_{J+1/2} - \bar{\bar{\tilde{\mathbf{G}}}}_{J-1/2} \tag{4.10}$$

to compute the net viscous flux through the cell volume.

4.3 Solution Procedure

The spatial difference approximation (4.6) leads to an approximate factorization of the Newton iteration equation (4.3) of the form

$$\hat{\bar{\mathbf{D}}}_J\Delta\tilde{\mathbf{U}}^p_J - \hat{\bar{\mathbf{M}}}^+_{J-1}\Delta\tilde{\mathbf{U}}^p_{J-1} + \hat{\bar{\mathbf{M}}}^-_{J+1}\Delta\tilde{\mathbf{U}}^p_{J+1} = -\hat{\vartheta}_J(\tilde{\mathbf{U}}^{p-1}_J - \tilde{\mathbf{U}}^n_J) - \hat{\bar{\mathbf{R}}}^{p-1}_J + \mathcal{G}^{n+1}_J\ , \tag{4.11}$$

where the index J refers to the Jth computational cell and the $\hat{\bar{\mathbf{D}}}$ and $\hat{\bar{\mathbf{M}}}$ matrices are evaluated based on the state vector $\tilde{\mathbf{U}}^{p-1}$. The $\hat{\bar{\mathbf{D}}}$ matrix contains the diagonal elements of the iteration matrix, and the $\hat{\bar{\mathbf{M}}}^+$ and $\hat{\bar{\mathbf{M}}}^-$ matrices contain the off-diagonal elements in the negative and positive computational coordinate directions, respectively, i.e.,

$$\begin{aligned}
\hat{\bar{\mathbf{D}}}_J &= \hat{\vartheta}_J\mathbf{I} + \frac{\partial\hat{\bar{\mathbf{F}}}}{\partial\tilde{\mathbf{U}}}\bigg|^+_{\tilde{\mathbf{U}}^{p-1}_J,G^{n+1}_{J+1/2}} - \frac{\partial\hat{\bar{\mathbf{F}}}}{\partial\tilde{\mathbf{U}}}\bigg|^-_{\tilde{\mathbf{U}}^{p-1}_J,G^{n+1}_{J-1/2}}\ , \\
\hat{\bar{\mathbf{M}}}^+_{J-1} &= \frac{\partial\hat{\bar{\mathbf{F}}}}{\partial\tilde{\mathbf{U}}}\bigg|^+_{\tilde{\mathbf{U}}^{p-1}_{J-1},G^{n+1}_{J-1/2}} \quad \text{and} \quad \hat{\mathbf{M}}^-_{J+1} = \frac{\partial\hat{\bar{\mathbf{F}}}}{\partial\tilde{\mathbf{U}}}\bigg|^-_{\tilde{\mathbf{U}}^{p-1}_{J+1},G^{n+1}_{J+1/2}}
\end{aligned} \tag{4.12}$$

To reduce the errors introduced by the approximate factorization, equation (4.11) is solved for $\Delta\tilde{\mathbf{U}}^p$ using a symmetric Gauss-Seidel subiteration procedure. The first subiteration is over positive grid indices; the second, over negative grid indices. The subiteration procedure is thus an *LU* decomposition of the Newton iteration matrix, with forward and backward substitution. Once the Gauss-Seidel subiteration procedure converges, equation (4.3) is satisfied, and the calculation proceeds to the next Newton-iteration level. As the solution at time $\tau = \tau^{n+1}$ converges, any errors introduced by the Newton iteration or the approximate factorization vanish. Only the errors in the calculation of the residual of equation (4.1) remain. The terms that make up this residual are calculated using second-order accurate difference approximations.

Boundary Conditions

The field equation (4.1) must be solved subject to conditions at the boundaries of the near-field computational domain. The flow tangency conditions used in the inviscid version of TURBO, cf. (3.13), are implemented by using phantom cells inside a solid surface. The density and pressure in a phantom cell are defined by a first-order accurate reflection condition, and the phantom cell velocity is defined such that the velocity at a solid surface, which is the average of the velocities in the phantom and the interior cells, satisfies the flow tangency condition, in a manner consistent with the finite volume discretization. Periodicity conditions; e.g., $\tilde{\mathbf{V}}_U = \tilde{\mathbf{T}}_{\mathrm{N_P}}\tilde{\mathbf{V}}_{\mathrm{L}}$, where the subscripts U and L refer to the upper and lower periodic boundaries of the computational domain, are imposed at the pitchwise boundaries. Finally, as discussed in the next section, analytic/numeric far-field solutions, based on reduced forms of the governing equations, are matched to the numerical near-field solution at the computational inflow and outflow boundaries ($\xi = \xi_{\mp}$).

The current TURBO implementation uses explicit boundary conditions, which are incorporated into the SGS iteration procedure, so that the boundary conditions are imposed in a semi-implicit manner. This treatment has been found to yield better convergence properties than a purely explicit implementation.

5. Far-Field Eigenanalyses

Far-field solutions, based on reduced sets of governing equations, can be applied to restrict axial extent of the near-field computational domain. To develop such solutions, we require an inviscid form of the field equation (3.1), that applies at fixed locations ($\mathbf{x} = \bar{\mathbf{x}}$) in the rotating frame. Expressed in terms of fluid dynamic variables, $\tilde{\mathbf{V}}$ and $\tilde{E}_T$, measured relative to a reference frame that rotates with the blade row and in terms of rotating cylindrical coordinates, this equation has the form

$$\left.\frac{\partial \tilde{\mathbf{U}}}{\partial t}\right|_{\mathbf{x}} + r^{-1}\frac{\partial r\tilde{\mathbf{F}}_r}{\partial r} + r^{-1}\frac{\partial \tilde{\mathbf{F}}_\theta}{\partial \theta} + \frac{\partial \tilde{\mathbf{F}}_\xi}{\partial \xi} = \tilde{\mathbf{S}} \, , \tag{5.1}$$

where the state and source-term vectors in equation (5.1) are given by

$$\tilde{\mathbf{U}} = \left\{ \begin{array}{c} \tilde{\rho} \\ \tilde{\rho}\tilde{V}_r \\ \tilde{\rho}\tilde{V}_\theta \\ \tilde{\rho}\tilde{V}_\xi \\ \tilde{\rho}\tilde{E}_T \end{array} \right\}, \qquad \tilde{\mathbf{S}} = r^{-1} \left\{ \begin{array}{c} 0 \\ (\tilde{U}_3)^2/\tilde{U}_1 + \tilde{P} \\ -\tilde{U}_2\tilde{U}_3/\tilde{U}_1 \\ 0 \\ 0 \end{array} \right\} + \Omega \left\{ \begin{array}{c} 0 \\ 2\tilde{U}_3 + \tilde{U}_1\Omega r \\ -2\tilde{U}_2 \\ 0 \\ \tilde{U}_2\Omega r \end{array} \right\} . \tag{5.2}$$

The flux vectors $\tilde{\mathbf{F}}_r(\tilde{\mathbf{U}})$, $\tilde{\mathbf{F}}_\theta(\tilde{\mathbf{U}})$ and $\tilde{\mathbf{F}}_\xi(\tilde{\mathbf{U}})$ and the pressure $P(\tilde{\mathbf{U}})$ have functional forms similar to those indicated previously for the $\tilde{\mathbf{F}}_j(\tilde{\mathbf{U}})$, $j = 1,2,3$, and $\tilde{P}(\tilde{\mathbf{U}})$ in §3.1.

5.1 Unsteady Perturbations in the Far Field

To determine approximate solutions to equation (5.1), that describe the flows far upstream ($\xi < \xi_-$) and far downstream ($\xi > \xi_+$) of a blade row, we first expand the unsteady state vector, $\tilde{\mathbf{U}}$, into an asymptotic series of the form

$$\tilde{\mathbf{U}}[\mathbf{x}, t] = \mathbf{U}(\mathbf{x}) + \tilde{\mathbf{u}}(\mathbf{x}, t) + \ldots = \mathbf{U}(\mathbf{x}) + Re\{\mathbf{u}(\mathbf{x})\exp(i\omega t)\} + \ldots \, , \tag{5.3}$$

where the column vectors $\mathbf{U}(\mathbf{x})$ and $\tilde{\mathbf{u}}(\mathbf{x}, t)$ contain the conservation variables for the zeroth-order background flow, which is steady in the rotating frame, and the first-order unsteady perturbation, respectively, and the dots refer to higher order terms. The components of the vector $\mathbf{u}$ are the complex amplitudes of the first-order unsteady conservation variables, i.e., $\mathbf{u}^T = [\rho,\ \bar{\rho}v_r + \rho V_r,\ \bar{\rho}v_\theta + \rho V_\theta,\ \bar{\rho}v_\xi + \rho V_\xi,\ \bar{\rho}e_T + \rho E_T]$ where $\bar{\rho}$, $\mathbf{V}$ and E_T and ρ, $\mathbf{v}$, and e_T are the steady and the complex amplitudes of the first-order unsteady, primitive, flow variables, respectively. The unsteady flux, say $\tilde{\mathbf{F}}_r$, and source term, $\tilde{\mathbf{S}}$, vectors are approximated using Taylor series expansions about the mean flow state, $\mathbf{U}$, i.e.,

$$\tilde{\mathbf{F}}_r(\tilde{\mathbf{U}}) = \mathbf{F}_r(\mathbf{U}) + \frac{\partial \mathbf{F}_r}{\partial \mathbf{U}}\tilde{\mathbf{u}} + \ \ldots \quad \text{and} \quad \tilde{\mathbf{S}}(\tilde{\mathbf{U}}) = \mathbf{S}(\mathbf{U}) + \frac{\partial \mathbf{S}}{\partial \mathbf{U}}\tilde{\mathbf{u}} + \ \ldots \, . \tag{5.4}$$

Field equations, that describe the steady and the first-order unsteady flows in the far upstream and far downstream regions, are determined by substituting the foregoing series expansions into the nonlinear, time-dependent equation (5.1), and equating terms of like order. The resulting equations for the zeroth- and first-order flows are

$$r^{-1}\frac{\partial r\mathbf{F}_r}{\partial r}+r^{-1}\frac{\partial \mathbf{F}_\theta}{\partial \theta}+\frac{\partial \mathbf{F}_\xi}{\partial \xi}=\mathbf{S} \tag{5.5}$$

and

$$i\omega\mathbf{u}+r^{-1}\frac{\partial(r\mathbf{A}\mathbf{u})}{\partial r}+r^{-1}\frac{\partial \mathbf{B}\mathbf{u}}{\partial \theta}+\frac{\partial \mathbf{C}\mathbf{u}}{\partial \xi}-\mathbf{D}\mathbf{u}=0\ , \tag{5.6}$$

respectively, where $\mathbf{A}=\partial\mathbf{F}_r\ /\partial\mathbf{U}$, $\mathbf{B}=\partial\mathbf{F}_\theta\ /\partial\mathbf{U}$ and $\mathbf{C}=\partial\mathbf{F}_\xi\ /\partial\mathbf{U}$ are flux Jacobian matrices and $\mathbf{D}=\partial\mathbf{S}\ /\partial\mathbf{U}$ is the source-term Jacobian.

We assume that, far from the blade row, the mean or steady flow quantities are dependent only on radial position; i.e., $\bar{\rho}=\bar{\rho}(r)$, $P=P(r)$, etc., and that the radial component of the steady velocity is negligible; i.e., $\mathbf{V}=V_\theta(r)\mathbf{e}_\theta+V_\xi(r)\mathbf{e}_\xi$. Under these conditions, the steady field equation (5.5) reduces to

$$\bar{\rho}^{-1}\frac{dP}{dr}=r^{-1}V_\theta^2+2\Omega V_\theta+\Omega^2 r=r^{-1}(V_\theta^{\text{abs}})^2\ , \tag{5.7}$$

where $V_\theta^{\text{abs}}=V_\theta+\mathbf{\Omega}\times r$ is the absolute circumferential velocity. We also assume that the kinematic and thermodynamic data needed, in conjunction with (5.7), to completely specify the steady background flow in the far field are available.

For the mean flow conditions just described, the linearized unsteady equation (5.6) reduces to

$$i\omega\mathbf{u}+r^{-1}\frac{\partial(r\mathbf{A}_2\mathbf{u})}{\partial r}+r^{-1}\mathbf{B}_2\frac{\partial \mathbf{u}}{\partial \theta}+\mathbf{C}_2\frac{\partial \mathbf{u}}{\partial \xi}-\mathbf{D}\mathbf{u}=0\ , \tag{5.8}$$

where the subscript 2 on the Jacobian matrices in (5.8) indicates that they are evaluated at $U_2=\bar{\rho}V_r=0$; e.g., $\mathbf{A}_2\equiv\partial\mathbf{F}_r/\partial\mathbf{U}|_{U_2=0}$.

Uniform Mean Flow

For the special case of a uniform mean flow, in the absolute frame, i.e., $V_\theta^{\text{abs}}=0$ and V_ξ is a constant, an exact solution can be determined for the first-order unsteady perturbation. This solution indicates that an arbitrary unsteady disturbance can be represented as the sum of independent entropic, vortical and irrotational acoustic disturbances. A state vector, $\mathbf{u}_C$, representing a linear combination of entropic and vortical disturbances is a solution of (5.8) that satisfies the convection equation $\bar{D}\mathbf{u}_C/Dt=(i\omega+\mathbf{V}\cdot\mathbf{\nabla})\mathbf{u}_C=0$. Thus, such disturbances are convected by the mean flow, and, for an unsteady flow occurring at temporal frequency ω in the rotating frame, $\mathbf{u}_C$ has a general solution of the form

$$\mathbf{u}_C=\sum_{m=-\infty}^{\infty}\mathbf{u}_m(r)\exp[i(\kappa_{\xi,m}\xi+\bar{m}\theta)]\ . \tag{5.9}$$

Here, the $\mathbf{u}_m$ are arbitrary functions of radius, $\bar{m}=N_{\text{D}}+mN_B$ and $\kappa_{\xi,m}=-(\omega-\bar{m}\Omega_{\text{x}})V_\xi^{-1}=-\omega_m^{\text{abs}}V_\xi^{-1}$, are the circumferential angular and axial linear wave numbers of the mth disturbance, and $\omega_m^{\text{abs}}=\omega-\bar{m}\Omega_{\text{x}}$ is the temporal frequency of the mth disturbance as seen by an observer fixed in the absolute frame.

The acoustic disturbances are governed by a convected wave equation for the unsteady pressure, which can be solved analytically [TS62]. The resulting solution for the complex-amplitude of the unsteady pressure in a subsonic axial mean flow is

$$p = \sum_{m=-\infty}^{\infty} e^{i\bar{m}\theta} \sum_{\mu=0}^{\infty} \left[p_{m\mu}^{-} \exp(\chi_{m\mu}^{-}\xi) + p_{m\mu}^{+} \exp(\chi_{m\mu}^{+}\xi)\right] E_{m\mu}(r) \; . \tag{5.10}$$

Here $p_{m\mu}^{\mp}$ are the amplitudes of the downstream and upstream traveling pressure waves, and $E_{m\mu}(r) = J_{\bar{m}}(k_{m\mu}r) + Q_{m\mu}Y_{\bar{m}}(k_{m\mu}r)$ are the "characteristic E-functions" of [TS62]. The E-functions are combinations of Bessel functions, of order $\bar{m}$, of the first and second kinds. The constants $k_{m\mu}$ and $Q_{m\mu}$ in (5.10) are determined by the duct-wall boundary conditions, and the index $\mu = 0, 1, 2, \ldots$ indicates the number of zero crossings or nodes in the μth radial mode.

The axial exponential coefficients, $\chi_{m\mu}^{\mp} = \beta_{m\mu}^{\mp} + i\kappa_{\xi,m\mu}^{\mp}$, are given by

$$\chi_{m\mu}^{\mp} = \left(1 - M_{\xi}^{2}\right)^{-1} A^{-1} \left[iM_{\xi}\omega_{m}^{\text{abs}} \mp \sqrt{(1 - M_{\xi}^{2})A^{2}k_{m\mu}^{2} - (\omega_{m}^{\text{abs}})^{2}}\,\right] \; , \tag{5.11}$$

where $M_{\xi} = V_{\xi}/A < 1$ is the mean axial Mach number. If $(\omega_{m}^{\text{abs}})^{2} > (1 - M_{\xi}^{2})A^{2}k_{m\mu}^{2}$, then the $\chi_{m\mu}^{\mp}$ are purely imaginary, and the $m\mu^{\text{th}}$ pressure patterns propagate. If the $\chi_{m\mu}^{\mp}$ are complex, then one pattern attenuates, and the other grows exponentially, with axial distance.

The perturbation state vector for acoustic disturbances is given by

$$\mathbf{u}_{A} = \sum_{m=-\infty}^{\infty} e^{i\bar{m}\theta} \sum_{\mu=0}^{\infty} \left[\mathbf{u}_{m\mu}^{-} \exp\left(\chi_{m\mu}^{-}\xi\right) + \mathbf{u}_{m\mu}^{+} \exp\left(\chi_{m\mu}^{+}\xi\right)\right] \; , \tag{5.12}$$

where the modal state vectors, $\mathbf{u}_{m\mu}^{\mp}(r)$, are determined, in terms of the pressure, from the linearized unsteady field equations. Note that, in addition to different axial behaviors, the acoustic disturbances in (5.12) and the convected disturbances in (5.9) have different radial behaviors. The former occur in radial modes, the shapes of which are determined by the unsteady field equations, whereas the latter have arbitrary radial dependence.

Nonuniform Mean Flow

Guided by the exact solutions for uniform mean flows, approximate solutions to the linearized unsteady equation (5.8) can be constructed for nonuniform steady background flows [MV97]. For this purpose, we set $\mathbf{u} = \mathbf{u}_{C} + \mathbf{u}_{W}$, where $\mathbf{u}_{C}$ describes the convected disturbance field, and

$$\mathbf{u}_{W} = \sum_{m=-\infty}^{\infty} \exp(i\bar{m}\theta) \sum_{n=0}^{\infty} a_{mn}\mathbf{u}_{mn}^{R}(r) \exp(\chi_{mn}\xi) \; , \tag{5.13}$$

describes a series of modal type disturbances. The summation over n in (5.13) includes different possible types of modes, such as upstream or downstream traveling modes as well as modes with different numbers of radial zero crossings.

The convected disturbance is a solution to equation (5.8) of the form (5.9), but, for nonuniform mean flows, the axial wave numbers, $\kappa_{\xi,m}(r) = -[\omega + \bar{m}r^{-1}V_{\theta}(r)]/V_{\xi}(r)$, are functions of radius. The convected field may contain entropic and/or vortical disturbances, depending on the properties of the mean flow. However, for a general nonisentropic, rotational mean flow, no convected field will exist.

The modal disturbances are determined by substituting the assumed form of the solution, (5.13), into the field equation (5.8), yielding the system

$$i\omega \mathbf{I}\, \mathbf{u}^R_{mn} + r^{-1}\frac{\partial}{\partial r}\left(r\mathbf{A}_2\, \mathbf{u}^R_{mn}\right) + i\bar{m}r^{-1}\mathbf{B}_2\, \mathbf{u}^R_{mn} + \chi_{mn}\mathbf{C}_2\, \mathbf{u}^R_{mn} - \mathbf{D}_2\, \mathbf{u}^R_{mn} = \mathbf{0}\ , \tag{5.14}$$

which must be solved numerically. After discretizing (5.14), and applying the hub- and duct-wall boundary conditions, $v_r = 0$ for $r = r_H, r_D$, we obtain the matrix equation

$$(\mathbf{P} - \chi_{mn}\mathbf{C}_2)\, \mathbf{u}^R_{mn} = \mathbf{0} \tag{5.15}$$

where $\mathbf{P} = -i\omega\mathbf{I} - \mathbf{L}(r, \mathbf{A}_2) - i\bar{m}r^{-1}\,\mathbf{B}_2 + \mathbf{D}_2$ and $\mathbf{L}(r, \mathbf{A}_2)$ is a finite difference approximation to $r^{-1}\partial(r\mathbf{A}_2\mathbf{u}^R_{mn})/\partial r$. The column vector $\mathbf{u}^R_{mn}$ in equation (5.15) contains an entry for each of the five conservation variables at each radial discretization point.

Equation (5.15) can be solved [MV97] using a standard linear algebra routine, to determine the axial eigenvalues, χ_{mn}, and the right eigenvectors, $\mathbf{u}^R_{mn}(r)$, of the modal far-field unsteady perturbations. The left eigenvectors are determined by solving the equation $(\mathbf{P} - \chi_{mn}\mathbf{C})^H\mathbf{u}^L_{mn} = \mathbf{0}$, where the superscript H denotes the conjugate transpose. An orthonormal set of left eigenvectors is obtained by setting $(\mathbf{v}^L_{mn})^H = (\mathbf{u}^L_{mn})^H\mathbf{C}/[(\mathbf{u}^L_{mn})^H\mathbf{C}\mathbf{u}^R_{mn}]$. By invoking the orthogonality of left and right eigenvectors, the complex amplitudes of the modal disturbances, a_{mn}, are determined by taking inner products involving $\mathbf{v}^L_{mn}$ and $\mathbf{u}_W$, i.e.,

$$a_{mn} = \langle \mathbf{v}^L_{mn}, \frac{N_B}{2\pi}\int_{\theta}^{\theta+2\pi/N_B} \mathbf{u}_W \exp[-(\chi_{mn}\xi + i\bar{m}\theta)]d\theta\rangle\ . \tag{5.16}$$

5.2 Classification of Unsteady Disturbances

Unsteady perturbations of uniform mean flows can be represented as superpositions of convected entropic and vortical disturbances and upstream- and downstream traveling irrotational pressure disturbances. For nonuniform mean flows, the situation is more complicated [Kou95]. In particular, for rotational, but isentropic, mean flows, the unsteady entropy is an independent convected disturbance. However, because of the coupling between vortical and acoustic disturbances, due to mean-flow vorticity, neither convected vortical nor irrotational acoustic disturbances exist. Instead, nearly-convected or vorticity-dominated modal disturbances, that contain pressure, and acoustic or pressure-dominated disturbances, that contain vorticity, occur [GA96]. These types of disturbances emerge as solutions of the eigenvalue problem (5.14).

The group velocity,

$$V_{g,mn} = \partial\omega/\partial\chi_{mn} = \langle \mathbf{v}^L_{mn}, \mathbf{C}\mathbf{u}^R_{mn}\rangle / \langle \mathbf{v}^L_{mn}, (\partial\mathbf{P}/\partial\omega)\, \mathbf{u}^R_{mn}\rangle\ , \tag{5.17}$$

i.e., the axial velocity at which an mnth modal disturbance carries energy, is used to classify modal disturbances. Nearly-convected disturbances travel downstream, without attenuation, at axial speeds slightly less than and slightly greater than the mean flow speed. If the mean axial Mach number is subsonic, acoustic disturbances travel both upstream and downstream.

For nonuniform mean flows, we can further decompose the unsteady state vector to account for the two types of modal disturbances. Thus, we set $\mathbf{u}_W = \mathbf{u}_A + \mathbf{u}_N$, where $\mathbf{u}_A$ and $\mathbf{u}_N$ are the complex amplitudes the acoustic and the nearly-convected unsteady disturbances, respectively. The state vector for the acoustic disturbances has the form

$$\mathbf{u}_A(r,\theta,\xi) = \sum_{m=-\infty}^{\infty} \exp(i\bar{m}\theta) \sum_{\mu=0}^{\infty} \left[a^-_{m\mu,A} \mathbf{u}^{R,-}_{m\mu,A}(r) \exp(\chi^-_{m\mu,A}\xi) + a^+_{m\mu,A} \mathbf{u}^{R,+}_{m\mu,A} \exp(\chi^+_{m\mu,A}) \right] , \tag{5.18}$$

where μ indicates the number of radial nodes, and the $-$ and $+$ superscripts refer to downstream and upstream traveling disturbances. The nearly-convected disturbances, i.e.,

$$\mathbf{u}_N(r,\theta,\xi) = \sum_{m=-\infty}^{\infty} \exp(i\bar{m}\theta) \sum_{\mu=1}^{\infty} \left[a^-_{m\mu,N} \mathbf{u}^{R,-}_{m\mu,N}(r) \exp(i\kappa^-_{\xi,m\mu,N}\xi) + a^+_{m\mu,N} \mathbf{u}^{R,+}_{m\mu,A} \exp(i\kappa^+_{\xi,m\mu,N}\xi) \right] . \tag{5.19}$$

are also ordered by the number of radial nodes, but in this case starting with $\mu = 1$, and the $-$ and $+$ superscripts in (5.19) refer to disturbances that travel downstream at speeds slightly slower and slightly faster than the convection speed.

In numerical calculations, the series in equations, (5.18) and (5.19) must be truncated, since only finite number of circumferential and radial modes can be accommodated. Also, the numerical solutions to (5.15) will yield spurious modes; i.e., modes that satisfy the difference equation (5.15) but not the differential equation (5.14). The spurious modes must be eliminated or filtered out, to yield a valid solution set. The filtering is based on the number of radial zero crossings or nodes and the point-to-point oscillations of a computed radial mode. Such criteria have been usually found to yield only genuine modes, but the filtering algorithm is still under development. As another caveat, since only a finite number of modes are retained after the truncation and filtering processes, the numerical far-field modal description may be incomplete. Based on previous work [MV97], the inclusion of spurious modes, or the exclusion of genuine modes, can be detrimental to both the accuracy and convergence of numerical solutions.

5.3 Near-Field/Far-Field Matching Procedure

The far field solutions must be applied in conjunction with a numerical near-field solution to determine the unsteady flow. Incoming disturbances (excitations) are prescribed, and outgoing disturbances are determined by matching the near- and far-field solutions. The amplitudes of the outgoing modal disturbances are determined by taking inner products, cf. (5.16), using the near-field state vector, $\mathbf{u}$, in lieu of $\mathbf{u}_W$. This requires invoking the assumption that $\langle \mathbf{v}^L_{mn}, \mathbf{u} \rangle \approx \langle \mathbf{v}^L_{m,n}, \mathbf{u}_W \rangle$, i.e., that the left eigenmodes of the modal disturbances are orthogonal to the convected disturbances. Once the amplitudes of the outgoing modes are determined, the wave-type modes are superposed to provide a solution for $\mathbf{u}_W = \mathbf{u}_A + \mathbf{u}_N$ for a finite number of modes.

At the upstream far-field boundary, the convected disturbance is set to describe any incident convected gust. At the downstream boundary, the wave-type modes are subtracted from the total unsteady disturbance and the remainder, $\mathbf{u}_C = \mathbf{u} - \mathbf{u}_W$, is treated as a convected disturbance. The convected disturbance in the region $\xi > \xi_+$ is computed, by the method of characteristics, as a solution of $\bar{D}\mathbf{u}_C/Dt = 0$. Since the mean radial velocity has been assumed to be negligible, $\mathbf{u}_C(r,\theta,\xi) = \mathbf{u}_C(r,\theta,\xi_+)\exp[-i\omega(\xi-\xi_+)/V_\xi]$ along constant-radius characteristics.

In the near-field, the nonlinear unsteady equations are solved using the time-marching technique described in §4. After a pre-determined number of time steps, say N_T, of the near-field solution, the amplitudes of the wave-type modes, i.e., $a^{\mp}_{m\mu,A}$ and $a^{\mp}_{m\mu,N}$, and the complex amplitude of the far-downstream convected disturbance, $\mathbf{u}_C(r,\theta,\xi_+)$, are updated. The far-field solutions, which are the sums of wave-type and convected disturbances, are then updated, and used to supply the far-field boundary information needed for the next set of N_T near-field time-steps.

6. Numerical Results

Unsteady aerodynamic response predictions will be presented to demonstrate the current capabilities of the TURBO code. First, we will consider subsonic unsteady flows through a rotor, based on the Tenth Standard Cascade Configuration [FV93], which is referred to in [MV97] as the 3D 10th Standard Cascade. Second, we will analyze the NASA Rotor 67 [SWHS89], which is a research transonic fan consisting of 22 blades.

We consider unsteady flows that are excited by prescribed single-degree-of-freedom, harmonic, blade motions (e.g., see Figure 2). The motions to be considered are pure translations normal to the sectional blade chords ($\mathbf{R}_\mathrm{B} = h\mathbf{n}$), and pure rotations about axes at the blade midchords ($\mathbf{R}_\mathrm{B}(\bar{\mathbf{x}}_\mathrm{B}) = \boldsymbol{\alpha} \times (\bar{\mathbf{x}}_\mathrm{B} - \bar{\mathbf{x}}_\mathrm{P})$). The complex amplitudes, h and α, of the bending and torsional vibrations are assumed to be constant along the span; $\mathbf{n}(r) = n_\theta \mathbf{e}_\theta + n_\xi \mathbf{e}_\xi$ is the unit normal to the blade chord at radius r, which is tangent to the cylinder $r =$ constant; and $\bar{\mathbf{x}}_\mathrm{B} - \bar{\mathbf{x}}_\mathrm{P}$ is the distance, at constant radius, to the point, $\bar{\mathbf{x}}_\mathrm{B}(r)$, on the mean or reference blade surface from the point, $\bar{\mathbf{x}}_\mathrm{P}(r)$, at the mean position of the torsional axis.

The blade motions are termed subresonant if all fundamental acoustic response disturbances attenuate with increasing axial distance from the blade row; superresonant (m, μ) if m and μ such disturbances persist in the far upstream and far downstream flow regions, respectively, and carry energy away from the blade row; and resonant if at least one acoustic response disturbance persists in either the far upstream or far downstream regions of the flow and carries energy along the blade row [Ver89b].

The TURBO analysis has been applied to predict unsteady surface pressure and the local (w_C) and global (W_C) work per cycle responses to the prescribed blade vibrations. The local and global works per cycle are determined from the relations

$$w_C(\mathbf{x}_B) = -\omega^{-1} \int_{\phi}^{\phi+2\pi} P_B \frac{\partial \mathcal{R}_\mathrm{B}}{\partial t} \cdot \mathbf{n}_B d(\omega t) \quad \text{and} \quad W_C = \oint_B w_C(\mathbf{x}_B) dA_B \,. \tag{6.1}$$

In equation (6.1), P_B is the pressure acting at the point $\mathbf{x}_B$ on the moving reference blade surface $\mathcal{B}$, $\mathcal{R}_\mathrm{B}$ is the displacement of this point relative to its mean position in the rotating frame, $\mathbf{n}_B$ is a unit vector normal to $\mathcal{B}$ and pointing into the fluid, and dA_B is a differential element of surface area.

In addition to the nonlinear TURBO results, for purposes of comparison, we will also present response predictions for the 3D 10th Standard cascade based on the two-dimensional linearized analysis, LINFLO [Ver93] and three-dimensional linearized analysis, LINFLUX [MV97]. In LINFLO, the unsteady flow is regarded as a small perturbation of a nonuniform, potential, steady background flow. The full-potential analysis CASPOF [Cas83] has been used to provide the steady background flows for the LINFLO calculations. In LINFLUX, the unsteady flow is regarded as a small perturbation of a nonuniform, Euler, steady background flow. The TURBO analysis has been used to provide the steady background flows for the LINFLUX calculations.

The TURBO nonlinear steady-state solutions are determined, over a single extended blade passage, on an H-type grid. Because of our assumptions regarding the flows far from the blade row, the axial extent of the mesh must be chosen such that the mean flows at inlet and exit are at most small perturbations from steady background flows that are fully-developed and axisymmetric. We have retained first-order steady quantities in our far-field expansions of the meanflow quantities to accommodate small axial and circumferential variations in the steady flow. This allows some flexibility in restricting the axial extent of the near-field computational domain. For the numerical examples presented in this report, we have found that an extent of one axial chord both upstream and downstream of the blade row to be conservatively sufficient.

Since the TURBO code is written in terms of absolute-frame variables, the steady-state solutions for both numerical examples are obtained by marching the calculations in a time-accurate manner. These steady-state solutions are then used as inputs for both the unsteady TURBO computations as well as the linearized LINFLUX computations. The unsteady TURBO solutions are computed over single or multiple blade passages, depending on the interblade phase angle. The H-grids used for the present TURBO and LINFLUX calculations have been generated using either the IGB [BH92] or the TIGER [SS91] grid generation packages.

For the 3D 10th Standard Cascade, the steady background flow at inlet is axial and uniform relative to a space-fixed or inertial reference frame. Thus, the absolute inlet Mach number, $M^{\text{abs}}_{-\infty} = M^{\text{abs}}_{\xi,-\infty}$ is a constant. For the Rotor 67 fan, the relative inlet Mach number is supersonic near the tip and subsonic near the hub. Thus, the steady background flow at inlet is only approximately axial and uniform relative to a spaced-fixed reference frame.

6.1 3D 10th Standard Configuration

The 3D Tenth Standard Cascade consists of 24 blades, which are twisted to reduce the variation in mean incidence due to blade rotation. The blades rotate within a cylindrical annular duct of inner radius $r_H = 3.395$ and outer radius $r_D = 4.244$. At midspan ($r = r_{\text{mid}}$), the blades are staggered at $\Theta(r_{\text{mid}}) = 45\,\text{deg}$ with a circumferential spacing, $G(r_{\text{mid}}) = 2\pi r_{\text{mid}}/N_{\text{B}}$, of unity, and the midspan blade section is a NACA 5506 airfoil, altered slightly [Ver89a] to have wedge-shaped trailing edges. The blade mean chord lines are located at

$$r\theta = \xi \tan\Theta + nG(r),\ 0 \le \xi \le \cos\Theta,\ n = 0, \dots, N_{\text{B}} - 1\ , \tag{6.2}$$

where

$$\frac{\tan\Theta(r)}{\tan\Theta(r_{\text{mid}})} = \frac{r}{r_{\text{mid}}}\ . \tag{6.3}$$

The axial chord is constant, hence, the leading and trailing edge ξ and θ coordinates are constant along the entire span. The airfoil chord varies from 0.946 at the hub to 1.057 at the tip, because of twist, and the local thickness to chord ratio varies to maintain constant thickness. The cascade operates in a uniform axial inlet flow, which occurs at $M^{\text{abs}}_{-\infty} = 0.4015$, and rotates at an angular speed of $|\Omega| = 0.2145$. This 3D configuration was chosen to match the subsonic Tenth Standard Configuration [FV93] at midspan, where the relative inlet Mach number, $M_{-\infty}$, is 0.7 and the relative inlet flow angle, $\Omega_{-\infty}$, is 55 deg.

The H-grid for the 3D Tenth Standard Cascade consists of 141 axial, 41 tangential and 11 radial surfaces (56,000 cells), and extends one axial chord upstream and downstream from the blade row. This is identical to the grid used in the 3D LINFLUX studies of [MV97]. Axial grid points are clustered near blade leading and trailing edges; circumferential grid points, near blade surfaces; and radial points are distributed uniformly. In particular, the normal and chordwise grid spacings at a blade leading edge are 0.02% and 0.10% of chord, respectively, see Figure 3.

The axial extent of the grid was found to be sufficient for the mean flow field to reach axisymmetric steady states at the computational inflow and outflow boundaries. There are 81 axial points on the upper and lower blade surfaces, and 30 axial points on the upstream and downstream periodic boundaries. This distribution was found to be sufficient for most of the calculations reported herein, with approximately 20 points per wave being applied to resolve the dominant acoustic waves. However, for some of the 3D Tenth Standard Cascade calculations, the near-sonic conditions on blade suction surfaces resulted in short wavelength acoustic response phenomena that could not be resolved on the prescribed 141 × 41 × 11 H-mesh.

The TURBO near-field, finite-volume solutions have been coupled to far-field acoustic eigensolutions, which have been determined on a radial grid consisting of 24 points clustered near the hub and duct walls. For the present calculations, any nearly convected disturbances that occur downstream of the blade row are simply convected numerically through the computational outflow boundary and into the far downstream region of the flow.

The full potential steady and the LINFLO linearized unsteady solutions were determined on composite meshes consisting of local C-meshes embedded in global H-meshes, which extended one axial chord upstream and downstream from the blade row. The H- and C-meshes used with LINFLO consisted of 155 axial and 41 tangential lines and 101 radial and 21 circumferential lines, respectively. Coarser H- and C- meshes were used for the CASPOF calculations.

The numerical solutions, reported herein, were determined on an IBM-3CT Workstation. TURBO, "time-accurate," steady, subsonic, inviscid solutions required 780 CPU minutes per 1,000 time steps and a minimum of 1,500 to 2,000 time steps to converge. The TURBO unsteady calculations were started from the steady solution, and performed using 500 time-steps per cycle of blade motion and four Newton iterations per time step. For single-passage solutions, six to eight cycles of motion were needed to converge the nonlinear inviscid solutions to a periodic state. The subsonic inviscid calculations required 350 CPU minutes per blade passage per cycle of blade motion. The number of blade passages included in a nonlinear unsteady calculation depends upon the interblade phase angle. For example, if $\sigma = 60$ deg, six passages are needed.

TURBO nonlinear steady and unsteady calculations require approximately 1350 μsec./time-step/cell with four sub-iterations. The memory requirement, using 32-bit arithmetic, is approximately 1.8 kilobytes/cell. This requirement is based on the option of using two blocks per blade passage and in-core storage for all variables.

Steady Flow

Predicted distributions of relative, steady, isentropic, surface, Mach number based on local static pressure $[P(r,\theta,\xi)]$ and the local inlet relative total pressure $[P_{T,-\infty}(r)]$, i.e.,

$$M = \left\{ \frac{2}{\gamma - 1} \left[\left(\frac{P_{T,-\infty}}{P} \right)^{\frac{\gamma-1}{\gamma}} - 1 \right] \right\}^{\frac{1}{2}} , \qquad (6.4)$$

for the 3D and 2D, 10th Standard Cascades, are shown in Figure 4. The inlet and exit, mean-flow quantities for the 3D calculation are given in Figure 5. For the CASPOF, full potential calculation, the relative inlet Mach number, $M_{-\infty} = 0.7$, and inlet flow angle, $\Omega_{-\infty} = 55$ deg, are prescribed and a Kutta condition is imposed at the blade trailing edges. For the TURBO calculation, the total temperature ($T_T^{\text{abs}} = 5.766$) and total pressure ($P_T^{\text{abs}} = 2.237$) of the uniform mean inlet flow ($V_\theta^{\text{abs}}) = 0$ are specified at the computational inlet boundary (i.e., at $\xi = \xi_{-\infty} = -c_{\text{ax}}$), and the mean-flow static pressure at the hub is specified at the computational exit boundary ($\xi = 2c_{\text{ax}}$), so that the relative inlet flow at midspan matches the 2D conditions.

The TURBO steady-flow predictions at the hub, $r/r_{\text{D}} = 0.8$, midspan, $r/r_{\text{D}} = 0.9$, and tip, $r/r_{\text{D}} = 1.0$, given in Figure 4, indicate that the Mach numbers on the blade suction and pressure surfaces show moderate variations with radius. Also, the 3D TURBO predictions at midspan are in close agreement with the 2D CASPOF predictions. The TURBO results indicate that the maximum Mach numbers on the suction surface of a blade are 0.849 at the hub, 0.906 at midspan, and 0.961 at the tip. These values occur at $\xi/c_{\text{ax}} = 0.053$, 0.073 and 0.085, respectively. Thus, the flow is very close to sonic in the tip region, along a blade suction surface just aft of the leading edge. The CASPOF predictions for the 2D cascade indicate a maximum Mach number of 0.916 at $\xi = 0.065$.

For the three-dimensional flow, the steady static pressure ($P = 1.4577$), density ($\bar{\rho} = 1.0$), and axial velocity ($V_\xi = 0.5736$) have constant values at inlet and the relative circumferential velocity, $V_\theta = -\Omega r$ varies linearly from 0.7283 at the hub to 0.9103 at the tip. At the computational exit boundary, the steady pressure, density, and axial velocity vary with radius (mean shear), and the circumferential velocity varies nonlinearly with radius (mean swirl). As indicated in Figure 5, the steady blade loading causes increases in the pressure and density and decreases in the axial and circumferential velocities, especially the latter.

Blade Vibration

The 3D TURBO and LINFLUX analyses and the 2D LINFLO analysis have been applied to predict the unsteady aerodynamic responses of the 3D and 2D 10th Standard Cascades to pure bending and pure torsional blade vibrations at unit frequency, as described below. In a linearized analysis, such as LINFLUX or LINFLO, the far-field conditions are determined based on the input mean flow before the unsteady computation begins. In the nonlinear TURBO analysis, a converged solution, which is steady in the rotating frame of reference, is used as the initial solution for an unsteady computation. Temporal Fourier decompositions of the flow quantities at inlet and exit are performed as the solution is marched in time. The temporal Fourier coefficients are updated N times per cycle, where N is a user input.

All of the results presented in this report have been determined using five updates per cycle. Thus, the far-field conditions are determined based on the most current temporal Fourier coefficients. Ideally, the zero-frequency, temporal Fourier coefficients should correspond to the initial mean flow. However, the back pressures used for all the unsteady TURBO calculations are the same as the back pressure used in the mean-flow calculation. As a result, the mean mass flow for different unsteady cases can differ by as much as 1% of the steady mass flow. One could maintain the same mean mass flow by adjusting the back pressure for each unsteady run, but this would be laborious and computationally expensive.

In the current 3D TURBO analysis, two to three temporal harmonics are kept in the far-field analysis. These higher harmonic terms, as will be shown later, are usually small compared to the first harmonic term. Thus, the classification of sub- or superresonant unsteady motion is based on the propagation properties of the fundamental (i.e., first-harmonic) acoustic disturbances. For example, the unsteady excitation at $\omega = 1$ and $\sigma = 90$ deg is classified as superresonant, because propagating acoustic response disturbances at the excitation frequency exist in the upstream region. If this excitation is a prescribed blade vibration, only acoustic response disturbances will occur in the far-field.

Local (w_C) and global (W_C) work-per-cycle predictions for the 3D 10th Standard Cascade undergoing pure torsional and pure bending vibrations at $\omega = 1$ and $\sigma = \pm 90$ deg ($N_D = \pm 6$) are shown in Figure 6, where the TURBO local response predictions are given at eleven spanwise stations from hub ($r/r_D = 0.8$) to tip ($r/r_D = 1.0$). These results indicate that the local work per cycle responses to the blade torsional and bending blade vibrations do not vary significantly with radius, but, the results for the bending vibrations show greater radial variations than those for the torsional motions. Note that the multi-passage TURBO solutions show slight blade-to-blade variations. Hence, local work-per-cycle predictions shown in Figure 6 are those on the reference blade; and the global work-per-cycle predictions are the averaged values, taken over all blades operating within the numerical solution domain. We will discuss the blade-to-blade variation later in this section.

The averaged local work per cycle predictions at midspan, as determined from the 3D TURBO, LINFLUX and the 2D LINFLO predictions, for the 10th Standard Cascade vibrating in torsion and bending are shown in Figures 7 and 9, respectively, for blade motions at unit frequency and at interblade phase angles, σ, of -90 deg, 0 deg, $+90$ deg and $+180$ deg. The motions at $\sigma = 0$ deg and 90 deg are superresonant. For the in-phase motions at $\sigma = 0$ deg, propagating acoustic response disturbances, at $(m, \mu) = (0, 0)$, occur both upstream and downstream of the blade row. For the motions at $\sigma = 90$ deg, such a disturbance occurs only in the upstream region. For the (subresonant) motions at -90 deg and $\sigma = 180$ deg all acoustic response disturbances attenuate.

Figure 7 shows that the torsional response predictions determined using the TURBO code are in good agreement with the corresponding 3D LINFLUX and 2D LINFLO predictions. The TURBO calculations were run with radial-mode far-field boundary conditions. To demonstrate the need for such conditions, the same torsional vibration cases were run, with TURBO, using quasi-unsteady, local, one-dimensional, far-field boundary conditions [Jan89]. Figure 8 shows that the predictions based on the 1D far-field conditions do not agree very well with the 2D LINFLO results, except for the subresonant vibration at $\sigma = -90$ deg. When the blades undergo a subresonant motion, all acoustic response disturbances attenuate. Thus, 1D boundary conditions are often adequate. However, for the vibration at $\sigma = 180$ deg, which is also subresonant, the local work per cycle predictions show appreciable differences on the suction surface. Similar discrepancies are also noted for the $\sigma = 0$ deg case. Although the unsteady motion at $\sigma = 0$ deg is superresonant, 1D boundary conditions should be capable of handling the planar propagating waves. Of the four cases shown in Figure 8, the unsteady predictions for the superresonant vibration at $\sigma = 90$ deg clearly show the poorest agreement.

Predictions for bending vibrations, as determined using the three aforementioned codes, are shown in Figure 9. Those for the bending vibrations at $\sigma = 0$ and 180 deg show small differences over the entire blade. The reasons for these differences are not understood at present, but similar discrepancies have been reported in earlier work in which the predictions of 2D nonlinear [AV94, AV96], 2D linearized (LINFLUX) [VMK95, MV95], and 3D linearized (LINFLUX) [MV97] analyses were compared with LINFLO results. Similar to the results of the 3D LINFLUX analysis, the local work per cycle predictions for the bending vibration at $\sigma = 90\,\text{deg}$ show small differences along the pressure surface, but large differences on the suction surface. The reasons for the large discrepancies have not been established at this time. However, we suspect that local, high-wave-number, acoustic responses, occurring in regions of high-subsonic steady Mach number, are not adequately resolved on the $141 \times 41 \times 11$ H-mesh used for the TURBO calculations. The local work per cycle predictions for the bending vibration at $\sigma = -90\,\text{deg}$ also show important differences, in this case, on both the suction and pressure surfaces. This is the only TURBO run that is significantly different from the 3D LINFLUX results given in [MV97]. Again, it is not understood why the discrepancies occur.

Global work-per-cycle predictions for the 2D and 3D 10th Standard Cascade cascades undergoing prescribed blade vibrations are shown in Figure 10, where results for the global work per cycle versus interblade phase angle are given for pure torsional vibrations about midchord and pure bending vibrations at unit frequency. The 3D TURBO results, indicated by the circular symbols in Figure 10, have been determined for $N_D = -6, -4, 0, 4, 6, 8, 16$, and 18; the 3D LINFLUX results, by the square symbols, for $N_D = -6, -5, \ldots, 18$, and the 2D LINFLO results, for $-90\,\text{deg} \leq \sigma \leq 270\,\text{deg}$ in increments of one degree. The 2D work per cycle predictions are multiplied by the blade span, i.e., $r_D - r_H = 0.2\, r_D = 0.849$, to allow a convenient comparison with the 3D predictions.

The resonance or cut-off conditions for the two-dimensional configuration are $\sigma^-_{-\infty} = -26.93\,\text{deg}$ and $\sigma^+_{-\infty} = 117.12\,\text{deg}$ in the far upstream region and $\sigma^-_{+\infty} = -31.80\,\text{deg}$ and $\sigma^+_{+\infty} = 59.79\,\text{deg}$ in the far downstream region. The superresonant blade motions at $\omega = 1$ occur at interblade phase angles between these cut-off values and send a propagating wave into the upstream and/or downstream regions of the flow. The blade motions at $-90\,\text{deg} \leq \sigma < -31.80\,\text{deg}$ and $117.12\,\text{deg} < \sigma \leq 270\,\text{deg}$ are subresonant. The results in Figure 10 indicate a very good agreement between the 3D TURBO, the 3D LINFLUX and the 2D LINFLO global response predictions over the entire nodal diameter or interblade phase angle range of blade vibrations. We should reiterate, however, that for superresonant bending vibrations at $\sigma = 90$ deg, and the subresonant bending motions at $\sigma = -90$ deg, the TURBO and LINFLO local responses show large differences, cf. Figure 9.

Next, we consider the acoustic properties far from the blade row. Predicted steady, as well as first- and second-harmonic axial eigenvalues and first-harmonic radial pressure modes, $p^R_{m\mu}(r)$, for $m = -1, 0, 1$ and $\mu = 0, 1$ are shown in Figures 11 through 13. Here, the unsteady excitation occurs at $\omega = 1$ and $N_D = 6$ ($\sigma = 90\,\text{deg}$). Because of mean blade loading, the steady inlet and exit conditions for the 3D 10th Standard Cascade differ. As a result, the acoustic properties, $\chi_{m\mu}$ and $p^R_{m\mu}$, in the far-upstream region of the flow, differ from those in the far-downstream region. In particular, for an unsteady excitation at $\omega = 1$ and $\sigma = 90\,\text{deg}$, the fundamental acoustic disturbances in the (0,0) mode are of propagating type far upstream, but, of attenuating type far downstream. Note that the second-harmonic acoustic disturbances in the (0,0) mode are of propagating type in both the upstream and downstream regions.

In the far-upstream region of an unsteady flow at $\omega = 1$ and $\sigma = 90$ deg through the 3D 10th Standard Cascade , the propagating acoustic response disturbance has an axial wave number, κ_ξ, of 1.584 and the least damped or (0,1) response disturbance has an attenuation constant, β, of 3.964. In the far-downstream region, $\beta = -1.077$ for the least-damped or (0,0) response disturbance. These numbers agree favorably with those predicted by the 3D LINFLUX run, namely, 1.583, 3.990, and -1.084. Since the absolute far-downstream mean flow is nonuniform, the axial wave numbers of the attenuating disturbances in a given circumferential mode vary with radial mode number, μ, as indicated in Figure 12, particularly those for $m = 1$.

The radial eigenmodes for the pressures associated with the far upstream acoustic excitations or responses and the far downstream acoustic responses for an unsteady excitation at $\omega = 1$ and $\sigma = 90$ deg are shown in Figure 13. Although the inlet and exit mean-flow conditions differ, the upstream and downstream radial pressure modes are very similar, with the downstream modes showing a somewhat greater radial variations than their upstream counterparts. Note that the phase of a modal pressure disturbance is independent of radius for the uniform absolute mean flow at inlet, but the phase varies with radius for the mean flow with swirl and axial shear that exists in the far downstream region. Thus, the far-upstream, pressure modes, $p^R(r)$, are purely real, but the far-downstream modes have some imaginary or out-of phase content.

The TURBO calculations for the subresonant $\sigma = -90$ deg and the superresonant $\sigma = 90$ deg blade motions reveal that, for the most part, the far-field acoustic responses are of small amplitude at the computational inflow and outflow boundaries. However, the superresonant torsional and bending vibrations at $\sigma = 90$ deg produce upstream propagating acoustic response disturbances which have amplitudes, a_A, of 1.352 and 1.540, respectively, and occur at an axial wave number, κ_ξ, of 1.583. The corresponding LINFLO predictions are $a_A = 1.529$ and 2.822 and $\kappa_\xi = 1.603$. Thus, there is a substantial difference between the TURBO and LINFLO predictions for the upstream propagating, (0,0), acoustic response waves caused by the bending vibration.

In Table 6.1, the TURBO-predicted eigenvalues and amplitudes of the upstream propagating, (0,0), acoustic response wave caused by the bending and torsion vibrations are compared against the corresponding LINFLUX and LINFLO values. Note that TURBO updates the far-field eigenmodes several times per cycle. Certain eigenmodes, usually higher order ones, may be missing from one update but reappear in the next update because the current eigenmode filtering scheme sometimes filters out modes that should be retained. In Table 6.1 the eigenvalue for the bending vibration is slightly different from the one for the torsional vibration, because the meanflow evolves differently in the two unsteady computations. Also, the eigenvalues and amplitudes for the (0,0) acoustic response mode of the second temporal harmonic are listed in the table. The second-harmonic content is significant in the initial cycle, but becomes negligible after eight cycles.

Next, we examine the results for a bending vibration at $\omega = 1$ and $\sigma = -90$ deg in some detail. This case is chosen because the nonlinear response predictions are in poor agreement with the results of both 2D and 3D linearized analyses. In addition, the response predictions show the most blade-to-blade variation. Furthermore, this is the only case that we were not able to get a converged work-per-cycle prediction even after more than forty cycles of unsteady computations.

	κ_ξ		a_A	
	torsion	bending	torsion	bending
LINFLO	1.603		1.529	2.822
LINFLUX	1.583		1.352	1.540
TURBO (1st harmonic, 8th cycle)	1.587	1.584	1.375	1.610
TURBO (2nd harmonic, 1st cycle)	3.216	3.218	0.103	0.103
TURBO (2nd harmonic, 8th cycle)	3.223	3.219	5.99×10^{-3}	4.96×10^{-4}

Table 6.1: Comparison between the axial wave numbers (k_ξ) and acoustic disturbance amplitudes (a_A) predicted by the 2D linear analysis (LINFLO), the 3D linear analysis (LINFLUX), and 3D nonlinear analysis (TURBO).

In Figure 14, the calculated time histories of the mass flow, $\dot{m} = \int \rho \boldsymbol{V} \cdot d\boldsymbol{A}$, and total pressure ratio, $P_{T,+\infty}/P_{T,-\infty}$ for the first twenty cycles are shown. It can be observed that the mass flow reached a periodic state in approximately six cycles. The normalized mean mass flow of 8.125 is approximately 0.7% lower than the normalized steady mass flow of 8.18. The time history of the mass flow shows significant higher harmonic content, even after the mass flow reaches a periodic state. We have not been able to determine the cause of the high non-harmonic variation in mass flow that occurs during the initial cycles. The inlet/exit mass flow fluctuation is observed immediately after the start of the unsteady computation, thus, this fluctuation must be generated in the far field, not in the interior of the solution domain due to the blade motion. One possible source of numerical error might be a deforming grid formulation, in which the "geometric conservation law" is violated. However, to the best of our knowledge, the TURBO deforming grid formulation and implementation are correct and do not violate the geometric conservation law. Moreover, a similar implementation was successfully used in the 2D nonlinear NPHASE analysis [AV94, AV96].

In the current TURBO unsteady analysis, we have included two to three temporal harmonic terms in the far-field analysis to minimize the reflection of outgoing transient higher harmonic waves back into the solution domain. Unfortunately, in addition to the aforementioned non-harmonic terms appearing in the far-field, the initial impulsive blade motion appears to have generated anharmonic and higher harmonic waves. Some of these waves are reflected, and the reflections ultimately result in blade-to-blade variations in the work-per-cycle response. This effect seems to be most noticeable for cases in which blades undergo bending vibrations.

Detailed response results for the 3D 10th Standard Cascade undergoing a bending vibration at $\omega = 1$ and $\sigma = -90\,\text{deg}$ are shown in Figures 15–17. An examination of the time-mean static pressure shows that the time-mean loadings on all four blades are the same. The real and imaginary parts of the first-harmonic unsteady pressure at mid-span are shown in Figure 15. The unsteady pressures on the neighboring blades do appear to be 90 deg out of phase. For example, the in-phase unsteady pressure on blade 0 (solid line) is similar to the out-of-phase unsteady pressure on blade 1 (long dashes). However, the local work-per-cycle predictions in Figure 16 show noticeable variations from blade to blade. The midpsan, local work-per-cycle predictions on all the four blades are shown in Figure 17. For comparison with the results of the 2D linearized analysis, we have averaged the TURBO, midspan, local work-per-cycle predictions over all blades, cf. Figures 7 and 9.

6.2 NASA Rotor 67

The NASA Rotor 67 is a research transonic fan consisting of 22 blades. The tip diameter of the fan rotor varies from 51.4 cm at the leading edge to 48.5 cm at the trailing edge, and the hub-to-tip radius ratio varies from 0.375 to 0.478 from the inlet to exit. At the design point, the rotational speed of the rotor is at 16,043 rpm. With an inlet axial Mach number of approximately 0.49, the tip speed at the design condition is 429 m/sec, which corresponds to a tip relative Mach number of 1.38. Also, the mass flow rate at the design point is 33.25 kg/sec and the total pressure ratio is 1.63.

The purpose of the present numerical study is to demonstrate the capabilities of the TURBO analysis for analyzing the flutter characteristics of realistic transonic fans. Our goal is to obtain steady inviscid solutions at two throttle positions on the design speed line, one near peak efficiency and the other near stall. At each point, we will perform flutter analyses for a bending and a torsional vibration at two different nodal diameters.

The grid for the Rotor 67 calculations, see Figure 18, consists of 121 axial, 33 tangential and 17 radial surfaces (61,440 cells), and extends one axial chord, at mid-span, upstream and downstream from the blade row. For the calculations, we assume that there is no clearance between the rotor blades and the outer duct wall. We have also idealized the endwalls such that near the computational inlet and exit boundaries, the inner and outer duct radii are constant. This is necessary because the 3D far-field eigensolver assumes that the inlet and exit flows are fully developed and, therefore, that they do not vary with axial distance. The computational grid consists of 65 axial points on the upper and lower blade surfaces, and 28 axial points on the upstream and downstream periodic boundaries. The grid is clustered near blade leading and trailing edges, and near blade surfaces. The current version of the TIGER grid generation package [SS91] used for generating the Rotor 67 grid, does not have an elliptic grid smoother. Thus, the grid quality near the leading- and trailing-edge planes is relatively poor. Furthermore, we have not examined whether the selected grid has adequate resolution for the Rotor 67 flows being considered, especially in the axial direction. The size of the grid was chosen so that the present unsteady calculations could be performed on a 128MB workstation.

TURBO time-accurate steady subsonic inviscid solutions for the Rotor 67 study required 680 CPU minutes per 1,000 time steps on an IBM-3CT Workstation. It is unclear to us why this case with slightly more grid cells (61,440) than that of the 3D 10th Standard Cascade case (56,000) require less CPU time per 1,000 time steps. However, for the Rotor 67 analysis, the first converged steady-state solution took more than 8,000 time steps. The TURBO unsteady calculations were started from the appropriate steady solution, and performed using 500 time-steps per cycle of blade motion, four Newton iterations per time step. For each cycle of blade motion, the unsteady inviscid calculations required 375 CPU minutes per blade passage.

As for the calculations for the 3D 10th Standard Cascade, the TURBO near-field, finite-volume solutions are coupled to far-field acoustic eigensolutions, which are determined on a radial grid consisting of 24 points clustered near the hub and duct walls. Any nearly convected disturbances that occur downstream of the blade row are simply convected numerically through the computational outflow boundary.

Steady Flow

Numerous researchers; e.g., Chima [Chi91], Jennions, et al. [JT92], Arnone [Arn93], Rhie, et al. [RZH+93], have performed numerical simulations of viscous flows through the NASA Rotor 67. Most showed the flow field to be very complicated and characterized by effects such as shock-boundary layer interaction, tip-leakage flow, unsteady vortex shedding, and flow separation with vortex roll up. Under the present effort, we have performed inviscid simulations of steady and unsteady flows.

Initially, we experienced difficulties in getting converged steady-state inviscid solutions. Consequently, we had to use very small time steps for the first quarter of the rotor rotation before the time step or the CFL number could be increased. Also, because of the relatively coarse grid used for our calculations, we did not expect the resulting solutions to agree well with data. As a result, we did not run the whole speed line. Instead, we ran two different back pressures to steady state to approximate the peak efficiency and near stall points reported in [SWHS89]. The mass flow for the first point (near peak efficiency) is 34.8 kg/sec and the total pressure ratio is 1.67. The mass flow for the second point (near stall) is 31.0 kg/sec and the total pressure ratio is 1.75. As expected, the inviscid "speedline" is higher than the experimental speedline due to lower losses, see Figure 19. Surprisingly, the TURBO inviscid solutions show good qualitative agreement with the experimental data.

In Figures 20 and 21, the numerical and experimental relative Mach number contours at three different spanwise locations are shown for the two different operating conditions mentioned above. Note, the constant J surfaces on which the contours plots of the numerical solution are shown are not constant-radius surfaces. Also, the contour plots of the numerical solutions are plotted in the ξ,θ-plane instead of the $\xi,r\theta$-plane because the plotting package used in generating the contour curves could not properly handle periodic boundaries that have varying radial locations. This explains why the airfoil geometries in the contours plots for the experimental data are not the same as those in the contour plots for the numerical results.

The Mach number contours near the peak efficiency point are shown in Figure 20. Those at 10 percent of span from the tip show an inlet Mach number of 1.35. There is a bow shock at the leading edge, and a normal in-passage shock near the trailing edge on the suction surface. At 30 percent of span, the flow pattern is similar, except that the inlet Mach number is lower, i.e., approximately 1.2. At 70 percent of span, the inlet Mach number is 0.95 and a supersonic bubble appears on the suction surface near the leading edge.

In Figure 21, we consider the near stall condition. The Mach contours at 10 and 30 percent of span show that the location of the in-passage shock is near midchord on the suction surface, and the strength of the shock is much stronger than the normal shock that occurs at near peak efficiency. Thus, the exit Mach number is lower in the near stall case. At 70 percent span, the size of the supersonic bubble has increased significantly. In general, the qualitative agreement between experiment and the computations for both operating conditions is good. However, because of grid clustering near blade edges and near blade surfaces, the grid is relatively coarse in the mid-chord and mid-passage regions. Hence, the inviscid solutions show highly smeared shocks.

Figure 22 shows a carpet plot of the chordwise steady pressure distributions at 17 spanwise stations. Here, the axial distance is normalized by the axial chord length at the hub. Due to blade twist, the normalized axial locations of the leading and trailing edges at the blade tip are approximately 0.25 and 0.75, respectively. The curves in Figure 22 clearly depict the differences between in-passage shock locations for the two steady solutions. These curves have pressure spikes at the blade trailing edge that are due to flow overspeeds over blunt trailing edges.

The radial distributions of the inlet and exit mean-flow quantities for Rotor 67 operating near peak efficiency are shown in Figure 23. At inlet, the relative circumferential velocity, $V_\theta = -\Omega r$ varies linearly from 0.436 at the hub to 1.263 at the tip, and the steady static pressure (P), density $(\bar{\rho})$, and axial velocity (V_ξ) are nearly constant. At the computational exit boundary, the steady pressure, density, and axial velocity vary with radius (mean shear), and the circumferential velocity varies nonlinearly with radius (mean swirl). As indicated in Figure 23, the steady blade loading causes increases in the pressure and density and decreases in the circumferential velocity. There is only a slight decrease in the axial velocity because the steady-flow operating point is not too far from the choke point.

Blade Vibration

For the flutter analysis, we have arbitrarily chosen a blade vibratory frequency of 1.19 times the rotation speed, giving a reduced frequency of 0.54 (based on the midspan relative inlet velocity and blade chord), because we do not have any structural information for the blade. This frequency is probably representative of, or slightly higher than, the first bending mode frequency of a typical low aspect ratio fan. Presently, a torsional and bending mode of the same frequency have been studied in our flutter analysis of Rotor 67. As stated earlier, simple 2D analytical mode shapes have been used, because there is no readily available structural information for the Rotor 67 configuration. We should note that the TURBO code is capable of handling finite-element mode shapes, such as NASTRAN-generated modes.

The TURBO analysis was run for vibrations at two nodal diameters, $N_D = 0$ and $N_D = 11$, for each of the meanflow conditions discussed above. At the near peak efficiency point, the predicted mean-flow, first-harmonic, and second-harmonic axial eigenvalues, at the inlet and exit, are shown in Figures 24 and 25, respectively, for the acoustic modes at $m = -1, 0, 1,\ \mu = 0, 1, 2, 3, 4$ and an unsteady excitation at $\omega = 0.54$ and $N_D = 0$ $(\sigma = 0\,\text{deg})$. The first-harmonic radial pressure modes, $p^R_{m\mu}(r)$, are shown in Figure 26. As for the subsonic 3D 10th Standard Cascade, the steady inlet and exit conditions differ due to mean blade loading. Thus, the acoustic properties $\chi_{m\mu}$ and $p^R_{m\mu}$, in the far-upstream region of the flow differ from those in the far-downstream region. However, unlike the results for the subsonic 3D 10th Standard cascade, there are many propagating acoustic modes in the far-upstream region because the meanflow at inlet is supersonic in the blade-tip region.

In the far-upstream region of an unsteady flow, at $\omega = 0.54$ and $\sigma = 0\,\text{deg}$, through Rotor 67 operating near peak efficiency, the far-field eigenanalyses of both the first and second temporal harmonics show that the first three radial modes for $m = -1$, the first two modes for $m = 1$, and the (0,0) mode are all propagating. For the first temporal harmonic, the axial wave number, κ_ξ, for modes (-1,0), (0,0), and (1,0) are 111.8, 6.766, and -94.4, respectively. As a result, the computational grid used in the near-field calculation does not have the resolution needed to accurately resolve the (-1,0) and (1,0) modes. For the torsional vibration, The least-damped or (0,1) response disturbance has an attenuation constant, β, of 10.86. The (0,0) upstream propagating acoustic response disturbance has an amplitude, a_A, of 1.35 which is linearly scaled to correspond a blade pitching amplitude of one radian about the midchord locations. All the other modes are at least two orders of magnitude smaller than the (0,0) acoustic response disturbance. However, near stall, the amplitudes of the (-1,2) and (1,1) acoustic disturbances are approximately 20% and 10% of that of the (0,0) acoustic disturbance.

Far fewer modes are determined in the far-downstream region than in the far-upstream region. This is probably an artifact of the numerical filtering scheme currently used in the far-field eigenanalysis. For this particular case, the filtering scheme did not eliminate all the superfluous modes. For example, there is one superfluous mode for the first temporal harmonic. We do not know whether these nonphysical modes will degrade the solutions or not. Only the (0,0) acoustic response disturbances are propagating. For the torsional motion, the first-harmonic axial wave number of the (0,0) mode is 5.88, and the amplitude of the disturbance is 0.123. The least-damped or (0,1) response disturbance has an attenuation constant of -15.82, and a non-negligible amplitude of 0.058. For the second temporal harmonic, the axial wave number of the (0,0) mode is 11.73, and the amplitude of the disturbance is 0.103. Also, the attenuation constant of the (0,1) mode is -14.48, and the amplitude of this mode is 0.032.

The radial eigenmodes for the pressures associated with the far upstream acoustic excitations or responses and the far downstream acoustic responses for an unsteady excitation at $\omega = 0.54$ and $\sigma = 0$ deg are shown in Figure 26. In addition to the differences between the inlet and exit mean-flow fluid properties, the hub-to-tip ratios are different at inlet and exit. Yet, the lowest order upstream and downstream radial pressure modes are very similar.

Local (w_C) and global (W_C) work per cycle predictions for Rotor 67 undergoing pure torsional motions at $\omega = 0.54$, and $\sigma = 0$ and 180 deg ($N_D = 0$ and 11) at the two aforementioned meanflow conditions are shown in Figure 27. The TURBO analysis indicates that the blade motions are stable. Moreover, as indicated by the global work per cycle predictions, the blade motions at $N_D = 11$ are more stable than those at $N_D = 0$. Also, the results show the blade to be more stable when operating at the near stall point than at the near peak efficiency point. The last observation seems to contradict previous experience. A close examination of the local work per cycle distributions shows the unsteady forces around the in-passage shock play an important role in determining stability of the blade motion. Near the peak efficiency point, the location of the in-passage shock in the outer span region of the blade is near the trailing edge on the suction surface and near mid-chord on the pressure surface. At $N_D = 0$, the unsteady forces ahead of the shock on both the pressure and suction surfaces extract energy from the torsional blade motion. For an out-of-phase torsional motion, the unsteady forces on the pressure surface ahead of the shock are significantly more stabilizing than are those for the $N_D = 0$ case, whereas forces ahead of the shock on the suction surface are destabilizing. Near stall, the in-passage shock moves forward towards the leading edge on the pressure surface, and towards mid-chord on the suction surface. The unsteady forces on the pressure surface near the leading edge, where the shock sits, are extracting work from the blade; whereas the unsteady forces on the suction surface in the vicinity of the shock, are stabilizing for $N_D = 0$ and destabilizing for $N_D = 11$.

Local and global work per cycle predictions for Rotor 67 undergoing pure bending motions at $\omega = 0.54$, $\sigma = 0$ and 180 deg and for the two meanflow conditions being considered are shown in Figure 28. Once again, the TURBO predictions show the blade motion to be stable at the four points analyzed. As for the torsional vibrations, the blade motions are more stable at $N_D = 11$ than at $N_D = 0$. However, as the back pressure increases, the bending vibrations at $\sigma = 0$ deg become less stable. Again, as for the torsional vibrations, the unsteady forces near the shock dominate the work-per-cycle predictions for the peak efficiency point. At this meanflow condition, the unsteady forces on the pressure surface ahead of the shock are stabilizing, while the unsteady forces on the suction surface are destabilizing, if $N_D = 0$ and stabilizing, if $N_D = 11$. At the near stall meanflow condition, the contributions to the local work per cycle from the unsteady loads away from the shock are significant, especially for the bending vibration at $N_D = 0$, in which the unsteady forces over the latter half of the blade on the suction surface, contribute energy to the blade motion.

6.3 Discussion

We have presented numerical results for unsteady flows through a three-dimensional version of the 10th Standard Cascade. These results pertain to flows in which the unsteady fluctuations are caused by prescribed blade vibrations. They were determined using the 3D TURBO and LINFLUX analyses and the 2D LINFLO analysis. TURBO employs an implicit, flux-split, finite-volume scheme for solving the unsteady Euler equations in the near field, which typically extends from one axial chord upstream to one axial chord downstream of the blade row, and numerical eigenanalyses for determining unsteady perturbations of fully-developed, axisymmetric, swirling mean flows in the far upstream and far downstream regions. For the unsteady flows considered herein, the eigenanalyses have been used to determine the first two or three modal acoustic disturbances, additional higher-order disturbances are assumed to be of negligible amplitude at the computational inflow and outflow boundaries, and the remaining part of the unsteady perturbation, consisting of convected and nearly convected disturbances, is simply convected out of the near-field domain through the computational outflow boundary.

The numerical results indicate that the far-field eigenanalysis is capable of providing reasonable solutions for the axial eigenvalues and the radial pressure modes (e.g.,see Figures 11, 12, and 13) of the acoustic excitations and responses that can exist far upstream and far downstream of a blade row. At this point, we have not applied the eigenanalysis to predict the axial eigenvalues and radial eigenmodes associated with nearly convected disturbances. The behavior of such disturbances is not well understood at present, as far-field eigenanalyses for non-uniform mean flows have become available only recently. However, it will be necessary to provide accurate numerical representations of nearly-convected, predominantly vortical, disturbances to predict the unsteady aerodynamic responses associated with wake/blade-row interactions.

The TURBO predictions for the zeroth-order or steady relative flow at $M_{-\infty}^{\text{abs}} = M_{\xi,-\infty} = 0.4015$ through the 3D 10th Standard Cascade shows moderate variations in the blade-surface Mach numbers with radius, (Figure 4), and small variations in blade loading. In addition, the 3D Euler predictions for the surface Mach numbers at blade midspan are in close agreement with 2D full-potential predictions. The 3D 10th Standard Cascade operates in a uniform, axial, absolute, mean inlet flow, but, because of steady blade loading, the mean flow far downstream of the blade row (Figure 5) has swirl and axial shear.

The TURBO local unsteady response predictions , i.e., w_C vs ξ, (Figures 6, 7 and 9) for the 3D 10th Standard Cascade, undergoing pure torsional and pure bending vibrations at $\omega = 1$, show small variations with radius and, for the most part, the results at midspan, are in good agreement with the 3D LINFLUX and 2D LINFLO predictions. However, the TURBO and LINFLUX local work-per-cycle results for a superresonant bending vibration at $\sigma = 90$ deg are significantly different from the 2D LINFLO predictions. We suspect that these differences are due to an inadequate resolution, of the local, high wave number, upstream traveling, acoustic response disturbances that occur at high-subsonic Mach numbers. For the subresonant bending vibration at $\sigma = -90$ deg, the 3D LINFLUX and 2D LINFLO results show good agreement, but the TURBO predictions do not agree with those of the two linear analyses. Furthermore, the convergence of the work-per-cycle for this subresonant bending vibration case using TURBO is very slow. We do not have an explanation for the slow convergence of the work-per-cycle calculations, and the discrepancies between the TURBO and LINFLUX solutions along the blade surfaces.

The TURBO, LINFLUX and LINFLO global work per cycle, W_C vs σ, predictions for torsional and bending vibrations (Figure 10) are in very good agreement. However, the global results for the bending vibrations must be interpreted with some caution, as the local responses differ along surfaces at several interblade phase angles.

We have presented some numerical results for unsteady flows through a realistic transonic fan, i.e., the NASA Rotor 67. Our ultimate goal is to use the 3D TURBO analysis for aeromechanical stability assessment of turbomachinery blades. For the unsteady flows considered herein, the eigenanalyses have been used to determine the first two or three modal acoustic disturbances. Although, we have a reasonable understanding of the eigenanlysis for subsonic mean flows, such as those associated with the 3D 10th Standard Cascade, we do not know how reliable this analysis is for supersonic flows. As discussed previously, sometimes, there are missing or superfluous modes. We do not know whether or not these modes seriously deteriorate the solutions.

Nevertheless, some interesting trends have been observed from the results of the TURBO unsteady analysis of Rotor 67 undergoing bending and torsional vibrations. The analysis shows the bending vibrations at $N_D = 0$ and $N_D = 11$ to be quite stable, much more so than for the blades undergoing corresponding torsional vibrations. Also, for both torsional and bending vibrations, the blades are less stable at $N_D = 0$ than at $N_D = 11$. In addition, the torsional mode of vibration becomes slightly more stable as back pressure increases, while the bending mode of vibration becomes less stable as back pressure increases. In general, all these trends seem to agree with those observed for classical supersonic unstalled flutter, which is usually associated with a torsional mode, and subsonic/transonic high-incidence flutter, which is usually associated with a bending mode.

7. Concluding Remarks

The TURBO[JHW92], nonlinear, unsteady, aerodynamic analysis has been extended for turbomachinery aeroelastic applications. This analysis is based on the Euler/Navier-Stokes equations of fluid motion; a near-field, implicit, flux-split, finite-volume, analysis; and far-field eigenanalyses for the unsteady perturbations of fully-developed, axisymmetric, swirling mean flows. The far-field eigenanalyses, which are coupled to the near-field finite-volume analysis at computational inflow and outflow boundaries, allow incoming external aerodynamic excitations to be prescribed, and acoustic response disturbances to pass through these computational boundaries without spurious reflections. Under the current effort, no external aerodynamic excitations have been considered.

We have applied the TURBO analysis to predict unsteady subsonic flows through a simple turbomachinery configuration, i.e., a three-dimensional version of the 10th Standard Cascade Configuration. We have also applied this analysis to predict unsteady flows through a realistic transonic fan, i.e., the NASA Rotor 67. We have considered unsteady flows excited by prescribed blade vibrations that are highly two dimensional. For the 3D 10th Standard Cascade, this allows us to compare and validate TURBO results against predictions based on previous two-dimensional analyses.

The numerical results indicate that the current version of the TURBO code is capable of providing accurate aerodynamic response information for unsteady subsonic flows, provided that the grids employed have a sufficient overall density and local clusterings in regions of high flow gradients. In particular, the numerical results indicate that the axial eigenvalues and radial eigenmodes of far-field acoustic disturbances can be accurately represented, and that the 3D blade-surface, response predictions show reasonable radial trends. The TURBO results at blade midspan and the 2D LINFLO results for the 3D 10th Standard Cascade are in good qualitative agreement, but in some cases significant quantitative differences occur. The differences occur along the suction surfaces of the blades, where steady Mach numbers are close to one, and upstream of the blade row. Some evidence [MV97] suggests that the quantitative differences between the TURBO and LINFLO results can be eliminated if the meshes used in the TURBO calculations are of sufficient density and the grid lines are properly distributed.

Based on the numerical results presented in this report, it appears that the far-field eigensolver, developed for the TURBO code, is working properly and that it has been successfully coupled with the near-field numerical algorithm. Also, the TURBO analysis can yield useful response information for unsteady flows excited by blade vibrations. However, the proper treatment of superharmonic and anharmonic waves needs further investigation. In addition, the mesh requirements for accurately resolving such flows must be better understood. The requirements for flutter applications, for which reduced frequencies are typically of order one, can be readily met, but those for forced response studies, in which reduced frequencies on the order of 5 to 50 must be considered, will impose serious constraints on available computational resources.

To improve the efficiency of TURBO steady and unsteady calculations, a number of computational strategies should be investigated. For example, a rotating-frame version of the TURBO analysis could be constructed to allow more efficient predictions of nonlinear, steady flows via the use of convergence accelerating schemes. Also, second-order accurate, surface boundary conditions could be incorporated into TURBO to reduce the time required to achieve converged low-loss, steady and unsteady solutions. In addition, a single-passage version of the TURBO analysis with time-lagged periodic boundary conditions should be considered. This will greatly reduce the computational requirements for unsteady flows in which the structural vibratory pattern has a non-zero nodal diameter. Finally, a parallel version of TURBO should be considered, particularly for viscous and high-frequency unsteady flows.

To date, we have focused on demonstrating and validating inviscid version of the TURBO code for flutter applications. In addtion, we have applied the code to predict flutter in transonic inviscid flows. However, the code needs further validation for transonic flows. Also, viscous effects are expected to play an important role in the analysis of high-incidence flutter. Thus, a validation the viscous capabilities of the TURBO code for unsteady applications should be carried out.

References

[Arn93] A. Arnone, *Viscous Analysis of Three-Dimensional Rotor Flow Using a Multigrid Method*, ASME Paper 93–GT–323, International Gas Turbine and Aeroengine Congress & Exhibition, Cincinnati, Ohio, May 24–27, 1993.

[AV94] T. C. Ayer and J. M. Verdon, *Numerical Unsteady Aerodynamic Simulator for Blade Forced Response Phenomena*, Contractor Report WL–TR–95–2011, prepared for the GUIde Consortium under U. S. Air Force Contract F33615–92–C–2212, December 1994.

[AV96] T. C. Ayer and J. M. Verdon, *Validation of a Nonlinear Unsteady Aerodynamic Simulator for Vibrating Blade Rows*, ASME Paper 96–GT–340, International Gas Turbine and Aeroengine Congress & Exhibition, Birmingham, UK, June 10–13, 1996.

[BH92] T. A. Beach and G. Hoffman, *IGB Grid: User's Manual (A Turbomachinery Grid Generation Code)*, CR 189104, NASA, January 1992.

[BL78] B. S. Baldwin and H. Lomax, *Thin-Layer Approximation and Algebraic Model for Separated Turbulent Flow*, AIAA Paper 78–257, 16th Aerospace Sciences Meeting, Huntsville, Alabama, January 16–18, 1978.

[BSK97] M. A. Bakhle, R. Srivastava, and T. G. Keith, Jr., *A 3D Euler/Navier-Stokes Aeroelastic Code for Propulsion Applications*, AIAA Paper 97–2749, 33rd Joint Propulsion Conference, Seattle, Washington, July 6–9, 1997.

[Cas83] J. R. Caspar, *Unconditionally Stable Calculation of Transonic Potential Flow through Cascades using an Adaptive Mesh for Shock Capture*, Transactions of the ASME: Journal of Engineering for Power **105** (1983), no. 3, 504–513.

[CCA94] J. P. Chen, M. L. Celestina, and J. J. Adamczyk, *A New Procedure for Simulating Unsteady Flows through Turbomachinery Blade Passages*, ASME Paper 94–GT–151, International Gas Turbine and Aeroengine Congress & Exhibition, June 1994.

[Chi91] R. V. Chima, *Viscous Three-Dimensional Calculations of Transonic Fan Performance*, Tech. Report TM–103800, NASA, 1991.

[CW93] J. P. Chen and D. L. Whitfield, *Navier-Stokes Calculations for the Unsteady Flowfield of Multi-stage Turbomachinery*, Paper 93-0676, AIAA 31st Aerospace Sciences Meeting and Exhibit, Reno, Nevada, January 11–14, 1993.

[DV94] D. J. Dorney and J. M. Verdon, *Numerical Simulations of Unsteady Cascade Flows*, Trans. of the ASME: Journal of Turbomachinery **116** (1994), no. 4, 665–675.

[FV93] T. H. Fransson and J. M. Verdon, *Standard Configurations for Unsteady Flow through Vibrating Axial-Flow Turbomachine Cascades*, Unsteady Aerodynamics, Aeroacoustics and Aeroelasticity of Turbomachines and Propellers, Edited by H. M. Atassi, Springer-Verlag, New York, 1993, pp. 859–889.

[GA96] V. V. Golubev and H. M. Atassi, *Acoustic-Vorticity Waves in Swirling Flows*, Technical Report, Department of Aerospace and Mechanical Engineering, University of Notre Dame, Notre Dame, Indiana, 1996.

[GC96] B. Gruber and V. Carstens, *Computation of the Unsteady Transonic Flow in Harmonically Oscillating Turbine Cascades Taking into Account Viscous Effects*, ASME Paper 96–GT–338, ASME International Gas Turbine and Aeroengine Congress & Exhibition, Birmingham, UK, June 10–13, 1996.

[Gil88] M. B. Giles, *Calculation of Unsteady Wake Rotor Interaction*, Journal of Propulsion and Power **4** (1988), no. 4, 356–362.

[GV94] G. A. Gerolymos and I. Vallet, *Validation of 3D Euler Methods for Vibrating Cascade Aerodynamics*, Paper 94–GT–294, ASME International Gas Turbine and Aeroengine Congress and Exposition, 1994.

[HCL94] K. C. Hall, W. S. Clark, and C. B. Lorence, *A Linearized Euler Analysis of Unsteady Transonic Flows in Turbomachinery*, Transactions of the ASME: Journal of Turbomachinery **116** (1994), no. 3, 477–488.

[HD93] L. He and J. D. Denton, *Three Dimensional Time-Marching Inviscid and Viscous Solutions for Unsteady Flows around Vibrating Blades*, ASME Paper 93–GT–92, 38th International Gas Turbine and Aeroengine Congress and Exposition, Cincinnati, Ohio, May 24–27, 1993.

[HL93] K. C. Hall and C. B. Lorence, *Calculation of Three-Dimensional Unsteady Flows in Turbomachinery Using the Linearized Harmonic Euler Equations*, Transactions of the ASME: Journal of Turbomachinery **115** (1993), no. 4, 800–809.

[HR89] D. L. Huff and T. S. R. Reddy, *Numerical Analysis of Supersonic Flow Through Oscillating Cascade Sections by Using a Deforming Grid*, Paper 89–2805, AIAA 25th Joint Propulsion Conference, Monterey, California, July 10–12, 1989.

[Jan89] J. M. Janus, *Advanced 3-D CFD Algorithm for Turbomachinery*, Ph.D. thesis, Mississippi State University, Mississippi State, Mississippi, May 1989.

[JHW92] J. M. Janus, H. Z. Horstman, and D. L. Whitfield, *Unsteady Flowfield Simulation of Ducted Prop-Fan Configurations*, Paper 92–0521, AIAA 30th Aerospace Sciences Meeting and Exhibit, Reno, Nevada, January 6-9, 1992.

[JT92] I. K. Jennions and M. G. Turner, *Three-Dimensional Navier-Stokes Computations of Transonic Fan Flow Using an Explicit Flow Solver and an Implicit k-ϵ Solver*, ASME Paper 92–GT–309, International Gas Turbine and Aeroengine Congress & Exhibition, 1992.

[JW89] J. M. Janus and D. L. Whitfield, *A Simple Time-Accurate Turbomachinery Algorithm with Numerical Solutions of an Uneven Blade Count Configuration*, Paper 89–0206, AIAA 27th Aerospace Sciences Meeting, Reno, Nevada, January 9-12, 1989.

[JW90] J. M. Janus and D. L. Whitfield, *Counterrotating Prop-Fan Simulations which Feature a Relative-Motion Multiblock Grid Decomposition Enabling Arbitrary Time Steps*, Paper 90–0687, AIAA 28th Aerospace Sciences Meeting, Reno, Nevada, January 8-11, 1990.

[Kou95] K. A. Kousen, *Eigenmode Analysis of Ducted Flows with Radially Dependent Axial and Swirl Components*, Proceedings of the First Joint CEAS/AIAA Aeroacoustics Conference, *Vol, II* (Munich, Germany), June 12–15 1995, pp. 1085–1094.

[MV95] M. D. Montgomery and J. M. Verdon, *A Linearized Unsteady Euler Analysis for Turbomachinery Blade Rows Using an Implicit Wave-Split Scheme*, Unsteady Aerodynamics and Aeroelasticity of Turbomachines, Edited by Y. Tanida and M. Namba, Elsevier, Amsterdam, 1995, pp. 143–160.

[MV97] M. D. Montgomery and J. M. Verdon, *A Three Dimensional Linearized Unsteady Euler Analysis for Turbomachinery Blade Rows*, NASA CR 4770, March 1997, prepared under Contract NAS3–26618 for NASA Lewis Research Center.

[PGW96] D. Peitsch, H. E. Gallus, and S. Weber, *Numerical Investigation of the Unsteady Transonic 3D-Flow in Stator and Rotor Cascades with Oscillating Blades*, ASME Paper 96–GT–307, ASME International Gas Turbine and Aeroengine Congress & Exhibition, Birmingham, UK, June 10–13, 1996.

[Rai87] M. M. Rai, *Navier-Stokes Simulations of Rotor-Stator Interaction Using Patched and Overlaid Grids*, AIAA Journal of Propulsion and Power **3** (1987), no. 5, 387–396.

[Rai89] M. M. Rai, *Three-Dimensional Navier-Stokes Simulations of Turbine Rotor-Stator Interaction; Part 1 – Methodology, Part 2 – Results*, AIAA Journal of Propulsion and Power **5** (1989), no. 3, 305–319.

[Roe81] P. L. Roe, *Approximate Riemann Solvers, Parameter Vectors and Difference Schemes*, Journal of Computational Physics **43** (1981), 357–372.

[RZH+93] C. M. Rhie, R. M. Zacharias, D. E. Hobbs, K. P. Sarathy, B. P. Biederman, C. R. Lejambre, and D. A. Spear, *Advanced Transonic Fan Design Procedure Based on a Navier-Stokes Method*, ASME Paper 93–GT–323, International Gas Turbine and Aeroengine Congress & Exhibition, Cincinnati, Ohio, May 24–27, 1993.

[Sid91] L. D. G. Siden, *Numerical Simulation of Unsteady Viscous Compressible Flows Applied to Blade Flutter Analysis*, ASME Paper 91–GT–203, International Gas Turbine and Aeroengine Congress and Exposition, Orlando, Florida, June 3–6, 1991.

[Sre96] K. Sreenivas, *Linearized Euler Analysis of Turbomachinery*, Ph.D. thesis, Mississippi State University, December 1996.

[SS91] B. K. Soni and M. H. Shih, *TIGER: Turbomachinery Interactive Grid GenERation*, Proceedings of the Third International Conference on Numerical Grid Generation in CFD (Barcelona, Spain), June 1991.

[SW81] J. L. Steger and R. F. Warming, *Flux Vector Splitting of the Inviscid Gasdynamic Equations with Application to Finite Difference Methods*, Journal of Computational Physics **40** (1981), no. 2, 263–293.

[SWHS89] A. J. Strazisar, J. R. Wood, M. D. Hathaway, and K. L. Suder, *Laser Anemometer Measurements in a Transonic Axial-Flow Fan Rotor*, Tech. Report TP–2879, NASA, 1989.

[TS62] J. M. Tyler and T. G. Sofrin, *Axial Flow Compressor Noise Studies*, SAE Transactions **70** (1962), 309–332.

[Ver89a] J. M. Verdon, *The Unsteady Aerodynamic Response to Arbitrary Modes of Blade Motion*, Journal of Fluids and Structures **3** (1989), no. 3, 255–274.

[Ver89b] J. M. Verdon, *The Unsteady Flow in the Far Field of an Isolated Blade Row*, Journal of Fluids and Structures **3** (1989), no. 2, 123–149.

[Ver93] J. M. Verdon, *Unsteady Aerodynamic Methods for Turbomachinery Aeroelastic and Aeroacoustic Applications*, AIAA Journal **31** (1993), no. 2, 235–250.

[VL74] B. Van Leer, *Towards the Ultimate Conservative Differencing Scheme, Part II*, Journal of Computational Physics **14** (1974), no. 4, 361–370.

[VMK95] J. M. Verdon, M. D. Montgomery, and K. A. Kousen, *Development of a Linearized Unsteady Euler Analysis for Turbomachinery Blade Rows*, NASA CR 4677, prepared under Contract NAS3–25425 for NASA Lewis Research Center, June 1995.

[Whi90] D.L. Whitfield, *Newton-Relaxation Schemes for Nonlinear Hyperbolic Systems*, Report MSSU–EIRS–ASE–90–3, Mississippi State Engineering and Industrial Research Station, Mississippi State University, Mississippi, October 1990.

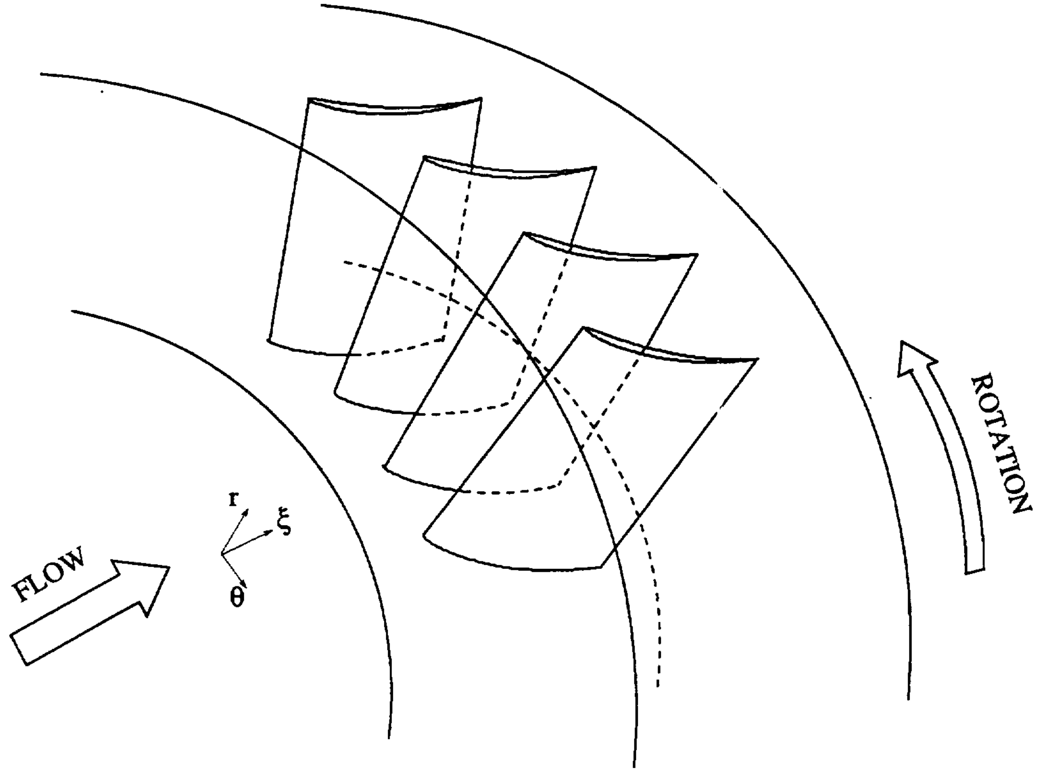

Figure 1: Rotating axial compressor blade row operating within an annular duct.

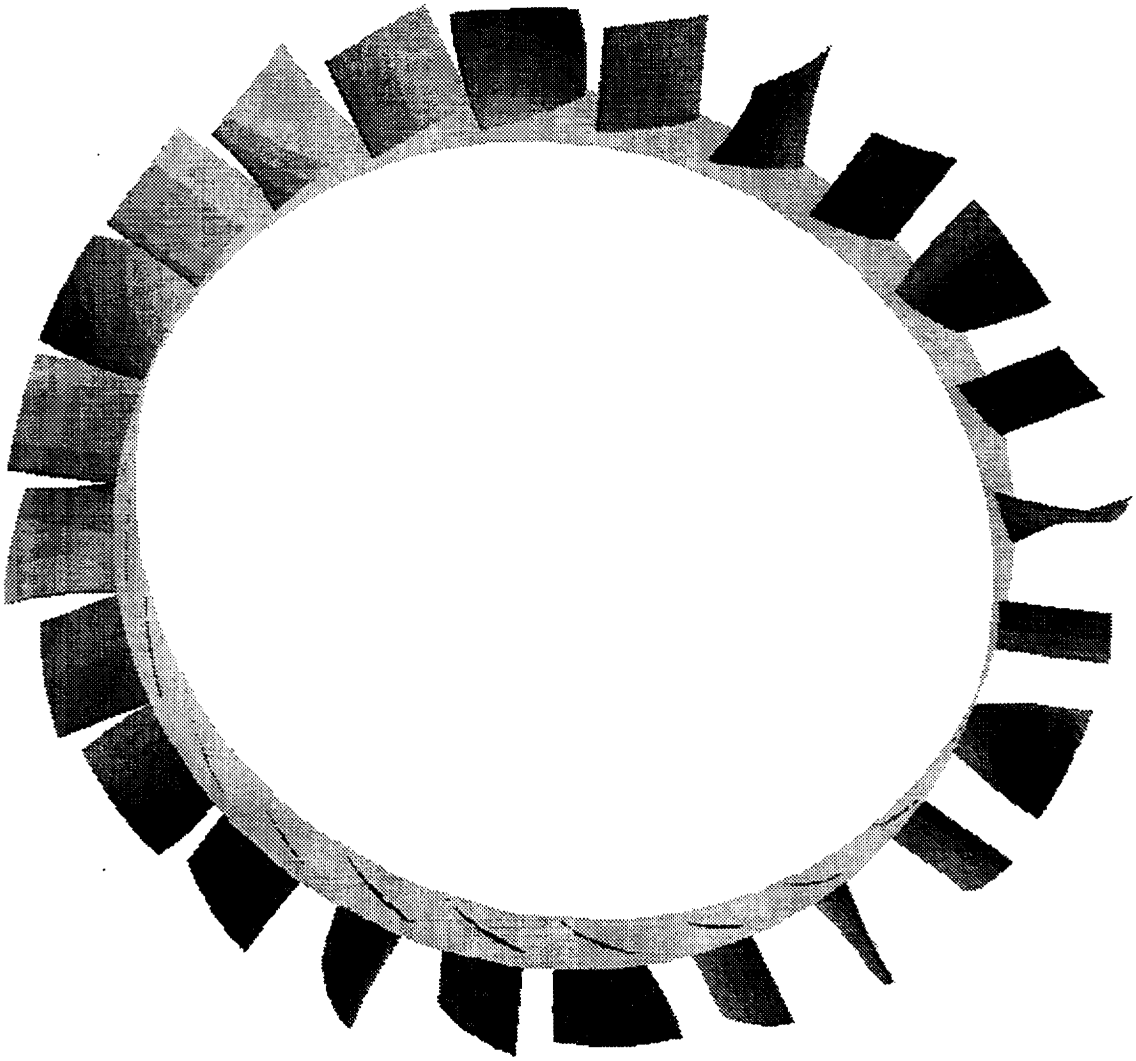

Figure 2: 3D Tenth Standard Configuration undergoing an exaggerated torsional motion ($\alpha_{hub} = 0$ deg, $\alpha_{tip} = 45$ deg). The rotor consists of 24 airfoils. The nodal diameter of the blade motion is 6, which results in an interblade phase angle of 90 deg. The outer casing has been eliminated from the figure for clarity.

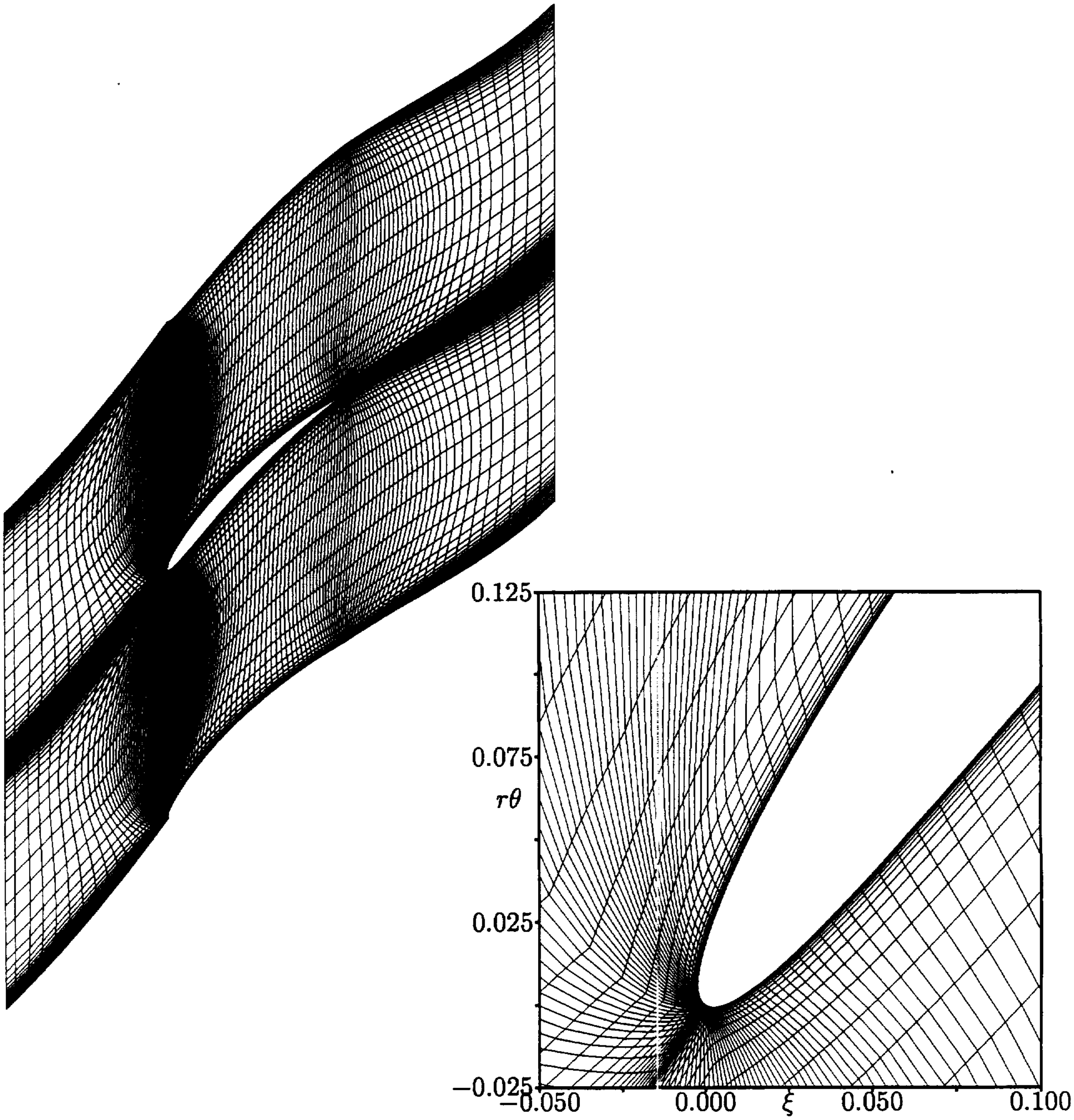

Figure 3: TURBO computational grid at midspan for the 3D 10th Standard Cascade.

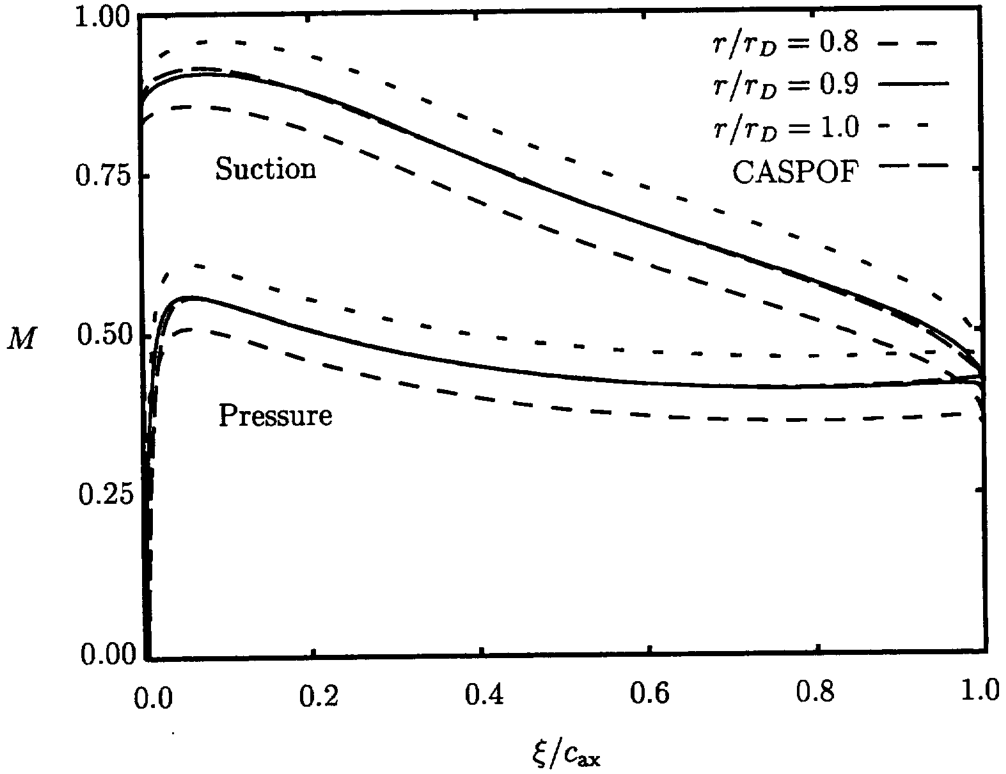

Figure 4: Relative steady isentropic surface mach number distributions for the 3D 10th Standard Cascade ($M_{-\infty}^{\text{abs}} = 0.4015$, $|\Omega| = 0.2145$).

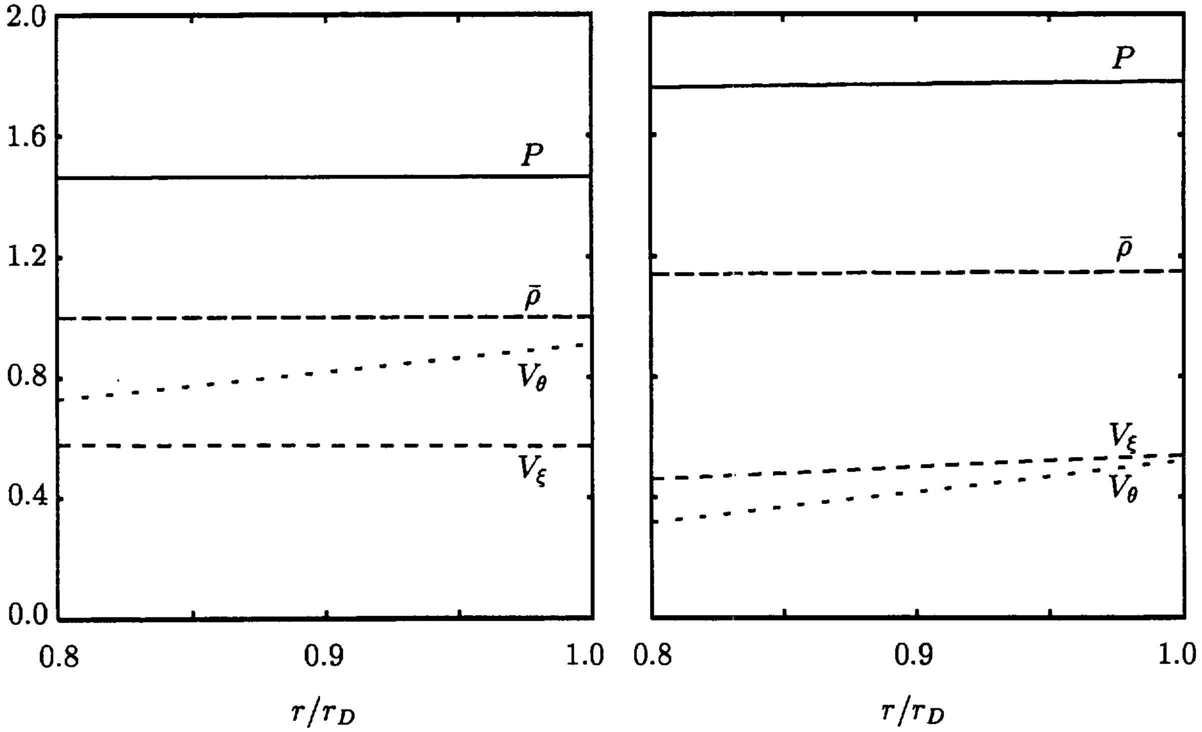

Figure 5: Relative frame steady flow properties far upstream and far downstream of the 3D 10th Standard Cascade ($M_{-\infty}^{\text{abs}} = 0.4015, |\Omega| = 0.2145$).

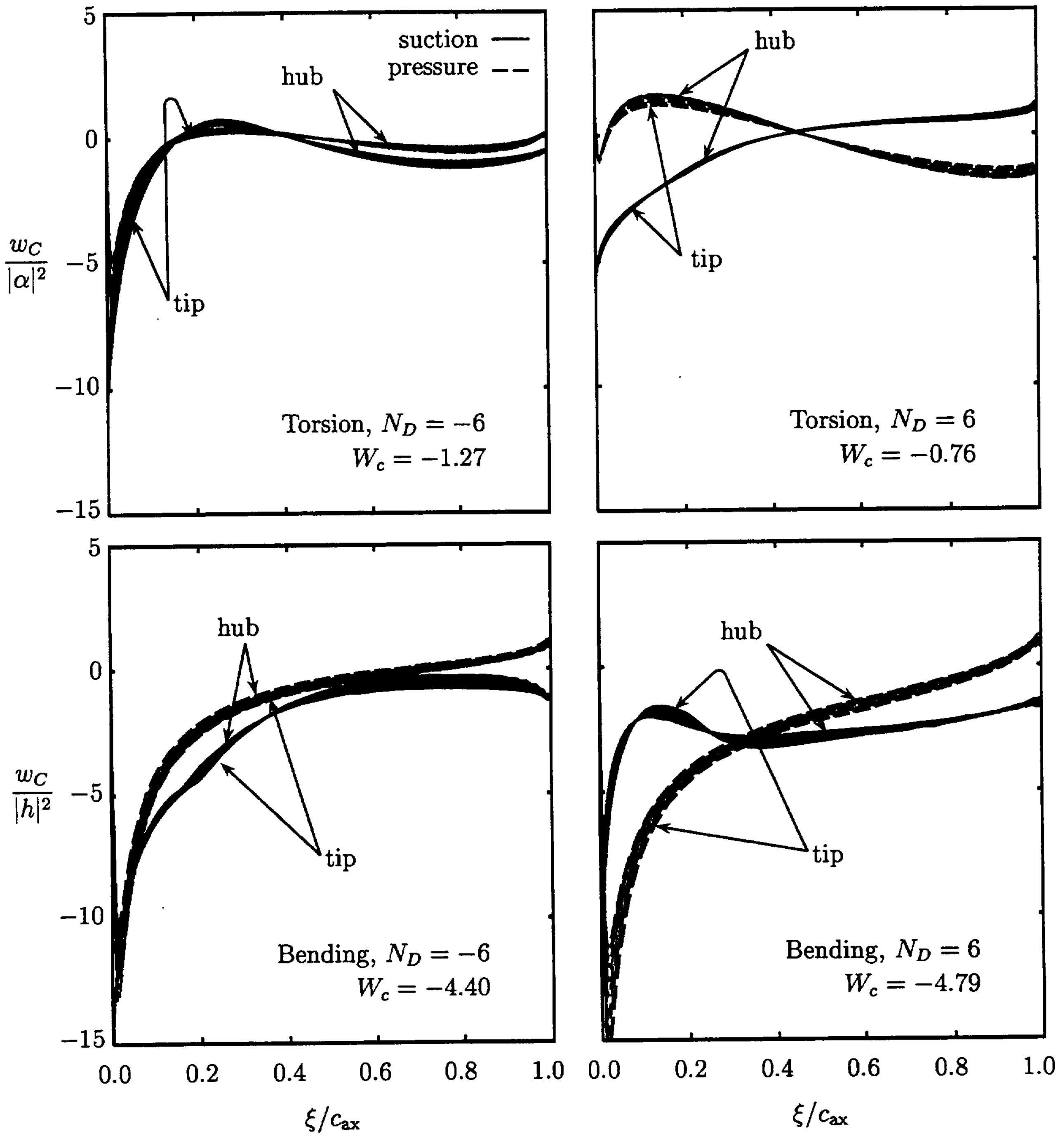

Figure 6: Local work per cycle distributions at all spanwise stations and global works per cycle for the 3D 10th Standard Cascade undergoing pure torsional vibrations about midchord and pure bending vibrations at $\omega = 1$ and $\sigma = \mp 90$ deg ($N_D = \mp 6$).

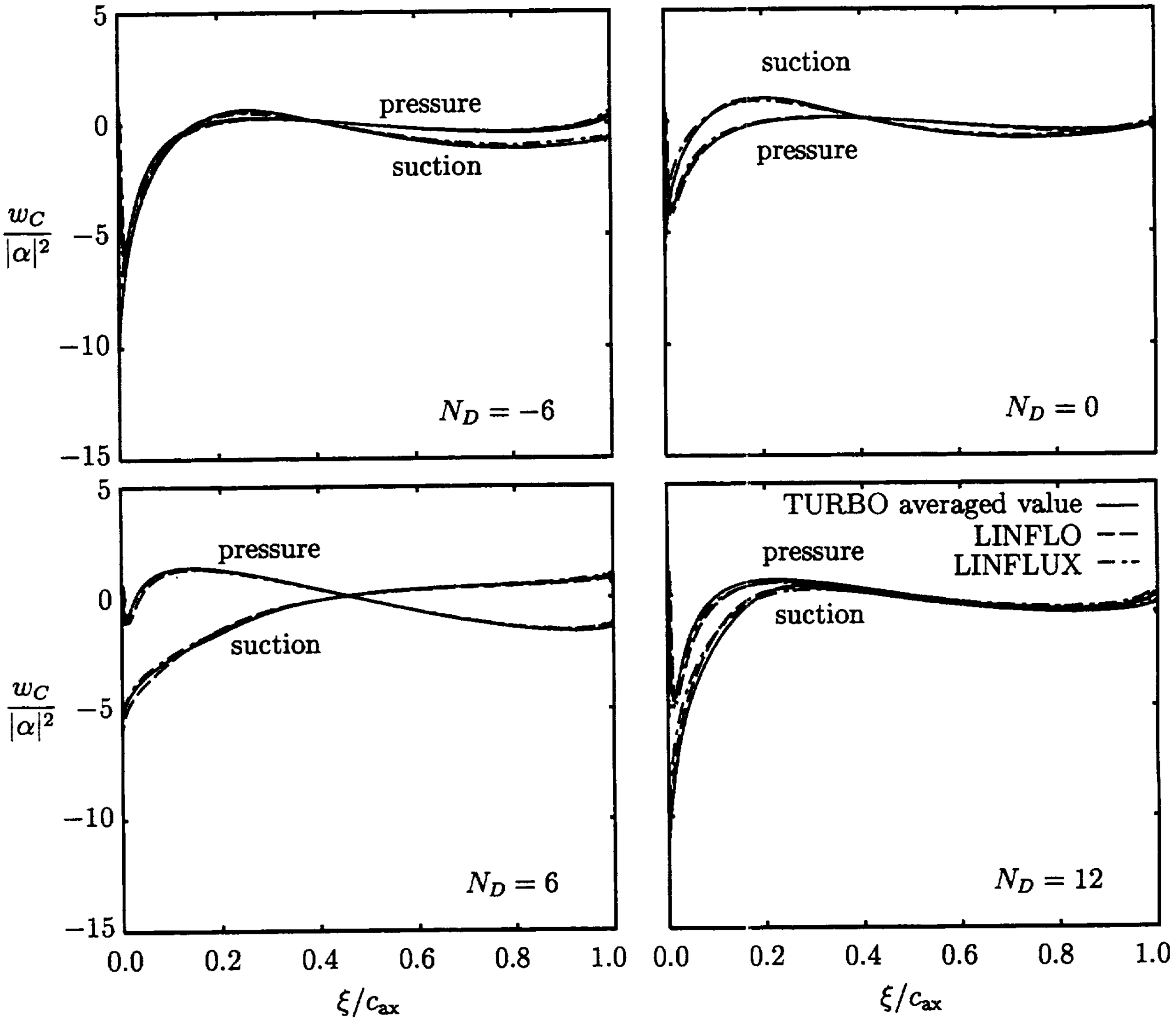

Figure 7: Averaged local work per cycle distributions at midspan, as predicted using the 3D TURBO and the 2D LINFLO analyses, for the 3D 10th Standard Cascade undergoing torsional blade vibrations about midchord at $\omega = 1$.

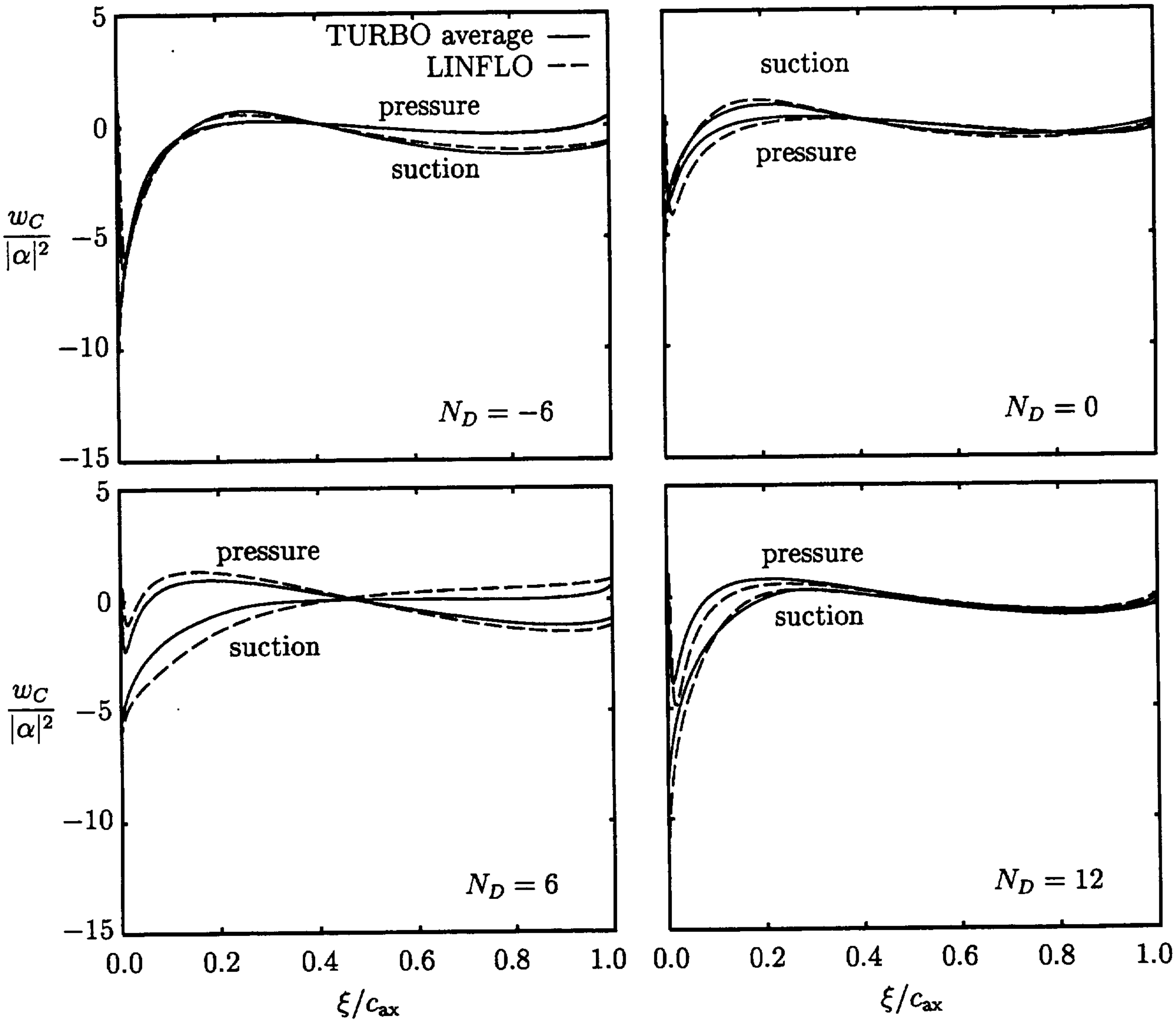

Figure 8: Averaged local work per cycle distributions at midspan, as predicted using the 3D TURBO analysis with one-dimensional, local, far-field conditions and the 2D LINFLO analysis, for the 3D 10th Standard Cascade undergoing torsional blade vibrations about midchord at $\omega = 1$.

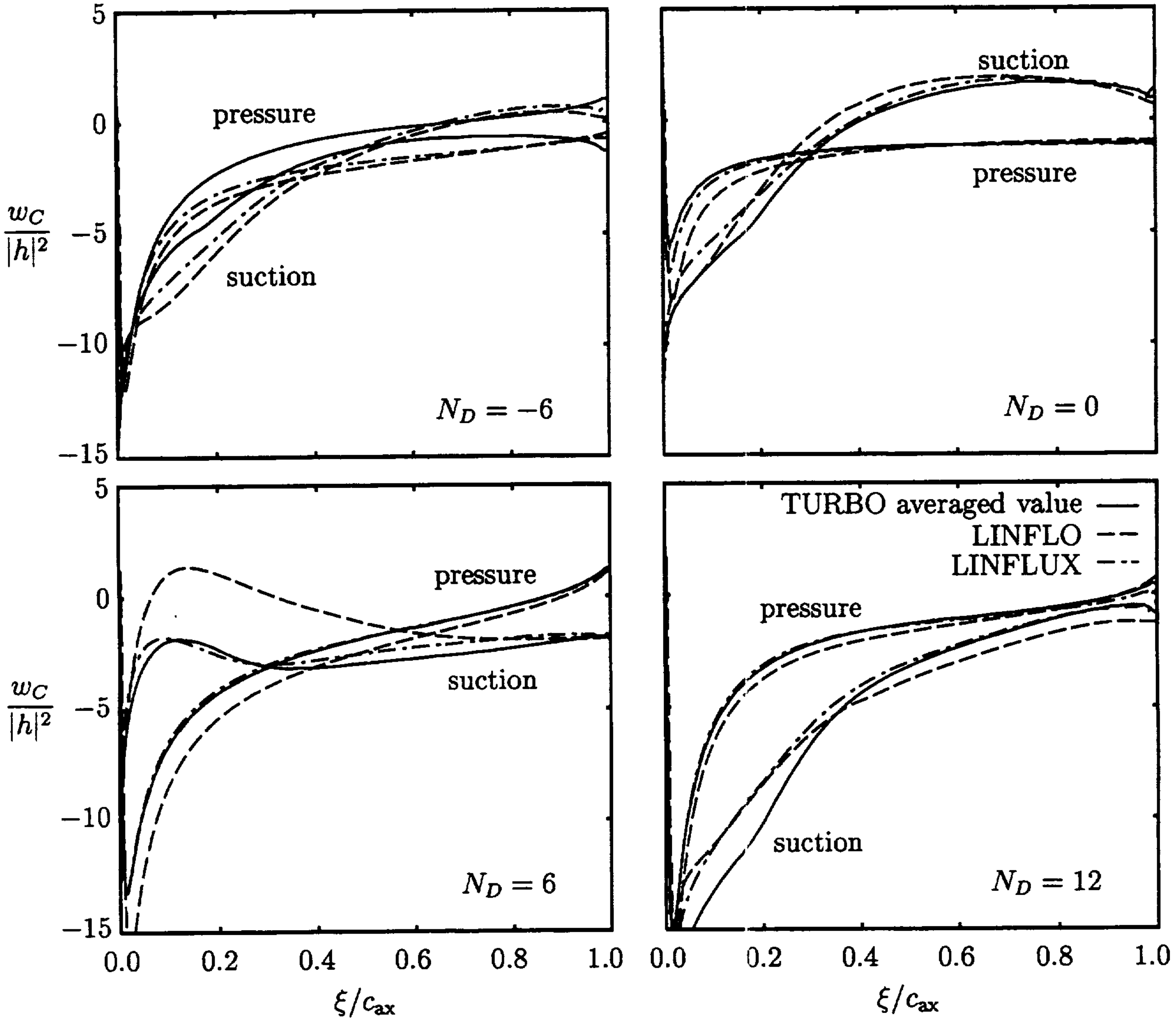

Figure 9: Averaged local work per cycle distributions at midspan, as predicted using the 3D TURBO and the 2D LINFLO analyses, for the 3D 10th Standard Cascade undergoing bending vibrations at $\omega = 1$.

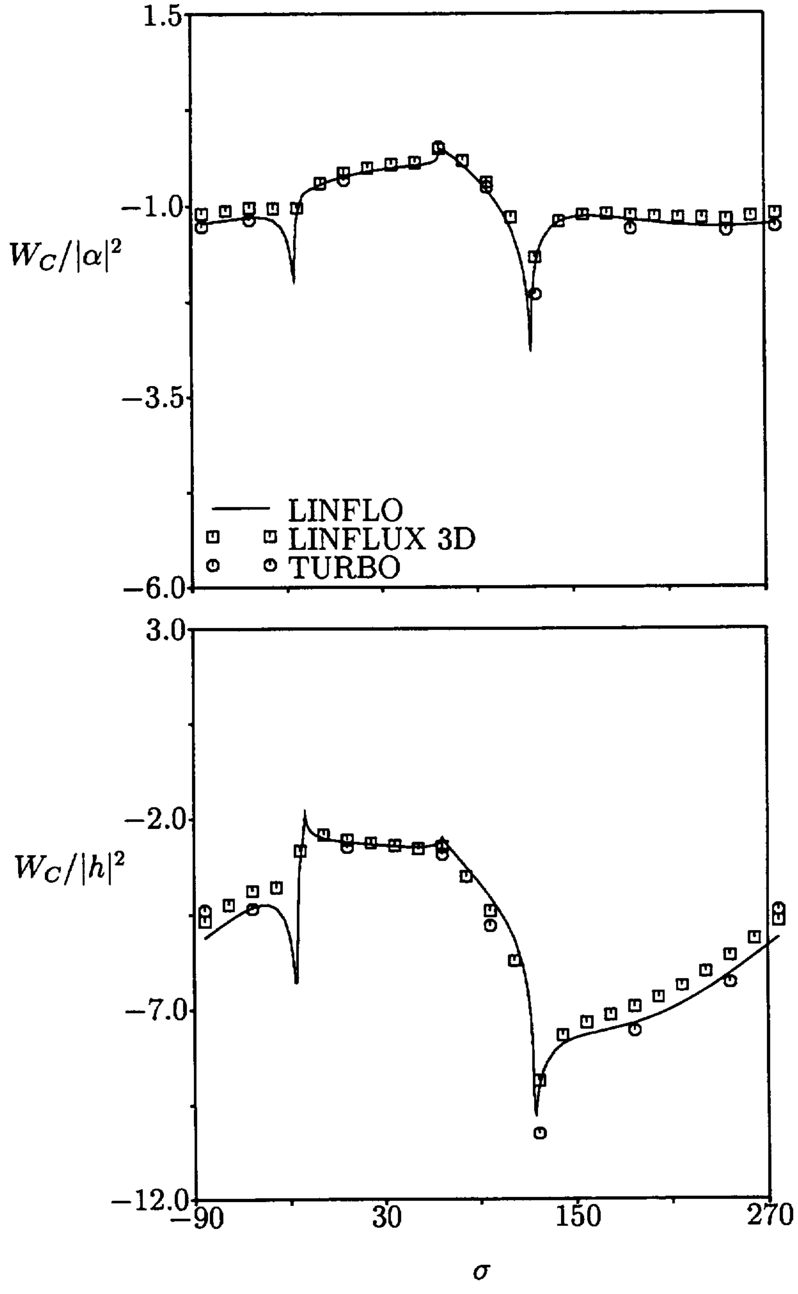

Figure 10: Work per cycle versus interblade phase angle for the 3D 10th Standard Cascade undergoing pure torsional vibrations about midchord (top) and pure bending vibrations (bottom) at $\omega = 1$.

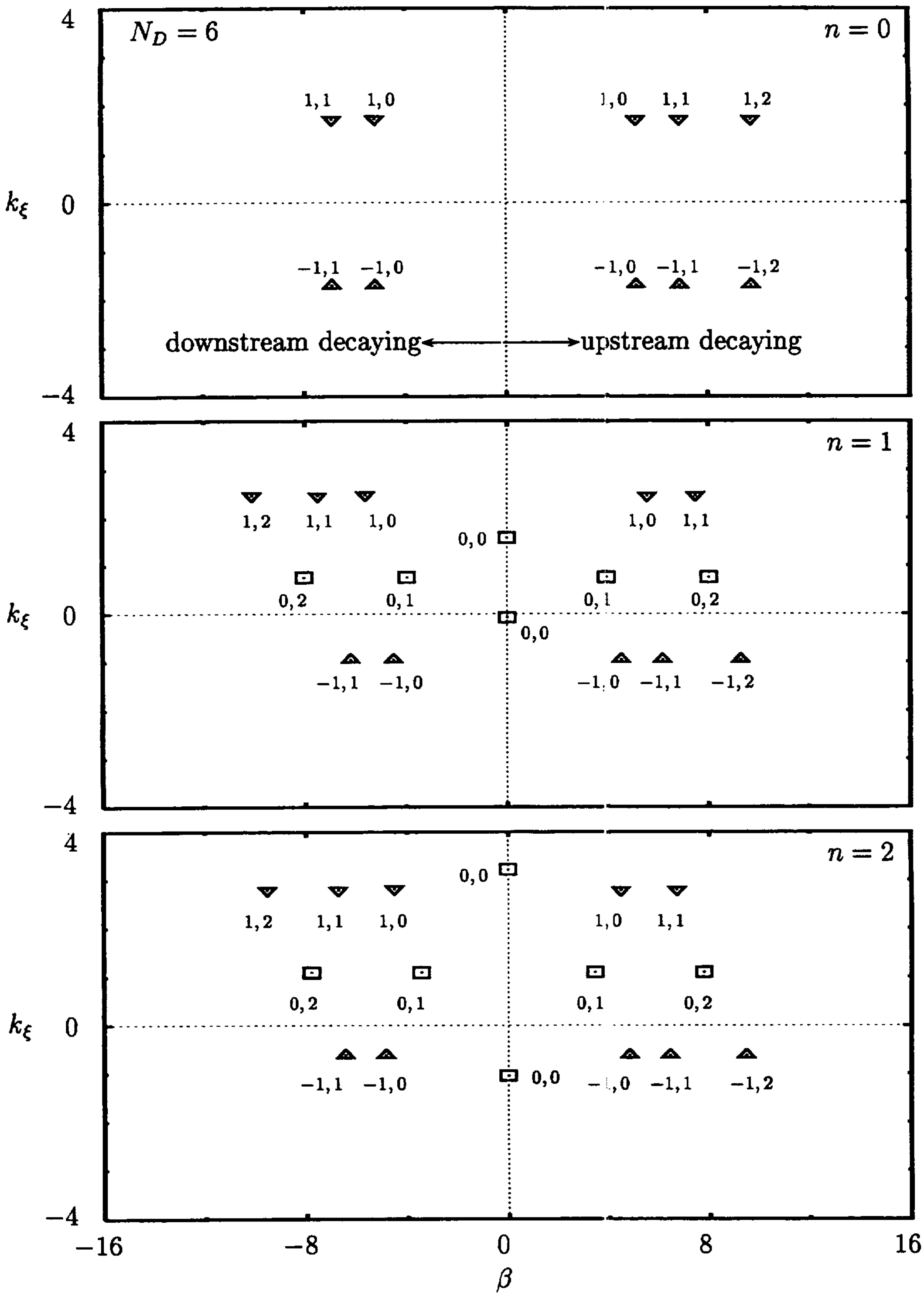

Figure 11: Axial eigenvalues, $\chi = \beta + i\kappa_\xi$, at inlet for three circumferential ($m = -1, 0, 1$) and three radial ($\mu = 0, 1, 2$) modes of steady ($n = 0$), first-harmonic ($n = 1$) and second-harmonic ($n = 2$) acoustic disturbance in an unsteady flow at $\omega = 1.0$ and $N_D = 6$, through the 3D 10th Standard Cascade.

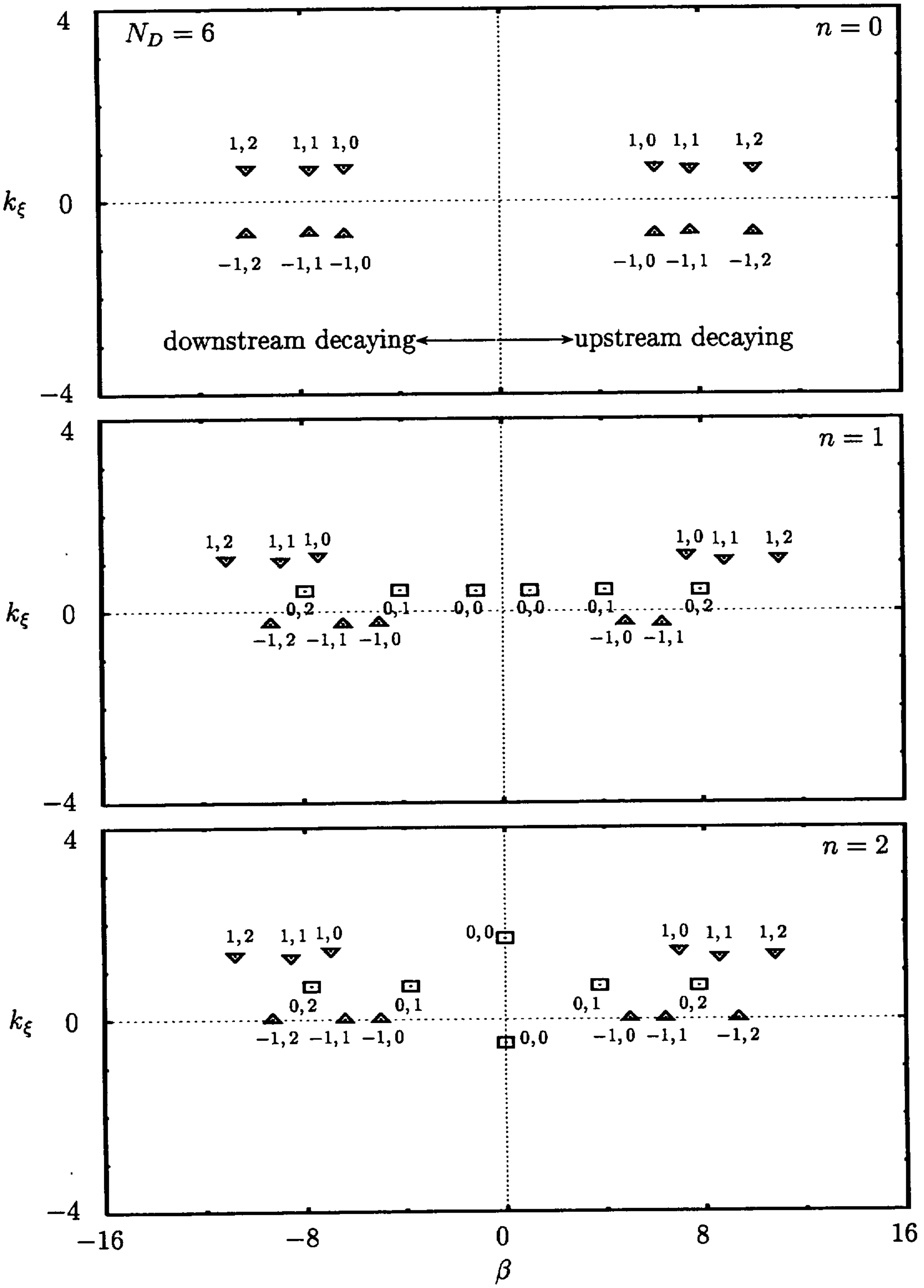

Figure 12: Axial eigenvalues, $\chi = \beta + i\kappa_\xi$, at exit for three circumferential ($m = -1, 0, 1$) and three radial ($\mu = 0, 1, 2$) modes of steady ($n = 0$), first-harmonic ($n = 1$) and second-harmonic ($n = 2$) acoustic disturbance in an unsteady flow at $\omega = 1.0$ and $N_D = 6$, through the 3D 10th Standard Cascade.

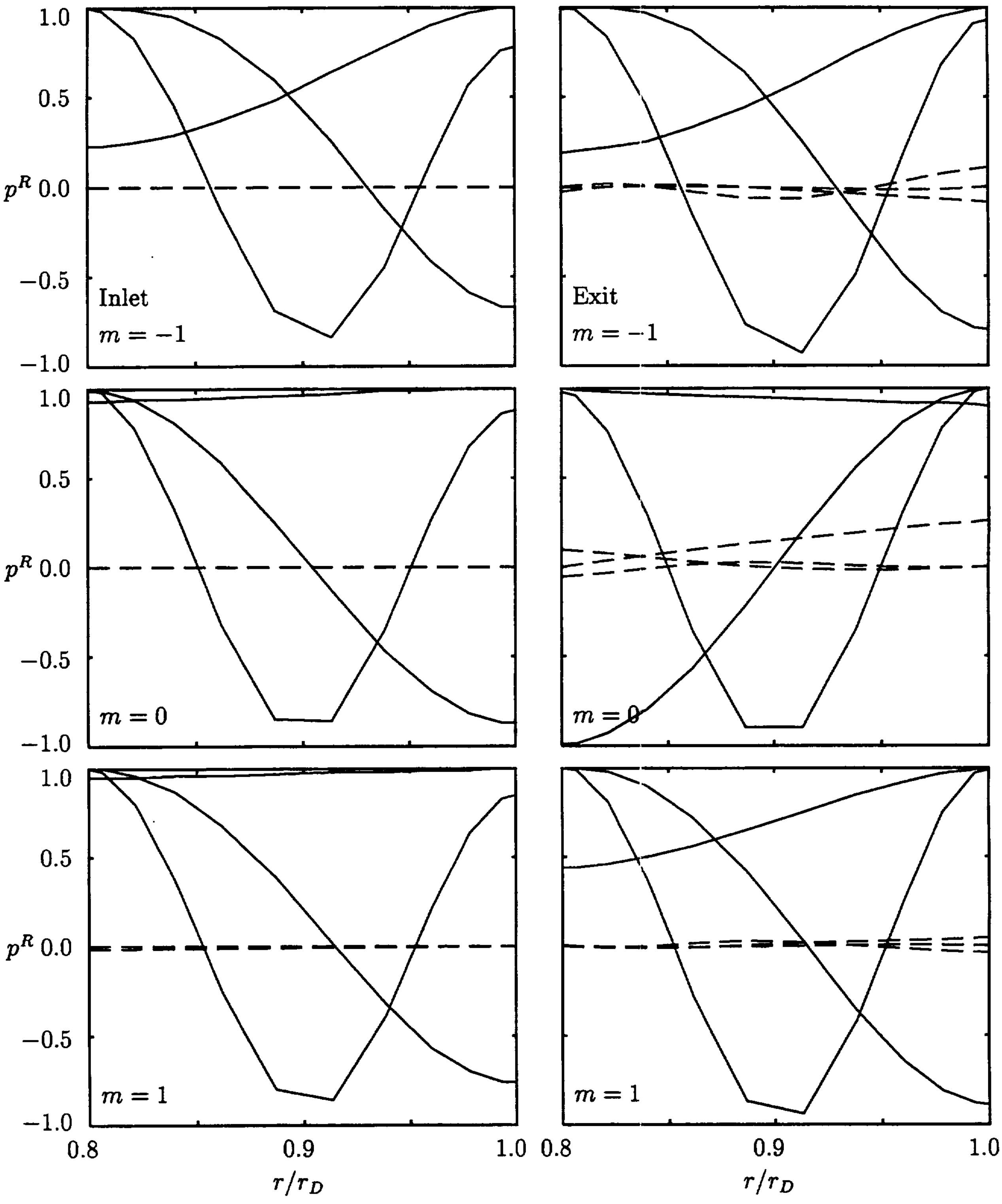

Figure 13: First harmonic, radial, pressure modes, $p^R_{m\mu}(r)$, $m = -1, 0, 1$, $\mu = 0, 1, 2$, at inlet and exit due to an acoustic excitation or response, at $N_D = 6$, far upstream and for an acoustic response, at $N_D = 6$, far downstream of the 3D 10th Standard Cascade: (——) in-phase component; (- - -) out-of-phase component of $p^R_{m\mu}(r)$.

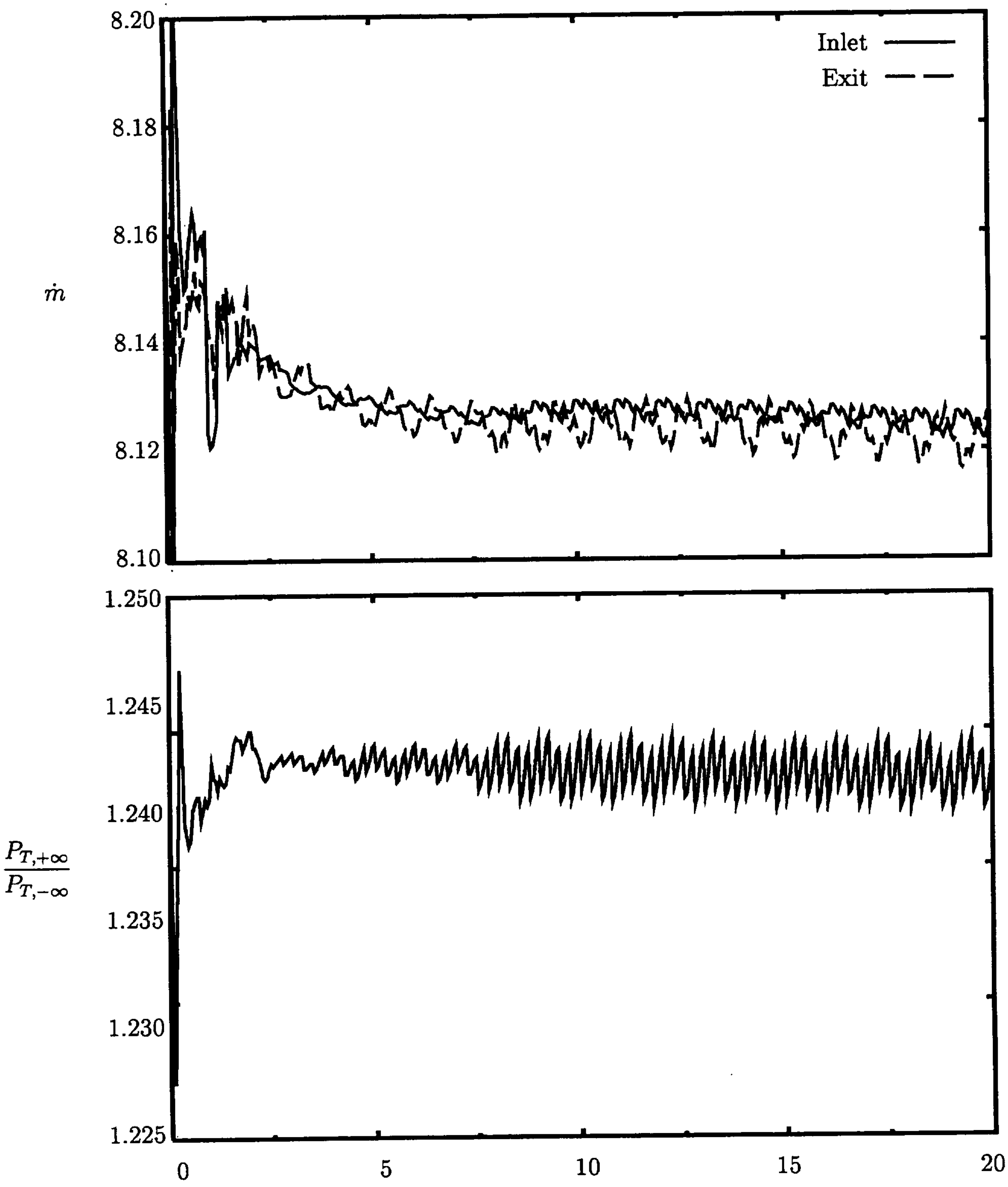

Figure 14: Time histories of mass flow and total pressure ratio for the 3D 10th Standard Cascade undergoing a pure bending vibration at $\omega = 1.0$ and $N_D = -6$.

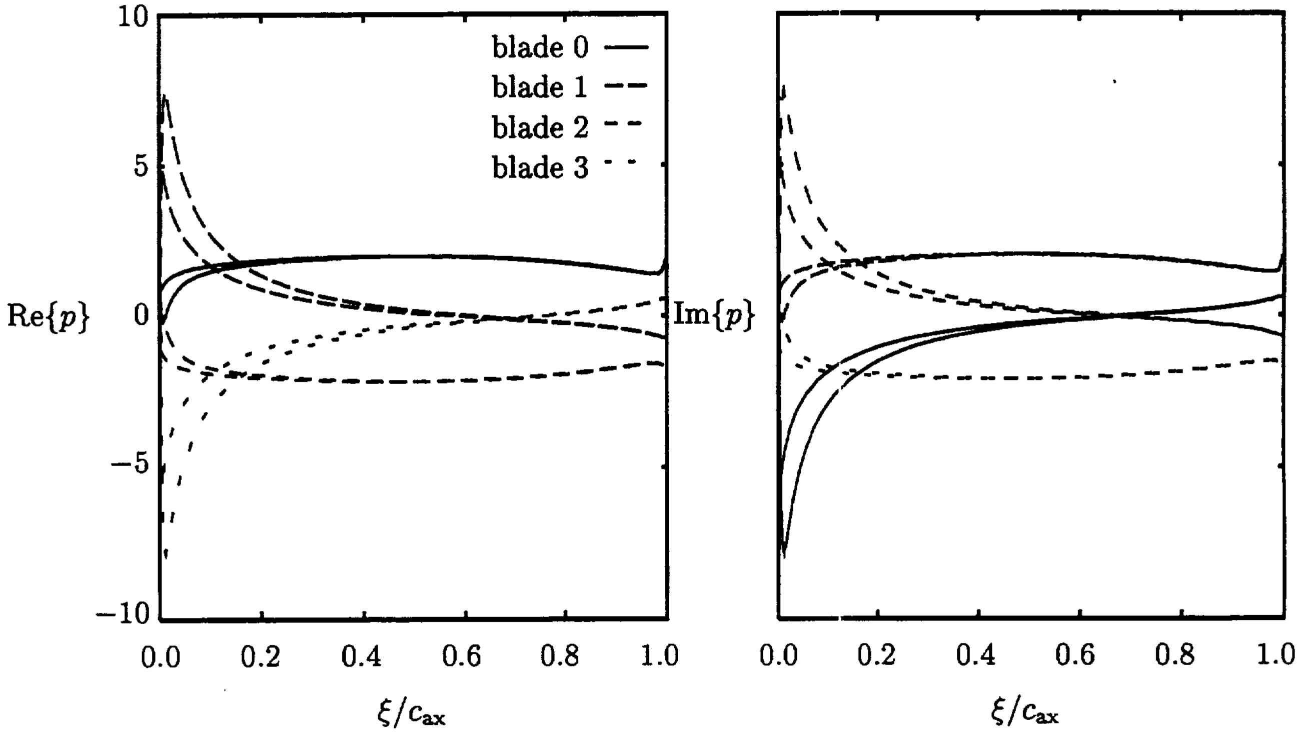

Figure 15: First-harmonic unsteady pressure distributions at midspan acting on four blades of the 3D 10th Standard Cascade undergoing a pure bending vibration at $\omega = 1.0$ and $N_D = -6$.

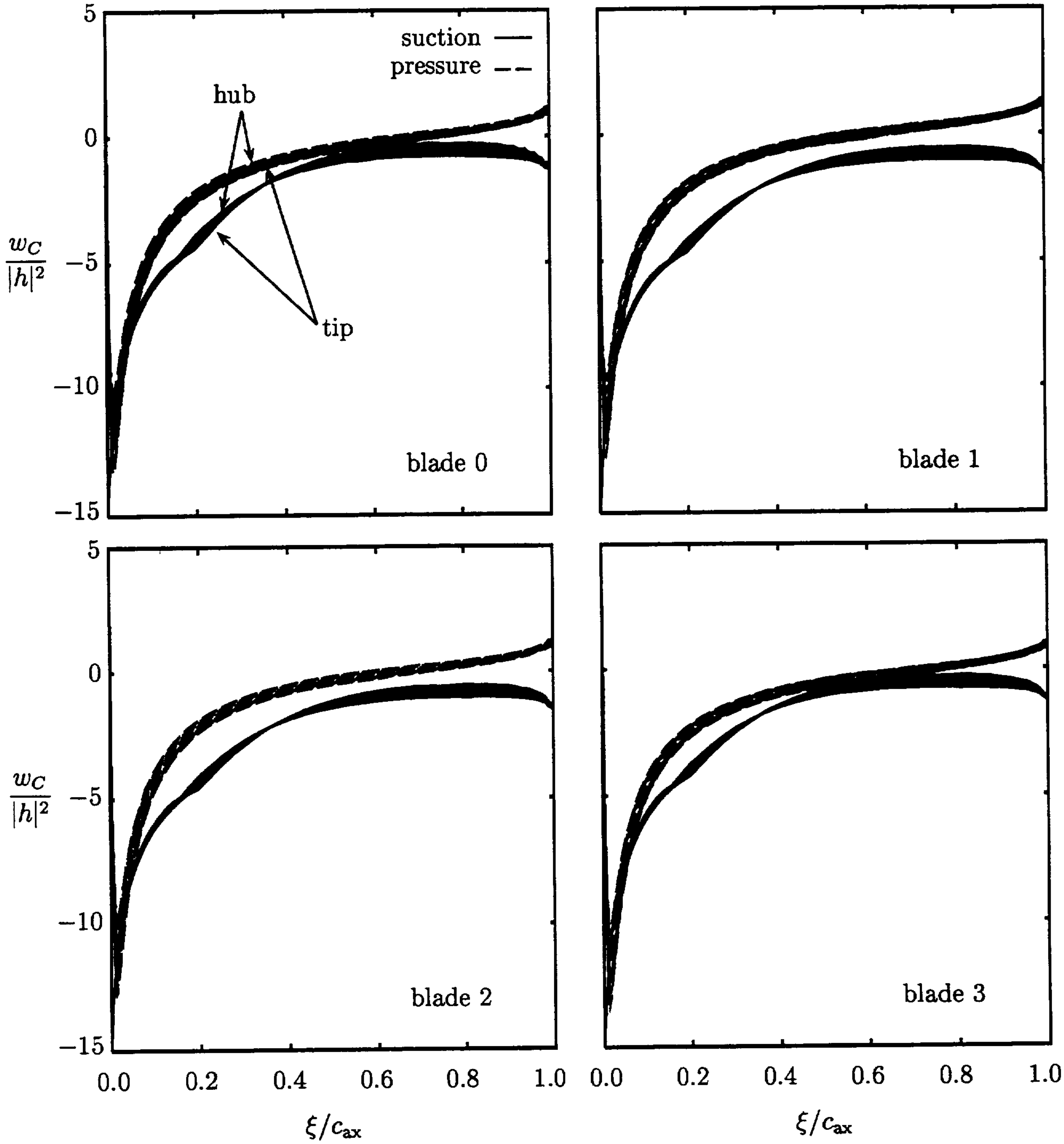

Figure 16: Local work per cycle distributions on four blades of the 3D 10th Standard Cascade undergoing a pure bending vibration at $\omega = 1.0$ and $N_D = -6$.

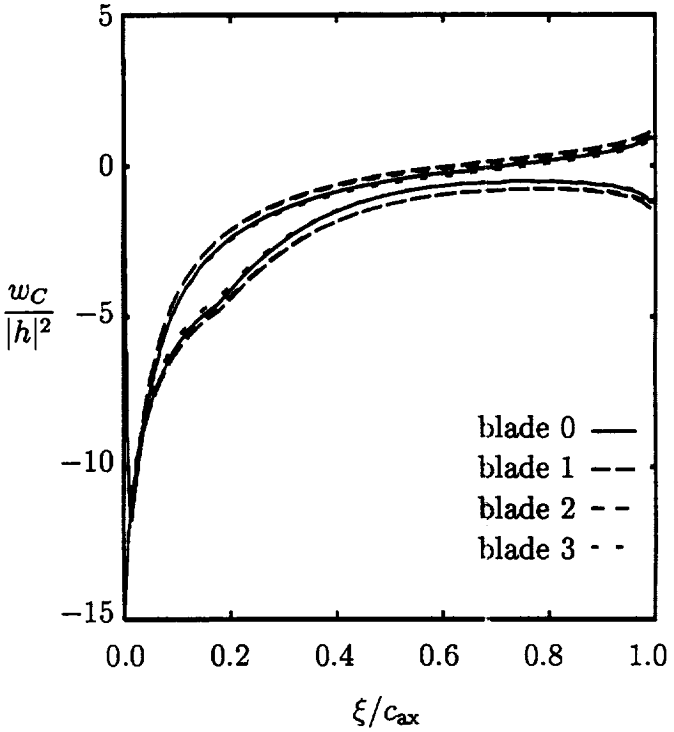

Figure 17: Local work per cycle distributions at midspan for the 3D 10th Standard Cascade undergoing a pure bending vibration at $\omega = 1.0$ and $N_D = -6$.

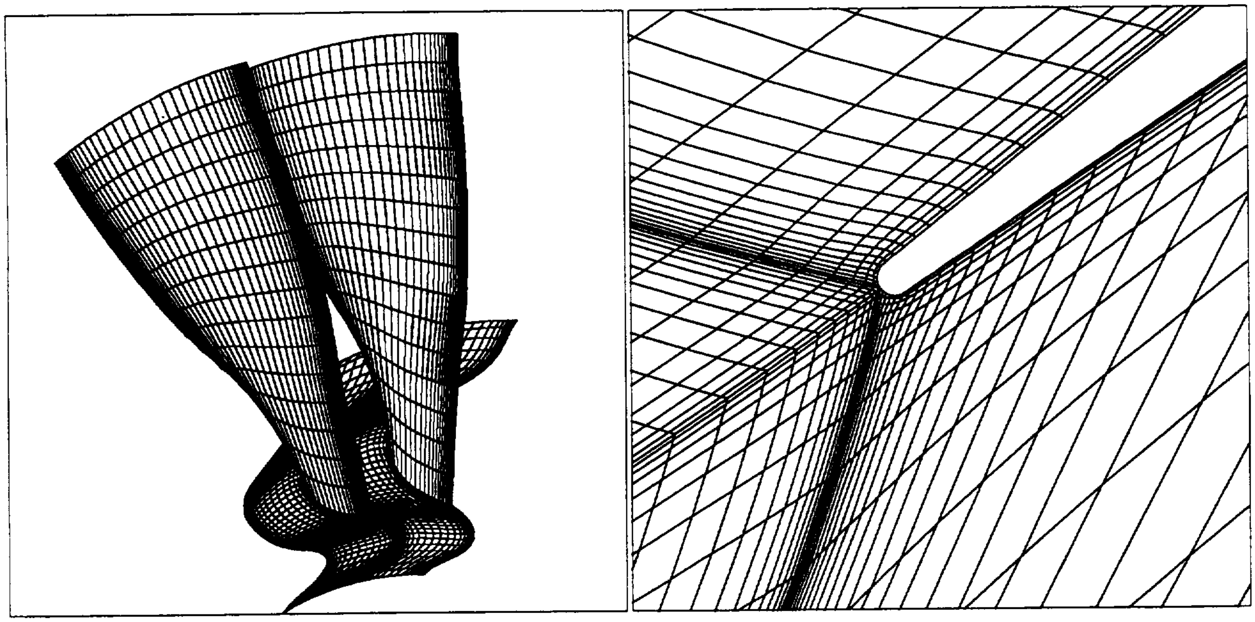

Figure 18: TURBO computational grid for the NASA Rotor 67 and leading edge detail at blade tip.

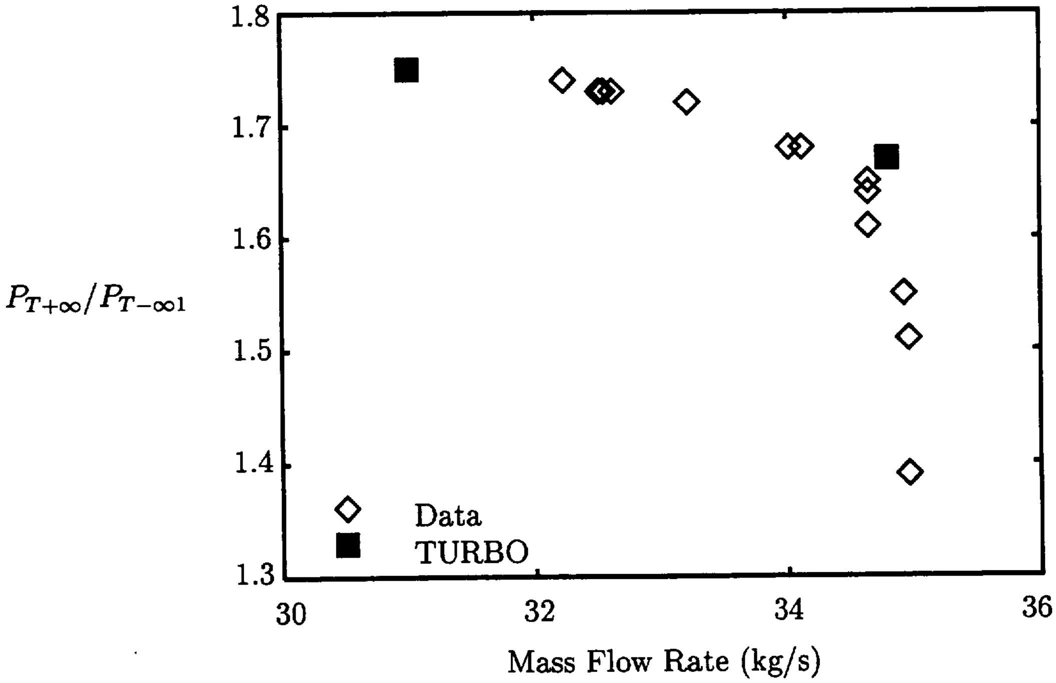

Figure 19: Comparison of measured and computed fan total pressure characteristics for the NASA Rotor 67 fan.

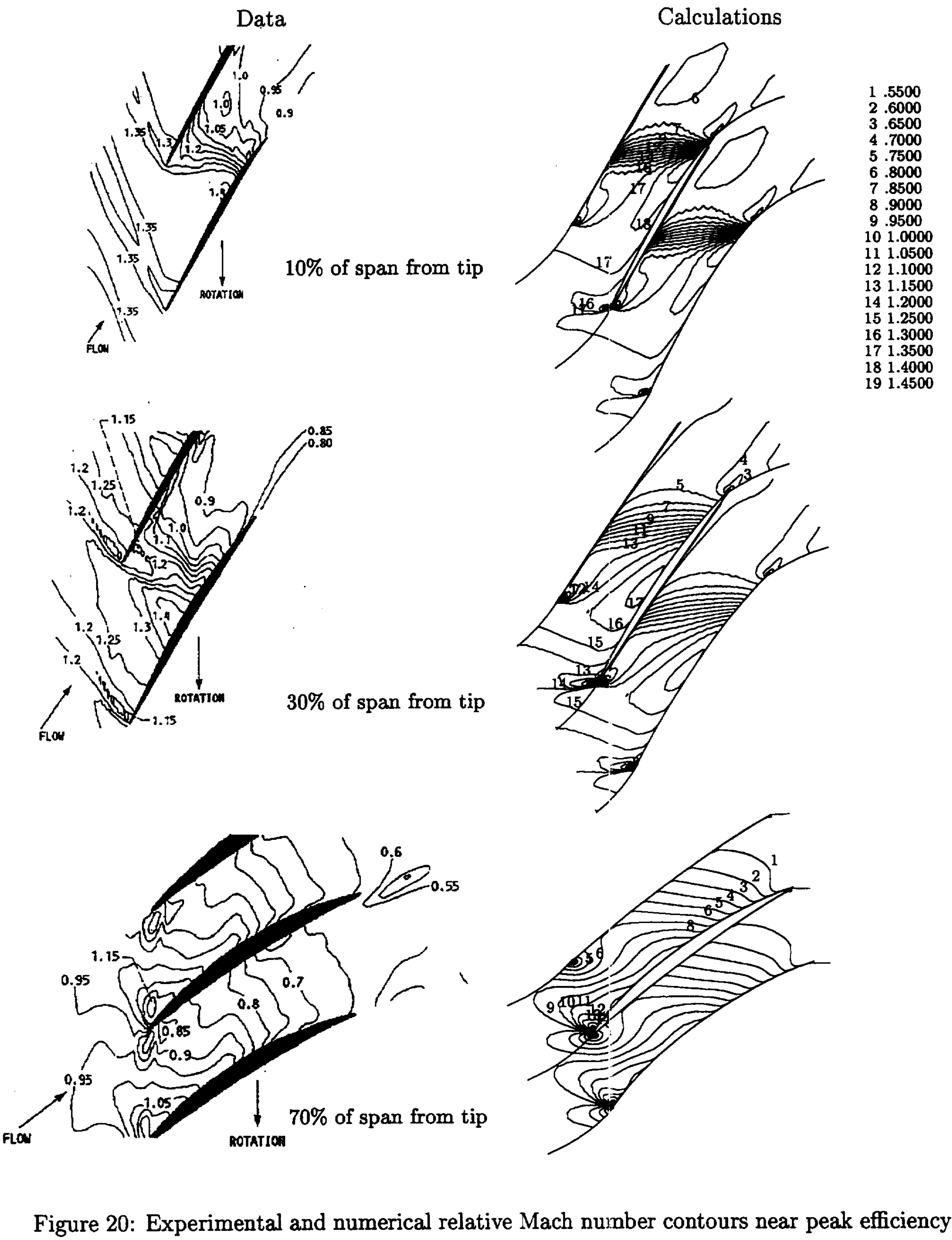
Data

Calculations

10% of span from tip

30% of span from tip

70% of span from tip

Figure 20: Experimental and numerical relative Mach number contours near peak efficiency.

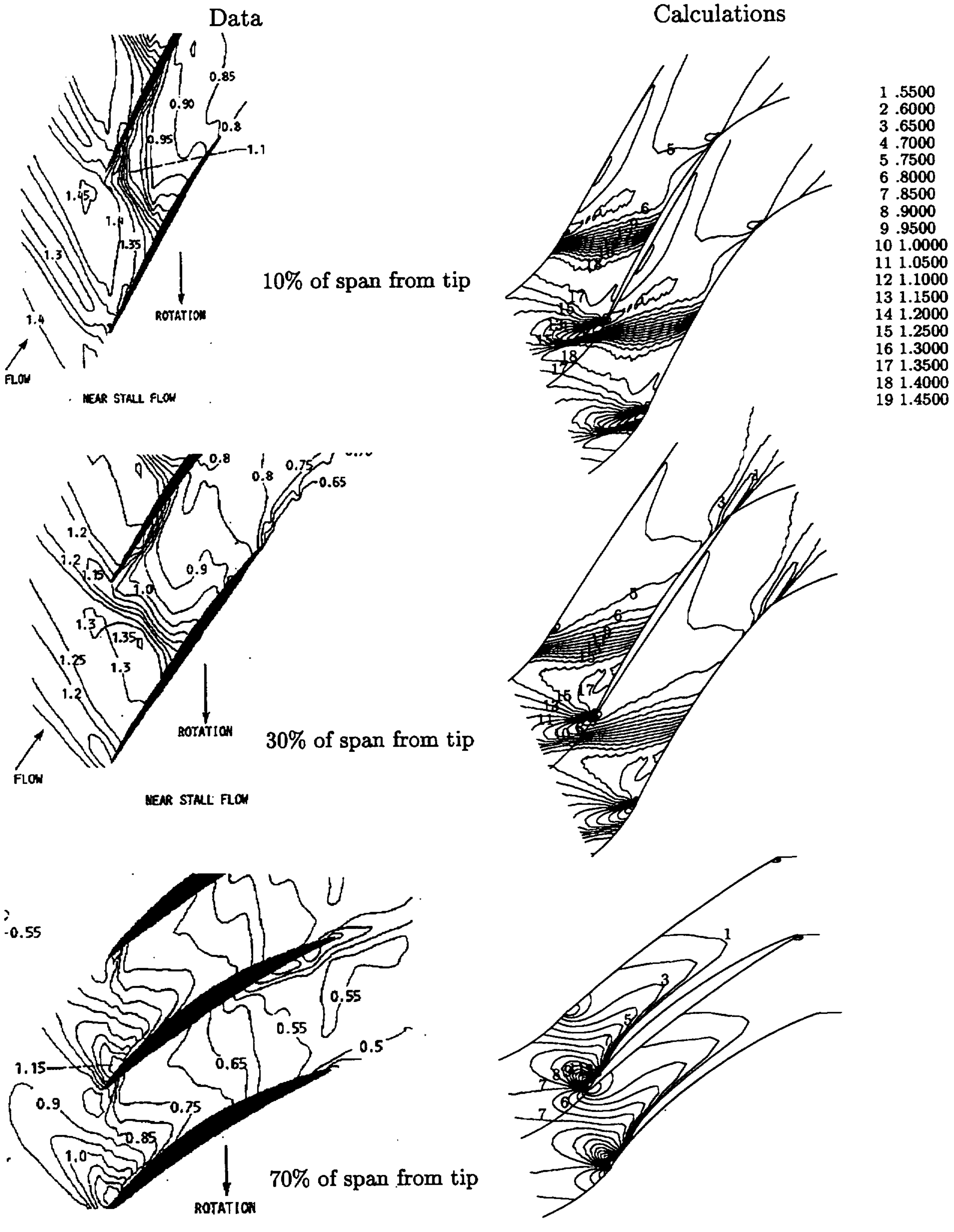

Figure 21: Experimental and numerical relative Mach number contours near stall.

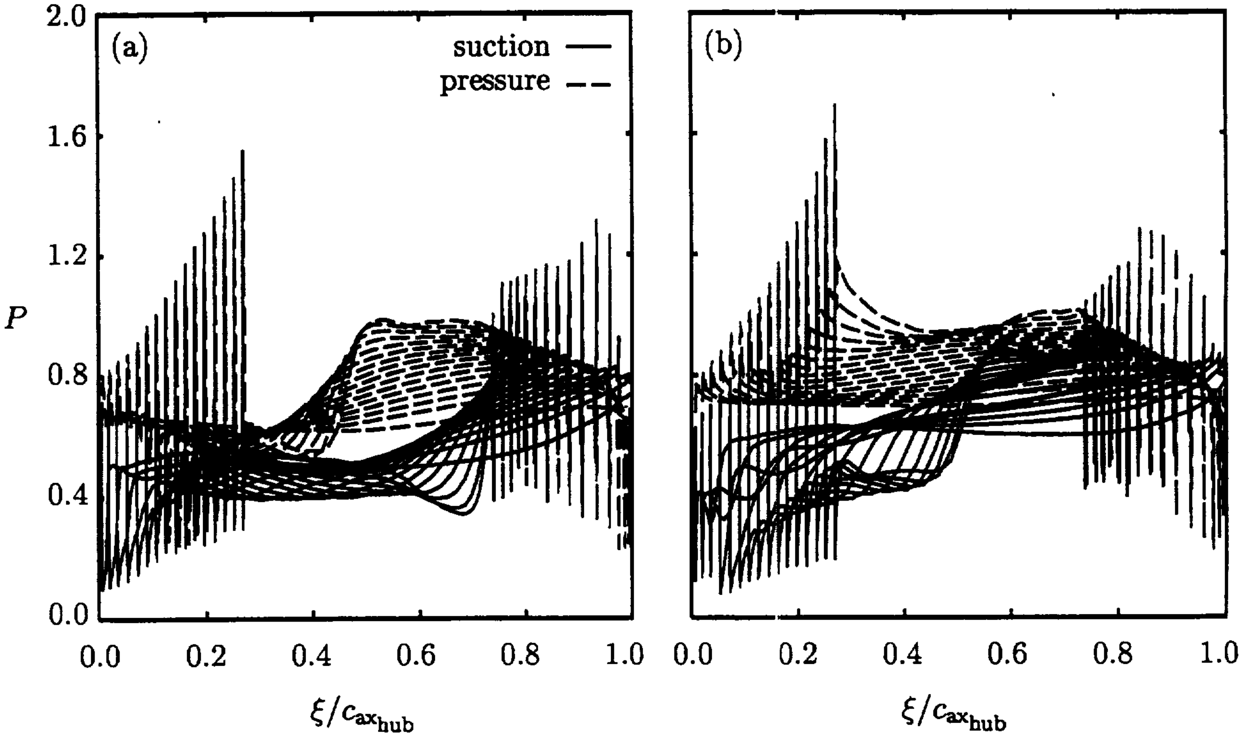

Figure 22: Steady static pressure distributions for the Rotor 67 fan (a) near the peak efficiency point, and (b) near stall.

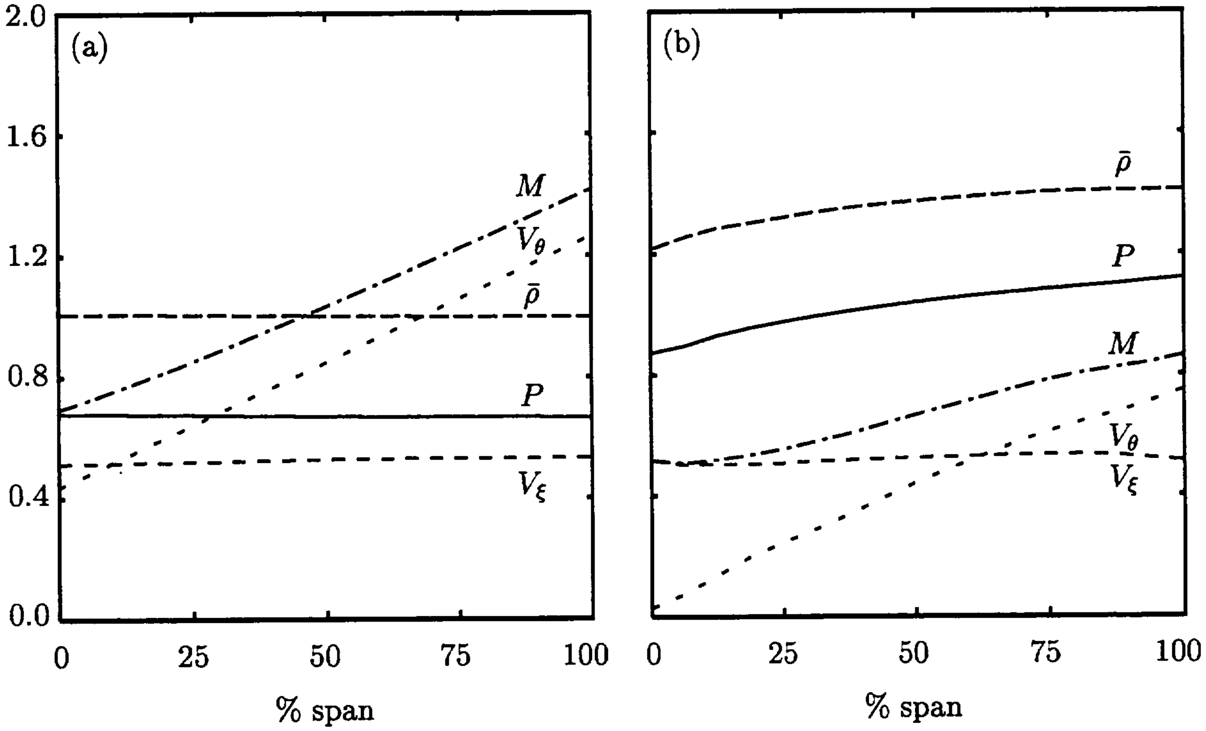

Figure 23: Relative frame steady flow properties (a) far upstream and (b) far downstream of the NASA Rotor 67 fan ($M_{-\infty}^{\mathrm{abs}} \approx 0.526, |\Omega| = 2.524$).

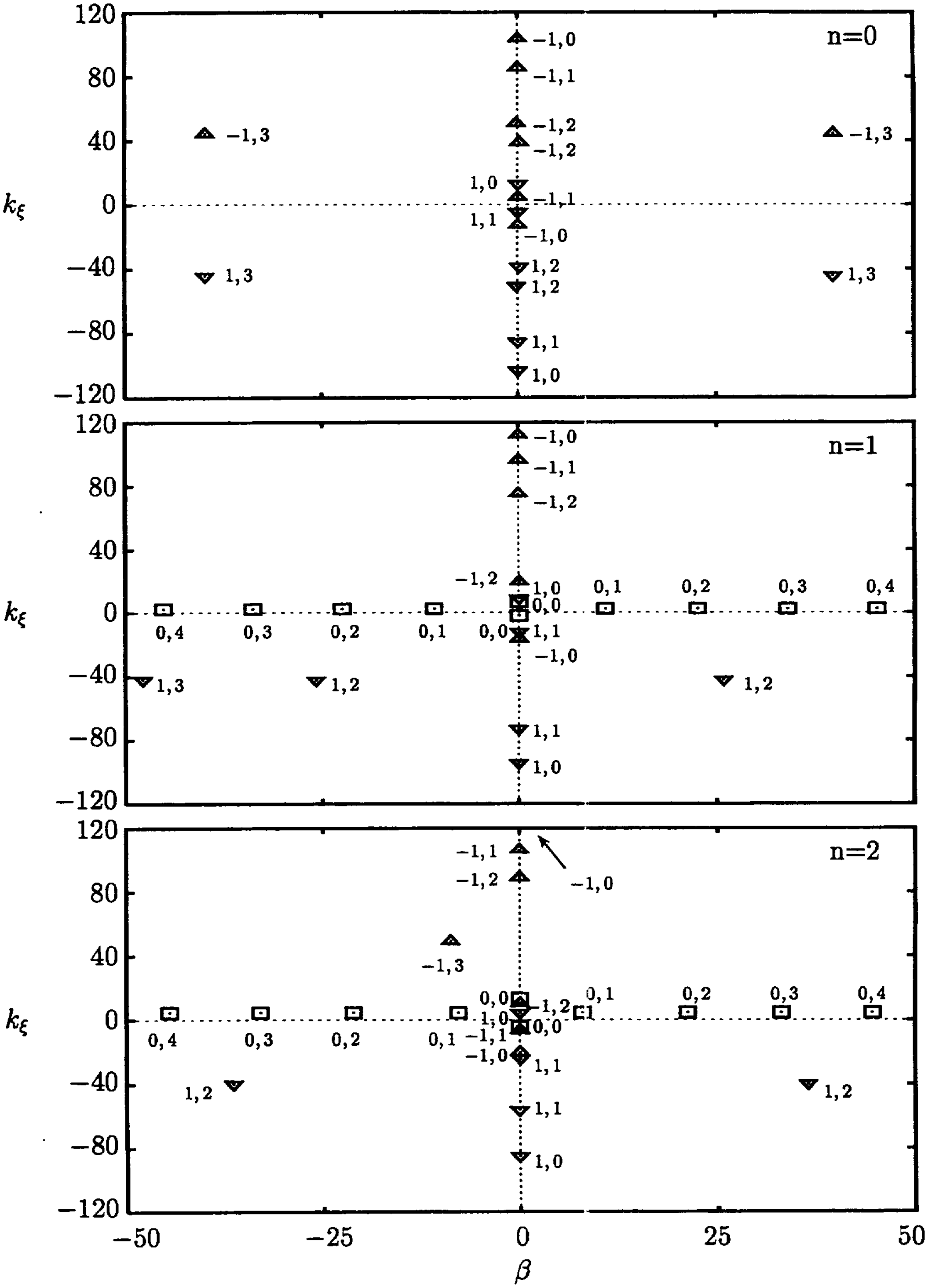

Figure 24: Axial eigenvalues, $\chi = \beta + i\kappa_\xi$, at inlet for the time-mean ($n = 0$), and the first ($n = 1$) and second ($n = 2$) temporal harmonics, and three circumferential ($m = -1, 0, 1$) and five radial ($\mu = 0, 1, 2, 3, 4$) modes of acoustic disturbance in the far field of Rotor 67, for an unsteady flow at $\omega = 0.54$ and $N_D = 0$, and a meanflow condition near peak efficiency.

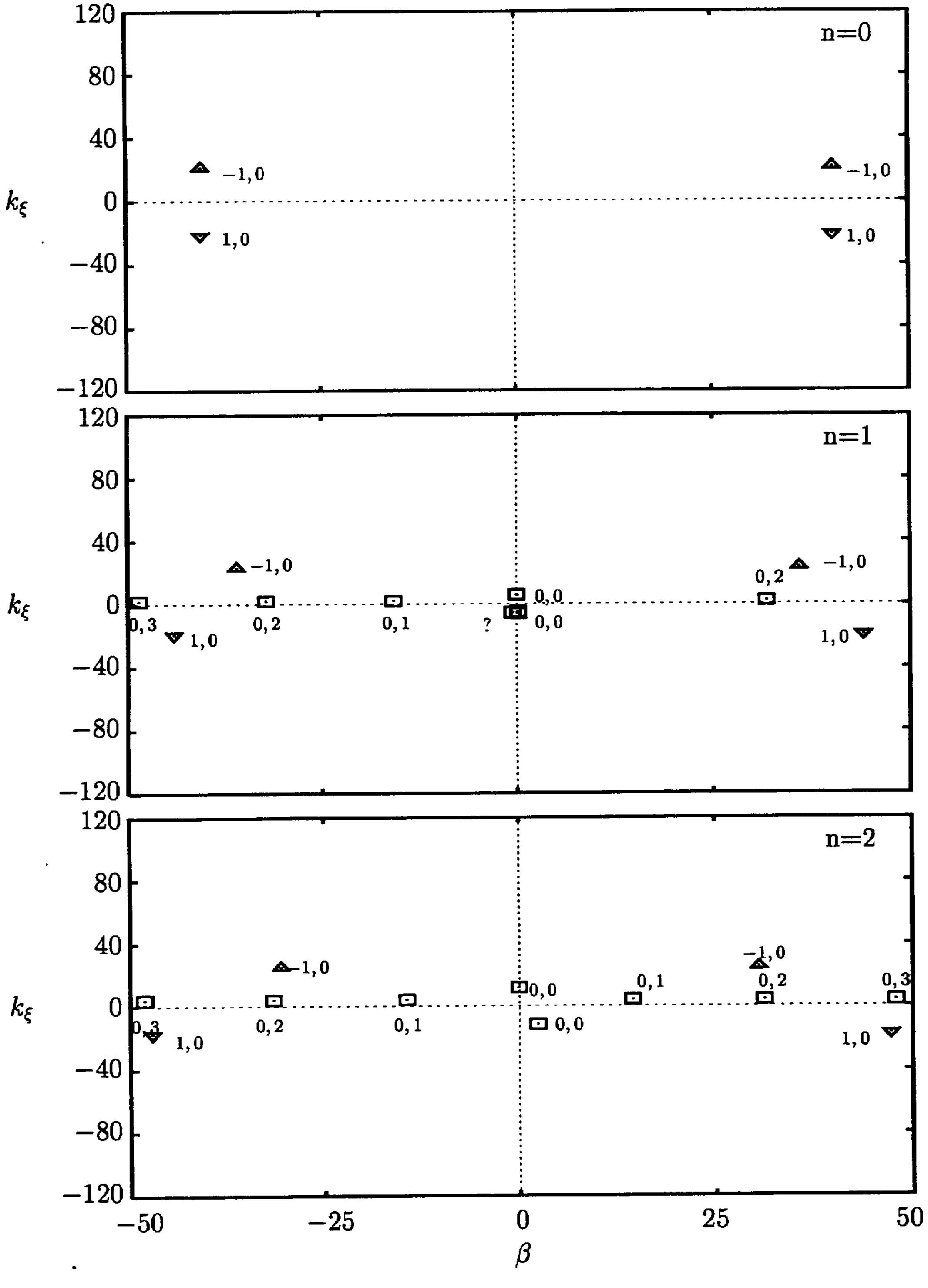

Figure 25: Axial eigenvalues, $\chi = \beta + i\kappa_\xi$, at exit for the time-mean ($n = 0$), and the first ($n = 1$) and second ($n = 2$) temporal harmonics, and three circumferential ($m = -1, 0, 1$) and five radial ($\mu = 0, 1, 2, 3, 4$) modes of acoustic disturbance in the far field of Rotor 67, for an unsteady flow at $\omega = 0.54$ and $N_D = 0$, and a meanflow condition near peak efficiency.

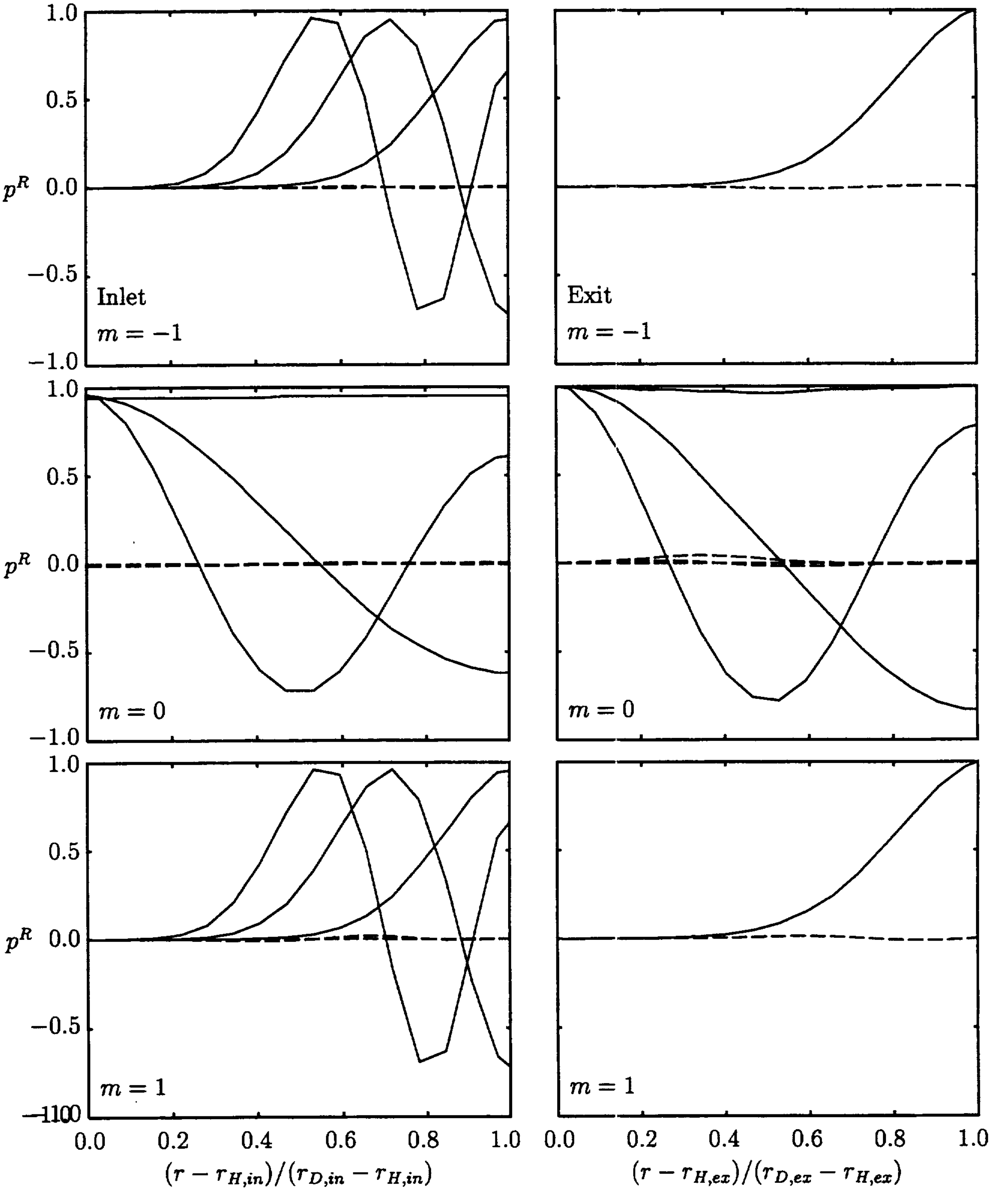

Figure 26: First harmonic, radial pressure modes, $p^R_{m\mu}(r)$, $m = -1, 0, 1$, $\mu = 0, 1, 2$, for an acoustic excitation or response, at $N_D = 0$, far upstream and for an acoustic response, at $N_D = 0$, far downstream of the Rotor 67 fan: (——) in-phase component; (- - -) out-of-phase component of $p^R_{m\mu}(r)$.

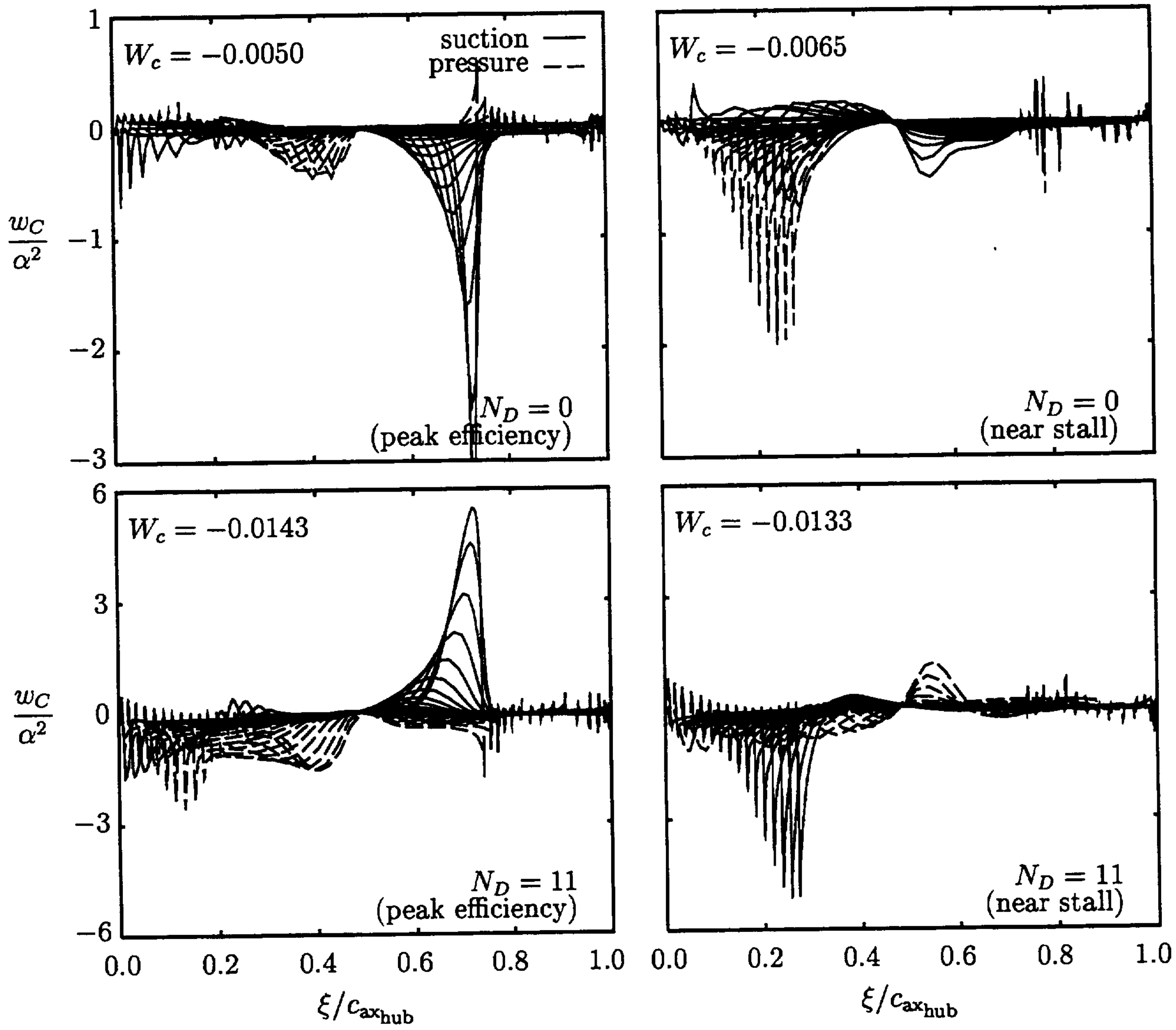

Figure 27: Local work per cycle distributions and global works per cycle for the Rotor 67 fan undergoing pure torsional vibrations about midchord at $\omega = 0.54$ and $\sigma = 0$ and 180 deg ($N_D = 0$ and 11).

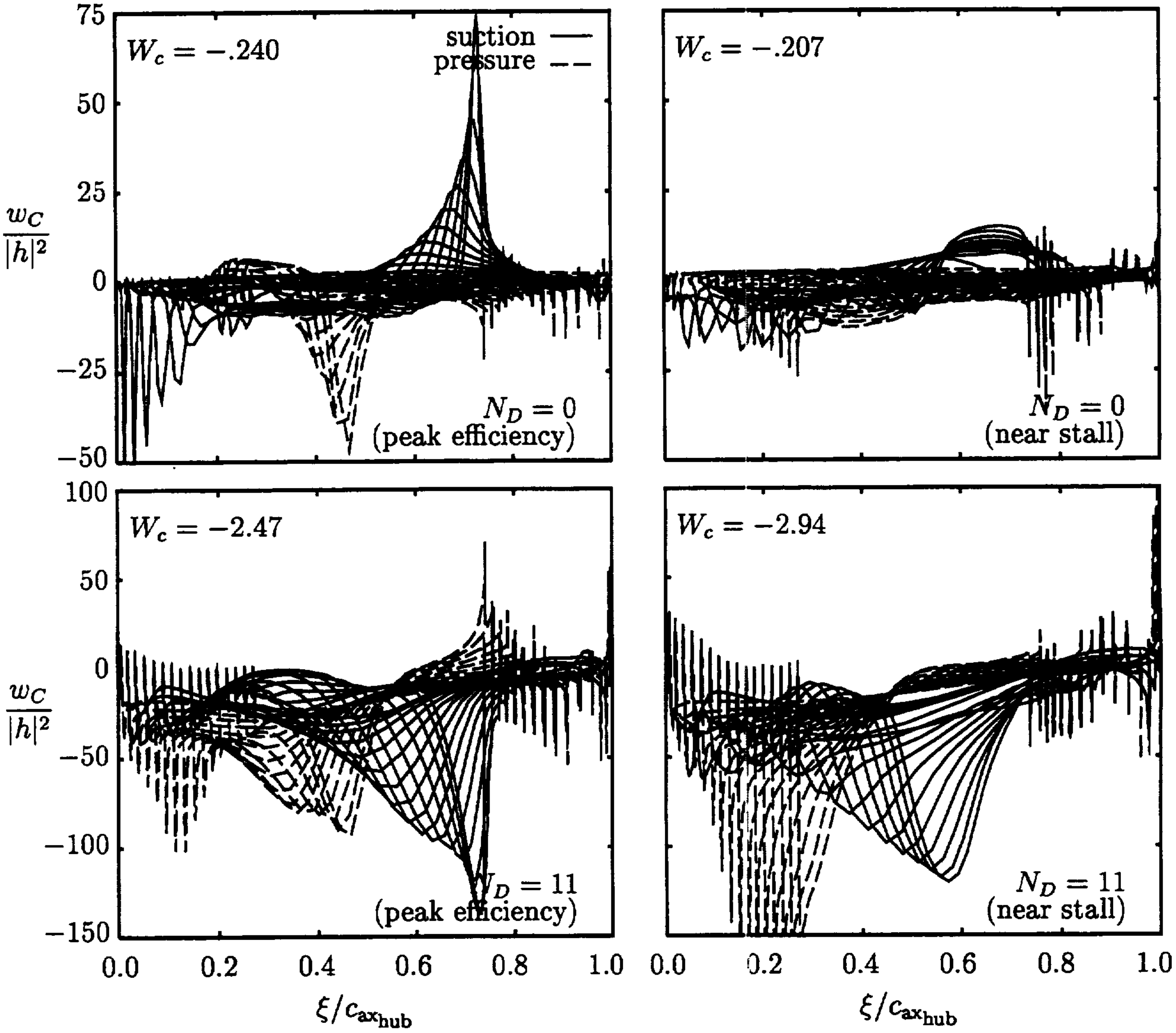

Figure 28: Local work per cycle distributions and global works per cycle for the Rotor 67 fan undergoing pure bending vibrations at $\omega = 0.54$ and $\sigma = 0$ and 180 deg ($N_D = 0$ and 11).

REPORT DOCUMENTATION PAGE

Form Approved
OMB No. 0704-0188

1. AGENCY USE ONLY *(Leave blank)*

2. REPORT DATE
August 1998

3. REPORT TYPE AND DATES COVERED
Final Contractor Report

4. TITLE AND SUBTITLE
A Numerical Simulator for Three-Dimensional Flows Through Vibrating Blade Rows

5. FUNDING NUMBERS
WU-538-03-11-00
NAS3-26618

6. AUTHOR(S)
H. Andrew Chuang and Joseph M. Verdon

7. PERFORMING ORGANIZATION NAME(S) AND ADDRESS(ES)
United Technologies Research Center
Aeromechanical, Chemical, and Fluid Systems
East Hartford, Connecticut 06108

8. PERFORMING ORGANIZATION REPORT NUMBER
E-11283

9. SPONSORING/MONITORING AGENCY NAME(S) AND ADDRESS(ES)
National Aeronautics and Space Administration
Lewis Research Center
Cleveland, Ohio 44135-3191

10. SPONSORING/MONITORING AGENCY REPORT NUMBER
NASA CR—1998-208511
R98-4.101.0238

11. SUPPLEMENTARY NOTES

Project Manager, Dennis L. Huff, Structures and Acoustics Division, NASA Lewis Research Center, organization code 5940, (216) 433-3913.

12a. DISTRIBUTION/AVAILABILITY STATEMENT
Unclassified - Unlimited
Subject Category: 02 Distribution: Nonstandard

This publication is available from the NASA Center for AeroSpace Information, (301) 621-0390.

12b. DISTRIBUTION CODE

13. ABSTRACT ***(Maximum 200 words)***

The three-dimensional, multi-stage, unsteady, turbomachinery analysis, TURBO, has been extended to predict the aeroelastic and aeroacoustic response behaviors of a single blade row operating within a cylindrical annular duct. In particular, a blade vibration capability has been incorporated so that the TURBO analysis can be applied over a solution domain that deforms with a vibratory blade motion. Also, unsteady far-field conditions have been implemented to render the computational boundaries at inlet and exit transparent to outgoing unsteady disturbances. The modified TURBO analysis is applied herein to predict unsteady subsonic and transonic flows. The intent is to partially validate this nonlinear analysis for blade flutter applications, via numerical results for benchmark unsteady flows, and to demonstrate the analysis for a realistic fan rotor. For these purposes, we have considered unsteady subsonic flows through a 3D version of the 10th Standard Cascade, and unsteady transonic flows through the first stage rotor of the NASA Lewis, Rotor 67, two-stage fan.

14. SUBJECT TERMS
Aeroacoustics; Aeroelasticity; Unsteady Aerodynamics; Turbomachinery; Computational fluid dynamics

15. NUMBER OF PAGES
80

16. PRICE CODE
A05

17. SECURITY CLASSIFICATION OF REPORT	**18. SECURITY CLASSIFICATION OF THIS PAGE**	**19. SECURITY CLASSIFICATION OF ABSTRACT**	**20. LIMITATION OF ABSTRACT**
Unclassified	Unclassified	Unclassified	

NSN 7540-01-280-5500

Standard Form 298 (Rev. 2-89)
Prescribed by ANSI Std. Z39-18
298-102